Optical Properties of Semiconducting Two-Dimensional Transition Metal Dichalcogenide and Magnetic Materials Artificial van der Waals Heterostructures

Yan Zhang

Optical Properties of Semiconducting Two-Dimensional Transition Metal Dichalcogenide and Magnetic Materials Artificial van der Waals Heterostructures

Yan Zhang

Graduate School of Energy Science

Kyoto University

Supervisor: Professor Hideaki Ohgaki

04. 2022

Abstract

Optical Properties of Semiconducting Two-Dimensional Transition Metal Dichalcogenide and Magnetic Materials Artificial van der Waals Heterostructures

By

Yan Zhang

Supervisor: Professor Hideaki Ohgaki

Atomically thin two-dimensional (2D) monolayer transition metal dichalcogenides (1L-TMDs) have been extensively studied due to their intriguing optical and electrical properties. Semiconducting 1L-TMDs with a direct band gap exhibits novel excitonic states such as tightly bound electron-hole pair by Coulomb interaction (excitons) because of the strong quantum confinement and reduced dielectric screening effect. Moreover, strong spin-orbit coupling and broken spatial inversion symmetry in 1L-TMDs give rise to doubly degenerate but inequivalent valleys (K+ and K– valley) located at corners of Brillouin zone in the momentum space and an effective coupling of spin and valley. The spin-valley polarized excitons accompanied with direct interband transitions at K+ and K– valley are optically generated by σ^+ and σ^- circularly polarized light, respectively, which also allows to control valley degree of freedom by circularly polarized light. The semiconducting 1L-TMDs with strong-light matter interaction will provide us novel platform to study and control emerging valley-physical properties.

2D materials including semiconducting 1L-TMDs can be freely stacked with other layered materials, which realizes artificial stacking van der Waals (vdW) heterostructures. The artificial vdW heterostructures provide us the opportunities of great number of material combinations with different physical properties, such as semiconducting, insulating, metallic, superconducting, and magnetic materials. The

emerging optical phenomena of interactions between optical excitonic states and magnetic spins including magnetic elementary excitations are expected in the artificial semiconducting and magnetic material vdW heterostructures. These heterostructures push me to study novel light-matter interaction and its modulation by magnetic interactions.

In this thesis, I have studied the optical properties of excitonic states in monolayer $MoSe_2$ (1L-$MoSe_2$), and its magnetic vdW heterostructures. At first, I described the dynamics of valley polarized excitons and trions of 1L-$MoSe_2$ under strong magnetic field to understand the fundamental valley-physics as a model system. Then, I have proposed new semiconducting and ferro-magnetic vdW heterostructures (1L-$MoSe_2$/$(La_{0.8}Nd_{0.2})_{1.2}Sr_{1.8}Mn_2O_7$)) with magnetic phase transition properties to reveal charge transfer and magnetic proximity effect. The photoluminescence (PL) properties of 1L-$MoSe_2$ can be strongly influenced and controlled by the electronic and magnetic properties of Mn oxide underneath, and *h*-BN spacer between semiconducting and Mn oxide. Moreover, I have demonstrated that the valley Zeeman splitting and polarization of 1L-$MoSe_2$ are significantly enhanced in the semiconducting and magnetic vdW heterostructures. I have also investigated the semiconducting and antiferromagnetic vdW heterostructures (1L-$MoSe_2$/$MnPS_3$). The fine spectral peaks in the low temperature PL spectra have been observed, which is attributed to intralayer moiré trion–magnon complexes. It is revealed that the intralayer moiré trion–magnon complexes keep the C_3 symmetry and have longer lifetime and coherence time.

These discoveries and findings on novel optical properties in monolayer semiconductor, and its magnetic vdW heterostructures will provide deeper understanding of valley physics and a perspective for the optical functionalities by magnetic control. These fundamental studies are very important to realize spin- and valley- based applications with low energy cost.

Acknowledgment

It has been an unforgettable and meaningful period in the past three and half years when I studied in Japan. My PhD was full of growth, beginning from a freshman in this research field and ending as a person who can provide help to newcomers. I want to express my gratitude to those who gave me support and help during my PhD studies in this thesis. Without them, I could not be here.

First of all, I would like to thank my supervisor, Prof. Kazunari Matsuda for giving me the chance to work as a PhD student in his group, which is full of talented and dedicated people. I am grateful that he provided me many resources for my research to achieve my goals and gave me valuable advice to me about science and life. His passion and attitudes about research teach me the most essential character of a true scientist, which has an important influence throughout my academic carrier.

I want to thank Prof. Yuhei Miyauchi for his kind guidance and suggestions to my PhD study. Besides, I am grateful to Assistant Prof. Keisuke Shinokita and Assistant Prof. Taishi Nishihara, who shared their knowledges and experimental skills with me.

I appreciate my collaborators. I want to thank Dr. Kenji Watanabe and Dr. Takashi Taniguchi for giving me *h*-BN samples and Prof. Yutaka Moritomo for providing manganese oxide crystals. I want to express my gratitude to Assistant Prof. Masato Goto, Associate Prof. Daisuke Kan, and Prof. Yuichi Shimakawa for their assistance with the SQUID measurement. I want to thank Assistant Prof. Yanlin Gao, Assistant Prof. Mina Maruyama, and Prof. Susumu Okada for DFT calculations. I also want to thank Prof. Hideaki Ohgaki and Prof. Yuhei Miyauchi for acting as members of my thesis committee.

I would like to express my gratitude to all lab members who cannot be absent in my memory of the past three and half years. I want to thank Dr. Fengjiu Yang, Dr. Wenjin Zhang, Dr. Xiaofan Wang, and Dr. Takashi Someya for teaching me a lot in the initial stage of my PhD study. Thank all the other members, Mr. Masafumi Shimasaki, Mr. Kenya Tanaka, Shotaro Mr. Yano, Mr. Kengo Hachiya, Mr. Ken Kiyama, Mr. Kim

Heejun, Mr. Keima Asou, Mr. Mikio Kobayashi, Mr. Wu Hengkai, Mr. Duan Feidong, Mr. Shuichi Asada, Mr. Yuuki Okamura, Mr. Kenichi Nagashima, Mr. Kunpei Anio and Mr. Kaihai Luc for their help, cooperation and accompany.

Last but not least, I want to thank my beloved parents and grandparents for their selfless devotion. I also thank Dr. Wei Yao, for his encouragement and accompany. I would like to deeply appreciate all people above for accompanying me through this difficult but meaningful time.

Yan Zhang

04. 2022

Table of contents

Chapter 1. Introduction

1.1. Background

Advanced materials play a crucial role in the development of modern electronic and optical technologies. Moreover, the size and dimension of materials have significant influences on their chemical and physical properties of materials. Zero-dimension (0D), one-dimension (1D), and two-dimension (2D) exhibit different electronic, optical, magnetic, and chemical characteristics. In 0D nanostructures such as semiconductor quantum dots and fullerenes, their properties are affected by the quantum confinement effect in three directions. The carbon nanotube is an example of 1D materials with confinement by only one direction. The quantum wells are among 2D materials with confinement in the plane[1].

Graphene as the first 'modern' 2D material was mechanically isolated from graphite in 2004[2], by which K.S. Novoselov and A.K. Geimwho were awarded the Nobel Prize in 2010. Since the rapid development of graphene-related research[3], hundreds of other layered materials have been reported[4]. Among these materials, atomic thin films of transition metal dichalcogenides, which can be prepared by exfoliating from their bulk crystals like graphene become one of the most attractive research fields in physics, chemistry, and material science[5–8].

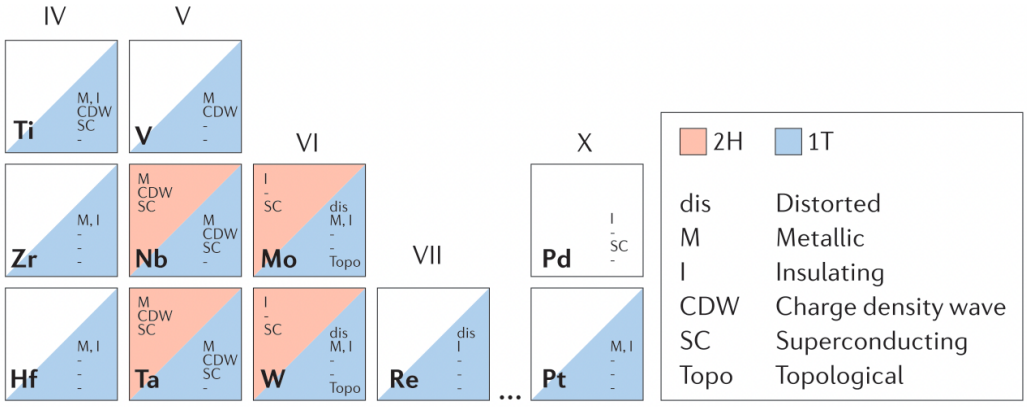

Figure 1.1. Periodic elemental table of the transition metals and the chalcogen atoms that predominantly crystallize in those layered structure. Reprinted with the permission from Ref.[3]. © 2017 Springer Nature.

It has been about one hundred year since the first revealing of the hexagonal crystal structures of TMDs materials[9]. About 60 kinds of TMDs had been studied until the late of 1960s. Over half of them were layered structure, which could be cleaved down to 10 to 100 nm[10,11]. Several special topics have been explored since that time, such as screening effect, *d* band formation, metal to insulator transition, superconductivity as well as magnetism[10].

In the past few years, TMDs reemerged and attracted considerable attention because of their very interesting electronic and optical properties. As shown in **Figure 1.1,** the general formula of TMDs is MX_2, where M represents a transition metal element and X is a chalcogen element. The bulk TMDs range from insulators such as HfS_2, semiconductors including $MoSe_2$ and WSe_2, semimetals such as WTe_2, to metals such as NbS_2[12], which are also indicated in **Figure 1.1**.

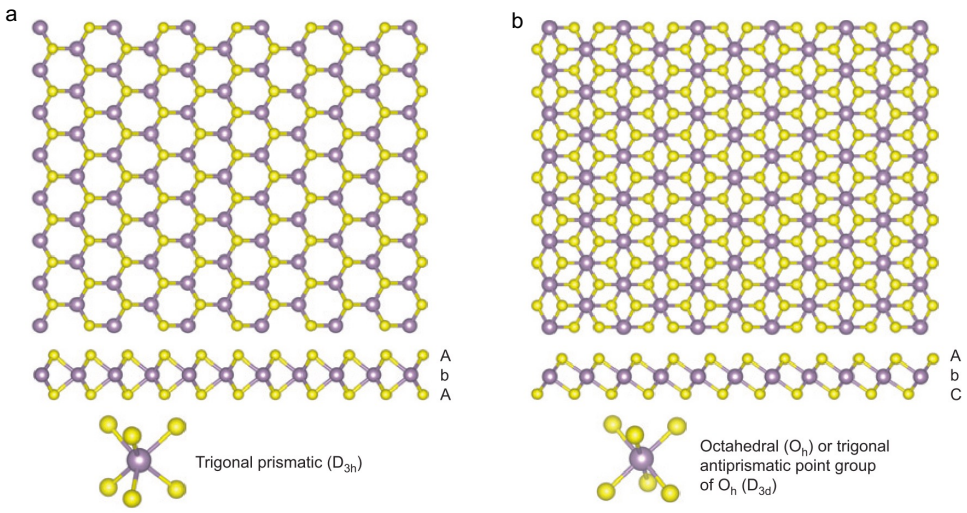

Figure 1.2. Top view of 1L-TMD with 2H (a) and 1T (b) coordination. Metals are in purple, and chalcogenides are in yellow. Reprinted with the permission from Ref.[12]. © 2013 Springer Nature.

TMDs have several structures caused by different stacking orders of the three atomic planes forming the individual layers of these materials. **Figure 1.2** shows two structural phases that are trigonal prismatic (2H) and octahedral (1T) coordination. **Figure 1.2a** shows that the 2H phase formed by ABA stacking of X and M elements in different atomic planes, which breaks the spatial inversion symmetry[3]. In contrast, the

1T phase is formed by ABC stacking (**Figure 1.2b**). The 2H phase of group-VI TMDs (M=Mo, W; X=S, Se) is thermodynamically stable[13,14], which is the focus of thesis.

Group-VI TMDs transit from indirect to direct band gap semiconductors with their thickness from bulk to monolayer. Compared with gapless graphene, the monolayer TMDs (1L-TMDs) with a direct band gap show novel excitonic properties, because of strong quantum confinement effect and reduced dielectric screening[6,15]. Optically generated quasiparticles (excitons and trions) in 1L-TMDs are very sensitive to surroundings, whose properties could be modulated by substrate underneath[16,17]. Moreover, 1L-TMDs have double-degenerate but inequivalent valleys (K+ and K–) at corners of Brillouin zone as the strong spin-orbit coupling together with broken inversion symmetry[13,18–20]. Valley gives rise to new degree of freedom. The excitons in 1L-TMDs, are also endowed with a valley degree of freedom because of the localization of the constituent electrons and holes in the K+ and K– valleys[20]. The broken inversion symmetry of 1L-TMD also contributes to a valley optical selection rule, where right and left circularly polarized light couples to interband transitions in the K+ valley and the K– valley, respectively. Circularly polarized light is experimentally used to inject excitons to preferential valley, leading to a different population of the two valley excitons (valley polarization of excitons). Two valleys can be considered as a binary pseudospin that are possibly used to process and store information. The manipulation of valley pseudospins is desired to realize valleytronic applications which are more attractive than spin-logic devices. The modern spin-logic technologies require large current and high magnetic field, giving rise to the slow speed and high-power consumption. However, valleytronic applications are possible to eliminate these disadvantages of spin-logic technologies.

Furthermore, vertically stacking different 2D materials such as 1L-TMDs, called van der Waals (vdW) heterostructures, provides a new platform to study novel and emerging interface phenomena in in artificially stacked structures[21]. A wide range of 2D materials, ranging from semiconducting 1L-TMDs[22,23], insulating hexagonal boron nitride (*h*-BN)[24], magnetic EuS[25,26], to metallic graphene[26] can be used to fabricate

vdW heterostructures. Noteworthy physical phenomena, such as magnetic proximity effect[27,28] and moiré related physics[29–31], have been investigated in vdW heterostructures based on 1L-TMDs. Thus, the unique excitonic physics with valley contrast in 1L-TMDs and its capability to construct vdW with other layered materials make them interesting for fundamental studies and for device applications such as electronics, spintronics, valleytronics, and energy storage[3], which are expected to inspire environment friendly applications with low energy cost.

1.2. Motivation

The semiconducting 1L-TMDs have novel and unique optical properties as described above. These atomically thin materials provide opportunities to engineer the optical properties arising from excitonic states (excitons) on the nanometer scale in 2D materials for emerging and complex functionalities[6]. Moreover, 1L-TMDs can be strongly affected by magnetic materials underneath, which provides a good platform to study the interactions of excitons and magnetic spins. For instance, the valley degeneracy of excitonic states of 1L-TMDs can be significantly lifted by introducing ferromagnetic insulator substrate[25,26]. 1L-TMD and magnetic vdW heterostructures will provide the opportunities towards new routes to study the exotic interface interactions and high-performance applications with novel functionalities of magnetic control and switching. Therefore, I aim to create new systems consisting of semiconducting TMDs and magnetic layered materials to realize emerging physical phenomena for fundamental study in physics, material science, and future applications.

1.3. Chapter outline

In this thesis, I mainly focus on studying the optical properties of semiconducting monolayer $MoSe_2$ (1L-$MoSe_2$) and its magnetic artificial vdW heterostructures by optical spectroscopic approaches. The thesis is organized by following:

In **Chapter 2**, brief introduction of basic knowledge of optical properties in 2D materials, especially the physics of excitons and valley degree of freedom in 1L-TMDs

will be introduced. In **Chapter 3**, I will describe the experimental methods and equipment of this thesis.

Chapter 4, 5, 6 will give a detailed clarification of my research results. To be specific, I will systematically demonstrate the dynamics of excitonic valley polarization in 1L-$MoSe_2$ using polarization- and time-resolved PL spectroscopy under magnetic field in **Chapter 4**. As large valley polarization is desired for future valley-tronics applications, the strategy for robust enhancement of valley polarization has been demonstrated in 1L-$MoSe_2$ realized by introducing a ferromagnetic metal Mn oxide with insulating spacer due to the magnetic proximity effect, in **Chapter 5**. In **Chapter 6**, I will describe novel excitonic states interacting with a magnetic elementary excitation in antiferromagnetic vdW heterostructures.

Finally, the summary and outlook for the future will be described in **Chapter 7**.

Chapter 2. Optical properties of low dimensional semiconductors

Low dimensional layered materials like graphene and TMDs provide unique advantages, compared with bulk materials. The reduction in thickness to atomical scale will significantly be changed the material physical properties from those in bulk form, resulting in binding energy of excitons, valley degree of freedom, valley Zeeman effect, and so on. Moreover, van der Waals heterostructures by stacking different layered materials offer novel platform to study and engineer emerging quantum states.

2.1. Basic optical properties of 2D materials

2.1.1. Electronic band structure

The optical properties of materials are mainly affected by their electronic band structures and dielectric screening effect[32–34]. The dielectric screening effect will be discussed in the next section. Here I will briefly introduce the electronic structure of graphene, because the electronic effective model for large amount of 2D materials can find their prototype in graphene[34]. Graphene is formed by a single atomic layer of carbon atoms with hexagonal honeycomb lattice structure. The tight binding model is frequently used for deriving the electronic structure of graphene[35]. **Figure 2.1** shows the electronic dispersion of graphene, calculated by tight binding approach, resulting in Dirac points at the corner of Brillouin zones[36]. The expanded electronic structure around to the Dirac cones are shown in right side of **Figure 2.1**. The electronic dispersion can be simply described near Dirac point by a linear relationship as follow[34].

$$E = \pm p v_{\mathrm{F}}, \tag{2.1}$$

where E is the electron energy, p is the relative momentum with respect to Dirac points, v_{F} is called Femi velocity with the value of around 10^6 m/s, plus (+) and minus (−) are the conduction and valence band, respectively.

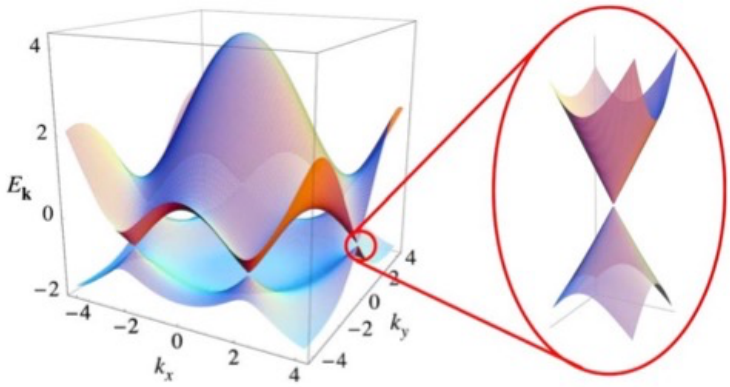

Figure 2.1. Electronic dispersion of graphene with honeycomb symmetry in the momentum space. On the left hand, it shows the energy dispersion as function of k_x and k_y. The image at right hand is the zoom of the energy band near a Dirac point (Reprinted with the permission from Ref.[36]. © 2009 APS).

Moreover, the band gap of graphene is zero, which leads to semi-metallic properties. Such an exotic linear dispersion is strikingly different from semi-metallic bilayer graphene and graphite with parabolic dispersion at the Fermi energy[35]. The graphene band structure is sensitive to the lattice symmetry as shown in **Figure 2.2**. The free-standing symmetric double layer graphene in Bernal stacking is gapless. However, a tunable band gap up to 250 meV will be opened in bilayer graphene if the inversion symmetry is broken by external electric field (**Figure 2.2c**)[37,38].

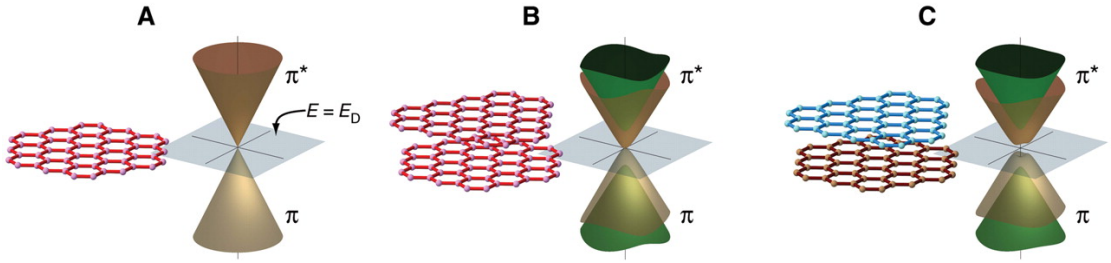

Figure 2.2. Electronic structure of monolayer graphene (a), symmetrical bilayer graphene (b), and asymmetrical bilayer graphene (Taken from Ref.[39]).

As discussed above, the strong dependence on layer number for graphene electronic structures has made thickness tuning as an essential research way in graphene studies. Such a research philosophy can also be applied to semiconducting TMDs (thermodynamically stable 2H phase), e.g., $MoSe_2$, MoS_2, WSe_2, and WS_2, which

attract much attention, since a transit from indirect to direct band gap is revealed when their thicknesses are thinned down from bulk to monolayer. **Figure 2.3a, b** display the calculation results from bulk and monolayer MoS_2 using density functional theory (DFT) with generalized gradient approximation[40,41], respectively.

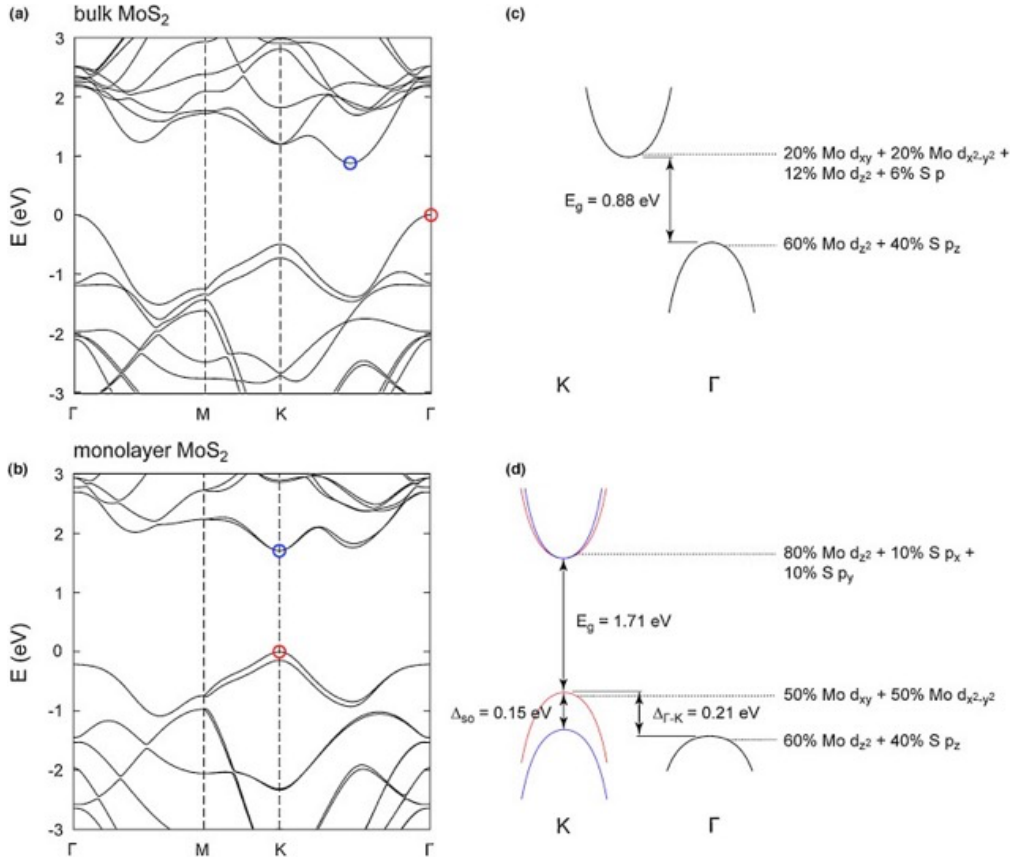

Figure 2.3. Electronic band structure of bulk MoS_2 (a), and monolayer MoS_2 (b). Schematic pictures of low energy band of bulk MoS_2 (a), and monolayer MoS_2 with characters of electronic orbitals and spin-orbit splitting (Taken from Ref.[40]).

Taking MoS_2 for example, the gap type transition is shown to be the results of orbital composition of electronic states and quantum confinement effect[40]. For its bulk crystal, the states near valence band maximum (VBM) at Γ point are mainly composed of *p* orbitals of S atoms and *d* orbitals of Mo atoms. The orbital geometry along out-of-plane direction makes the energy levels of these states significantly affected by quantum confinement effect as shown in **Figure 2.3c**. Hence, with decreased thickness of MoS_2, indirect band gap size grows due to the enhanced quantum confinement effect[42]. On the other hand, the states at valence (VB) and conduction band (CB) at K point are

mainly made up of localized *d* orbitals from Mo atoms (**Figure 2.3d**) which are laid in plane and are less sensitive to interlayer coupling than those near Γ point. Therefore, the direct band gap almost remains unchanged. The different characteristic of band gap in bulk and monolayer group-VI TMDs gives rise to the distinguishing optical properties, which will be demonstrated in the following sections.

2.1.2. Dielectric screening

Dielectric screening of 2D materials is strikingly different from that of bulk material, which can be understood by a simple picture using the knowledge of solid-state physics. In bulk materials, the charge is partly screened by the polarization charge. However, in the case of 2D materials, the previous simple description cannot work anymore, because the field line of testing charge extends outside the atomic thin materials into the vacuum, where the screening effect is significantly suppressed[43]. Due to the reduced screening effect, the optically excited electron-hole pairs (excitons) have a large binding energy in 2D materials, which is very important in studying the optical excitation of monolayer TMDs.

Moreover, in practice, the existence of special surroundings like substrates underneath will further modify the optical behaviors of 2D materials are very sensitive to surroundings like substrates underneath. For example, considering the effect from substrates, the screening is finally taken into account by a dielectric constant with the value of $(\varepsilon_{sub} + 1)/2$, when 2D material is supported by a substrate with dielectric constant of ε_{sub}[40]. To be more accurate, the dynamical dependence of dielectric function on the wavevector (q) and frequency (ω) should be considered[44,45].

2.1.3. Excitons

When a semiconductor absorbs a photon with higher energy than its band gap, a quasi-particle, called exciton, is then formed as a complex state of an electron at CB and a hole at VB bound by the Coulomb interaction. The excitons have been experimentally observed in many solid-state materials, which can be classified into two

types — Frenkel exciton (**Figure 2.4a**) and Wannier-Mott exciton (**Figure 2.4b**), depending on the size of excitons and the strength of Coulomb interaction.

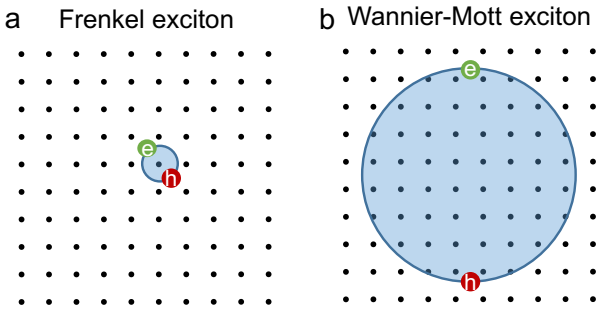

Figure 2.4. Schematic of Wannier-Mott exciton (a), and Frenkel exciton (b).

The Frenkel excitons with a binding energy on the order of 0.1-1 eV[46], usually have a smaller radius and exist in atoms, molecules or insulators. In contrast, the Wannier-Mott excitons which are also called as free excitons, are mainly observed in semiconductors. Because of the reduced Coulomb interaction between electron and hole, they have a large radius and can freely move through the crystals. In addition, charged excitons (trions) can be formed as well in the semiconductors. The trion is a bound state composed of two electrons and a hole (negatively charged exciton or negative trion) or an electron and two holes (positively charged exciton or positive trion), as shown in **Figure 2.5**. In some cases, four-particle complexes as biexciton can also exist, under higher exciton density (**Figure 2.5c**). In this thesis, I will focus on discussing the Wannier-Mott excitons or trions in TMDs.

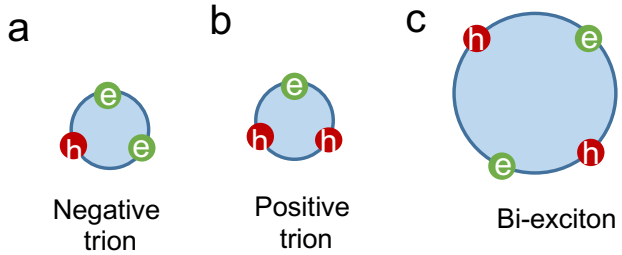

Figure 2.5. Schematic illustration of negative trion (a), positive trion (b), and biexciton (c).

The Bohr model can be applied to exciton because we can think that the electron in exciton is bound and move around the hole, like a hydrogen atom. The exciton energy

levels which depend on dimensionality (α) of semiconductor, can be given as below[47]:

$$E_n = E_g - \frac{E_e}{\left(n+\frac{\alpha-3}{2}\right)^2}, \tag{2.2}$$

$$E_e = \frac{m_e \varepsilon}{\mu} E_H, \tag{2.3}$$

where n=1, 2, 3…, is the principal quantum number, E_g is the bandgap, E_e is the effective Rydberg constant, E_H is the Rydberg constant, m_e is the free-electron mass, ε is the dielectric constant, and μ is the reduced mass of electron in exciton.

According to the **Eq. (2.2)**, the binding energy of 1s exciton (E_b) is described as below[47]:

$$E_b = \left(\frac{2}{\alpha-1}\right)^2 E_e, \tag{2.4}$$

therefore, in the case of three-dimensional ($\alpha = 3$) system, $E_b = E_e$, while in the two-dimensional case, $E_b = 4E_e$, which is 4 times larger than that of 3D materials because of the reduced dielectric effect.

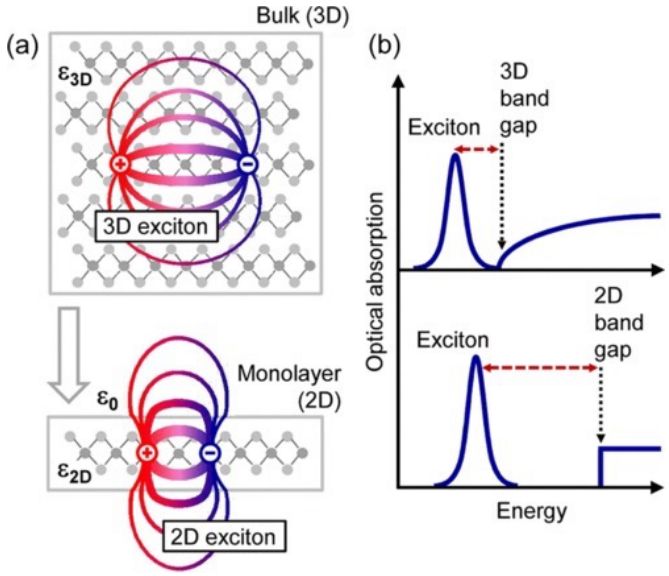

Figure 2.6. (a) Real space illustration of excitons with electric field lines in 3D (upper) and 2D semiconductors (down). (b) Optical absorption of 3D and 2D semiconductors, which is affected by the electronic and excitonic properties caused by the dimensionality (Reprinted with the permission from Ref.[48]. © 2009 APS).

In an atomically thin 2D semiconductor, the electric field lines of exciton extend

outside the monolayer material[48] as shown in **Figure 2.6a**, which leads to the dramatically reduced screening effect as discussed in **Section 2.1.2**. This contributes to a further enhancement factor (more than 4) of binding energy in exciton in atomic thin semiconductors, which is called as "dielectric confinement" or "image charge effect"[48]. In addition to larger binding energy of excitons in 2D materials than that in 3D materials, the quasiparticle band gap is also enhanced in monolayer materials. This behavior can be observed in optical absorption spectra, as shown in **Figure 2.6b**. As discussed above, the excitonic properties in 2D materials can be strikingly different from their bulk crystals.

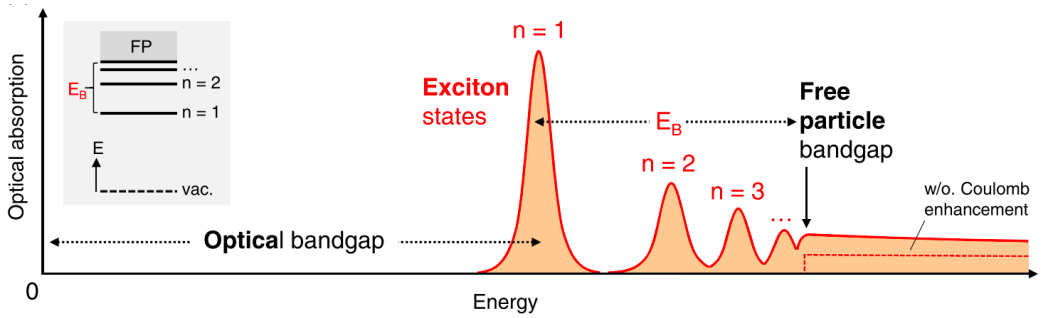

Figure 2.7. Schematic of relationship between excitonic Rydberg states and electronic band gap. The inset shows the energy level schematic diagram of exciton states. (Reprinted with the permission from Ref.[6]. © 2018 APS).

Figure 2.7 shows the relationship between excitonic Rydberg states and free particle electronic band gap. The emergence of bound exciton states below the free particle bandgap caused by the Coulomb attraction between electrons and holes, which are labelled by their corresponding principal quantum number[6,49]. The inset shows the energy level schematic diagram of atomic like exciton states with the binding energy (E_B) of ground state (n=1) below the free particle (FP) bandgap[6,49].

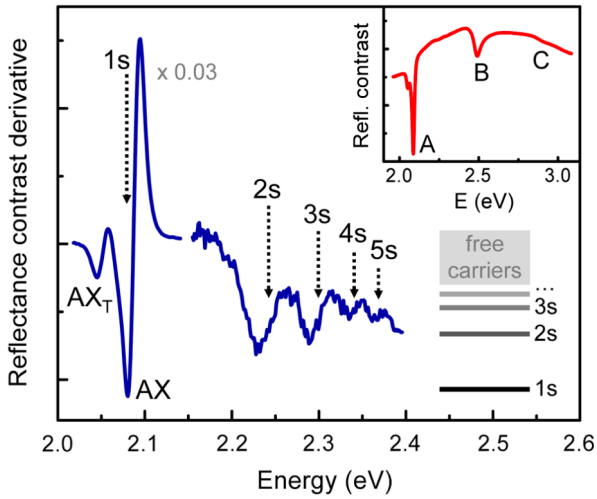

Figure 2.8. Experimental result of reflectance contrast of 1L-WS_2 at 5 K with inset of the main transitions of *A*, *B*, and *C* excitons (Reprinted with the permission from Ref.[50]. © 2014 APS).

Experimentally, the reflectance contrast defined as $\frac{\Delta R}{R} = (R_{\text{sample}} - R_{\text{substrate}})/R_{\text{substrate}}$ can demonstrate the characteristic features of excitonic Rydberg series in 1L-TMDs and the binding energy can be estimated, where R_{sample}, and $R_{\text{substrate}}$ are reflectivity from sample and substrate. **Figure 2.8** exhibits the experimental result of reflectance contrast derivative of 1L-WS_2 at 5 K. The inset shows the main transitions of *A*, *B*, and *C* excitons[51]. The main figure explains the properties of *A* excitons with the estimated binding energy on the order of 20–30 meV[50]. The peak intensity and the energy spacing of 1s, 2s, 3s, 4s, and 5s states of the *A* exciton reduce with energy increasing are typical properties of an excitonic Rydberg series.

2.1.4. Photoluminescence

Photoluminescence is a radiative emission process, which happens when excited states relax to the lower energy level by emitting photons. **Figure 2.9** shows the general diagram of PL process in solids. Here, τ_{NR} is the non-radiative decay time and τ_{R} is the radiative decay time, which determines the value of PL quantum efficiency (η_{R}) as following:

$$\eta_R = \frac{1}{1+\frac{\tau_R}{\tau_{NR}}}, \tag{2.5}$$

from **Eq. (2.5)**, the radiative lifetime should be much shorter than non-radiative lifetime to achieve an efficient PL process.

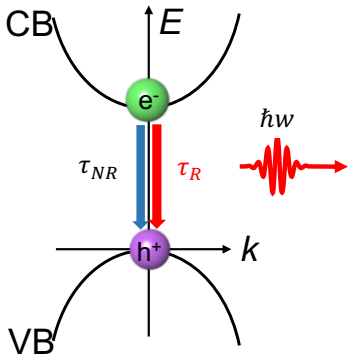

Figure 2.9. Schematic of PL process of exciton.

The PL intensity of TMDs has strong dependence on their thickness, because their band structures show in-direct to direct band gap transformation with the number of layers decreasing as discussed in **Section 2.1.1**[42,52,53].

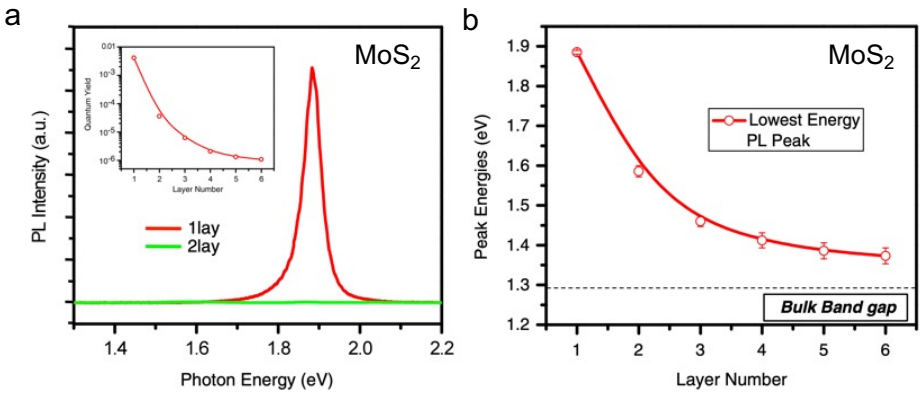

Figure 2.10. (a) PL spectra of 2L-MoS_2 and 1L-MoS_2. The inset presents the PL quantum efficiency with the layer number from 1 to 6. (b) Energy of peak A in MoS_2 with the layer number from 1 to 6. The dashed line indicates the bulk band gap (Reprinted with permission from Ref.[42]. © 2010 APS).

Figure 2.10a shows the PL spectra of monolayer (1L) and bilayer (2L) MoS_2. The dominant peak intensity at 1.9 eV is dramatically increased in monolayer MoS_2. The η_R of 1L-MoS_2 is over a factor of 10^4 compared with the bulk MoS_2. The peak position

shifts to higher energies with thickness decreasing[42]. Similarly, the results of thickness dependent PL intensity were observed in WS_2 and WSe_2[51].

The temperature dependent behaviors PL intensity of 1L-WSe_2 (WS_2) and MoS_2 ($MoSe_2$) are fundamentally different. **Figure 2.11a** presents the PL spectra of 1L-WSe_2 at various temperatures. The PL intensity of the dominant peak in 1L-WSe_2 increases with elevating the temperature. However, the PL intensity changes opposite in 1L-MoS_2 with increasing temperature. **Figure 2.11b** shows the integrated PL intensity of 1L-WSe_2 (red dots) and 1L-MoS_2 (blue dots). It shows the very clear difference between two monolayer samples because of effect of dark excitons. The PL intensity from bright excitons can be understood by the temperature dependence of radiative decay time ($\tau_R \propto T$)[54]. Therefore, the different temperature dependent PL intensity of 1L-WSe_2 can be explained by the emergence of dark excitons, which exists at the energy level below bright excitons.

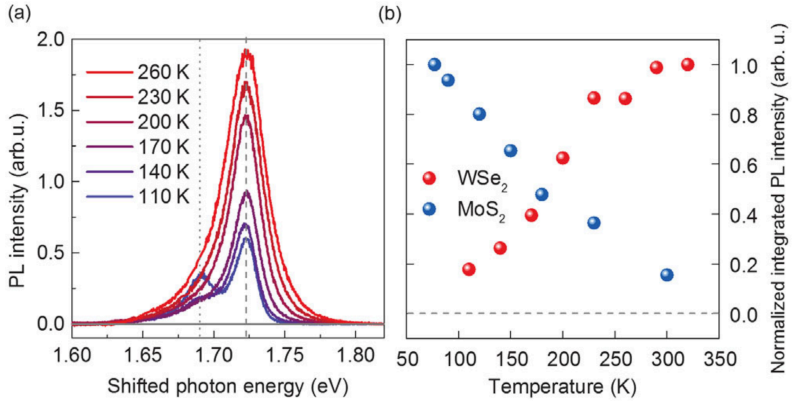

Figure 2.11. (a) PL spectra of suspended monolayer WS_2 from 110 to 260 K. (c) The temperature dependent normalized PL intensity of 1L-WSe_2 and MoS_2 as a function of temperature (Reprinted with permission from Ref.[54]. © 2015 APS).

2.2. Valley physics of 1L-TMDs

Similar to charge, and spin, "valley" as a new degree of freedom is possibly manipulated to store and carry information; it attributes to the novel electronic applications, which is well known as valleytronics[55,56]. The new materials for exploring valleytronics are crucial. These materials should have a band structure with

doubly- or more-degenerate but inequivalent valleys. The monolayer TMDs with broken spatial inversion symmetry breaking and strong spin-orbit coupling provide a good platform to explore the valley physics, and valleytronics applications. In the following sections, I will give a brief introduction to valley physics of monolayer TMDs.

2.2.1. Spin-valley coupling

At first, let us look at the structure of TMDs carefully. **Figure 2.12a** shows the crystal structure of 2*H*-phase bulk MoS_2 with a space group of D_{6h}^4, which keeps the spatial inversion symmetry. In contrast, monolayer MoS_2 belongs to D_{3h}^1 group, which breaks the spatial inversion symmetry as shown in **Figure 2.12b**. The 1L-MoS_2 has a band gap at the K+ and K– (K and –K are other symbols labelled by other papers[57]) points which are corners of Brillouin zone in **Figure 2.12b**. Using a two-band tight-binding model (massive Dirac fermion model), Hamiltonian of 1L-TMDs can be described as following[57]:

$$\hat{H} = at\left(\tau_v k_x \hat{\sigma}_x + \tau_v k_y \hat{\sigma}_y\right) + \frac{\Delta}{2}\hat{\sigma}_z - \lambda\tau\frac{\hat{\sigma}_z - 1}{2}\hat{s}_z, \tag{2.6}$$

where a is the lattice constant, t is the effective hopping integral, $\tau = \pm 1$ is the valley index, k denotes the relative crystal momentum, Δ is the band gap, $\hat{\sigma}$ is the Pauli matrices for basis functions, 2λ is the splitting at the top of VB due to spin-orbital coupling (SOC), and $\hat{s}_z$ is the Pauli matrices for spin projection along z direction. The last term is from SOC, which is attributed to the *d* orbital of Mo atoms[58]. The conduction band-edge is spin degenerate at K+ and K– points and the valence band-edge splits due to the strong SOC. Moreover, the splitting at K+ and K– valleys should be opposite because of the time-reversal symmetry, as schematically shown in **Figure 2.12c** and **Figure 2.13**[57]. The small splitting of conduction band is obtained by three-band tight binding model[59].

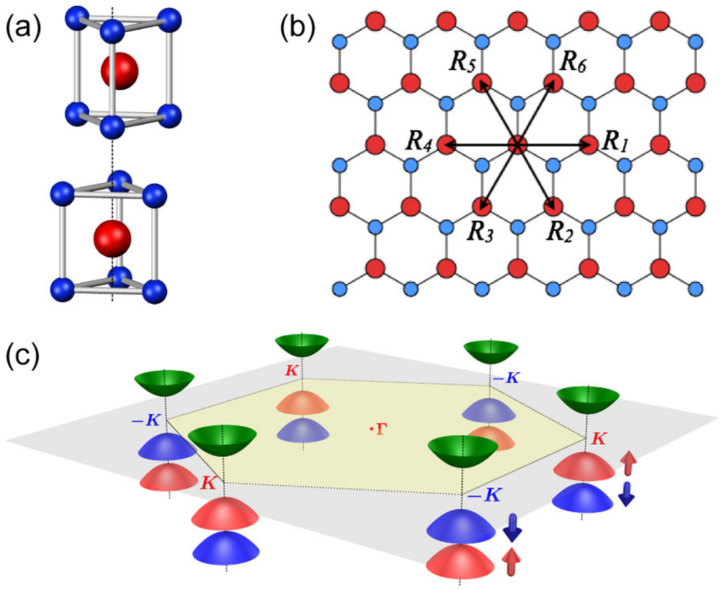

Figure 2.12. (a) Unit cell of bulk MoS_2 with 2*H* stacking order. (b) Top view of monolayer MoS_2. R_i (*i*=1−6) are the nearest vectors to Mo atoms. (c) Schematic image of band structure of monolayer MoS_2 at the band edges at K points. (Reprinted with permission from Ref.[57]. © 2012 APS)

The large splitting at the valence band was reported to be ~150 meV for MoX_2 and ~450 meV for WX_2[58]. The reversed spin splitting with the two doubly-degenerate valleys directly leads to the spin valley coupling (locking)[20,57]. The coupling of valley and spin requires a simultaneous spin flip in addition to a large momentum to transfer to conserve energy[60,61], which gives a rise to attractive phenomena[20].

2.2.2. Orbital magnetic moment and Berry curvature

The orbital magnetic moment is related to the valley pseudospin which is analogy to the bare magnetic spin linked to the real spin[62]. Two parts have contributed to the orbital magnetic moment, that are intracellular component stems and intercellular contributions. The first component is formed by the parent atomic orbitals. In monolayer-TMDs, the intracellular component origins from the hybridization of $d_{x^2-y^2}$ and d_{xy} orbitals ($d_{x^2-y^2} + \tau_v i d_{xy}$) with angular momentum l_z ($l_z = 2\tau\hbar$) for the valence band, while the hybridization of d_{z^2} orbitals with $l_z = 0$ for the conduction

band. The intracellular component stems mainly contribute to the value of valley Zeeman splitting, which will be explained detailly in next section. The second component arises from phase winding of Block states on the intercellular scale[63], which relates to the Berry curvature[62,64]. I will briefly introduce the concept in this section.

To simplify, the following discussion assumes that the intracellular circulation currents is absent in a nondegenerate band. Orbital magnetic moment contributed by the intercellular current circulation in the conduction band is described using $k \cdot p$ analysis as described below [65]:

$$m(k) = -i\frac{e\hbar}{2m_e^2}\sum_{i\neq c}\frac{p^{ci}(k)\times p^{ic}(k)}{\varepsilon_i(k)-\varepsilon_c(k)}, \tag{2.7}$$

where $p(k)$ is the interband matrix element of the canonical momentum operator, and $\varepsilon(k)$ is the band dispersion. The broken inversion symmetry again gives rise to finite Berry curvatures at the K± valleys, resulting in a finite valley Hall conductivity. The Berry curvature in the CB is described by[57,66]:

$$\Omega_c(k) = -i\frac{\hbar^2}{m_e^2}\sum_{i\neq c}\frac{p^{ci}(k)\times p^{ic}(k)}{[\varepsilon_i(k)-\varepsilon_c(k)]^2}, \tag{2.8}$$

the Berry curvature in the VB has the same value, but with the opposite sign. Moreover, due to the finite Berry curvature with opposite signs in K+ and K– valley, an in-plane electric field can be spontaneously produced, which is known as valley Hall effect, as an analogy of Hall effect in the classical picture.

The optical circular dichroism is related to orbital magnetic moment, and Berry curvature as following[66]:

$$\eta(k) = -\frac{m(k)\cdot\hat{z}}{\mu_B^*(k)} = -\frac{\Omega_c(k)\cdot\hat{z}}{\mu_B^*(k)}\frac{e}{2\hbar}[\varepsilon_i(k)-\varepsilon_c(k)], \tag{2.9}$$

where $\mu_B^*(k)$ is the effective Bohr magneton. From the relationship, it is noted that the valley contrasted optical circular dichroism is accompanied by valley contrasted contribution to Hall conductivity.

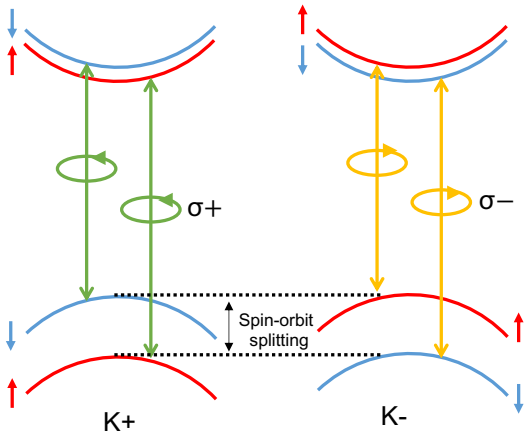

Figure 2.13. Spin-valley coupling with optical selection rule.

The orbital magnetic moment is coupled with circularly polarized light, giving a rise to the optical selection rule for interband transition[65]. The light with right helicity (σ^+) only couples to the K+ valley, while the light with left helicity (σ^-) only couples to the K– valley. In addition, because of the spin splitting of the valence-band, the valley optical selection rule becomes spin-dependent selection rules in monolayer TMDs as shown in **Figure 2.13**[57].

2.3. Optical control of valley polarization

As discussed above, the monolayer TMDs have doubly degenerated but inequivalent valleys, because of broken inversion symmetry and strong spin-orbit coupling. The excitons or trions at K+ and K– valley in monolayer TMDs have a valley degree freedom, which can be selectively excited by shining circularly polarized light, called as valley polarized excitons or trions. This has been demonstrated independently by different groups using optical excitation and detection of circularly polarized light[18,67,68]. The valley polarization defined by the difference between the population of two-valley (K+ and K–) excitons can be experimentally measured by the PL spectra with circularly polarized light, which is very important experimental technique in this PhD thesis. The valley polarization ρ can be described as:

$$\rho = \frac{I_{\sigma+} - I_{\sigma-}}{I_{\sigma+} + I_{\sigma-}}, \tag{2.10}$$

where $I_{\sigma+}$ and $I_{\sigma+}$ represent the PL intensity of valley excitons at K+ and K– valley, respectively. In an ideal case, the valley polarization can be unity under perfectly circular polarized light, and negligible valley scattering.

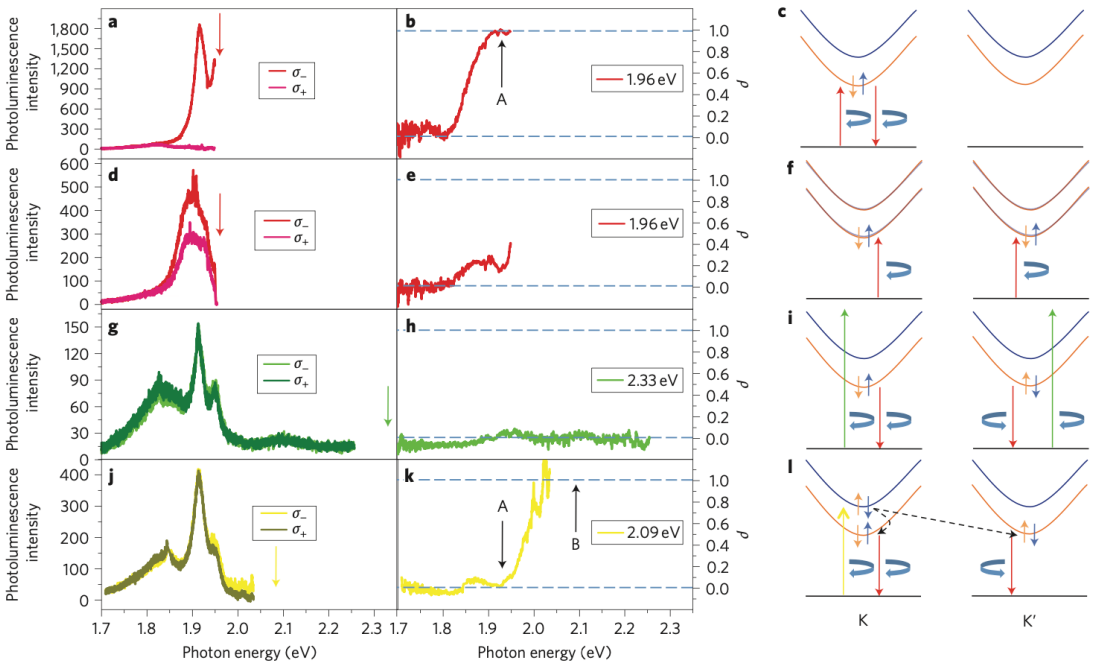

Figure 2.14. (a) PL spectrum of 1L-MoS_2 with excitation energy of 1.96 eV. The corresponding polarization as a function of photon energy is shown in (b). (i) Schematic diagram of valley excitonic states followed by optical selection role. (d-f) Results of bilayer MoS_2 with excitation energy of 1.96 eV. (g-i) Results of 1L-MoS_2 at 2.33 eV excitation. (j-i) Results of 1L-MoS_2 at 2.09 eV excitation. **(**Reprinted with the permission from Ref.[67]. © 2012 Springer Nature).

Moreover, the valley polarization shows resonant dependence in photon energy, as shown in **Figure 2.14**[67]. The resonances with *A* and *B* exciton are at around 1.9 and 2.1 eV, respectively. **Figure 2.14a, b** display the PL of 1L-MoS_2 and their valley polarization on resonance excitation with the *A* exciton[67]. The valley polarization of *A* exciton under this condition is near unity according to optical selection rule. **Figure 2.14j, k** show the results for the *B* exciton excited by 2.09 eV photon. Hot luminescence near the *B* exciton energy have the same helicity as the optical excitation[67]. However, the *A* exciton PL does not have valley polarization, which leads to the same population of band-edge holes at the two-valleys (K+ and K–) after relaxation from the *B* to *A*

exciton state, as shown in **Figure 2.14i**[67]. **Figure2.14g, h** present the results under 2.33 eV, which is higher than resonant energy of both *A* and *B* exciton. Therefore, no valley polarization is observed at all here.

2.4. Zeeman effect

2.4.1. Zeeman effect of atoms

Before discussing the valley Zeeman effect in TMDs, I will briefly give an introduction of Zeeman effect in atoms. The degenerated atomic energy level is split into several sublevels, when magnetic field (*B*) is applied to atoms. The splitting here is so-called Zeeman effect of atoms. The Zeeman effect is associated with quantum numbers of atoms which are orbital momentum *L*, spin momentum *S*, and total angular momentum *J*. The atomic level without magnetic field has degenerate energy levels with the number of M_J, which equals $2J+1$. **Figure 2.15** shows the example of $^2P_{3/2}$ energy levels of an alkali atom with and without magnetic field (*B*).

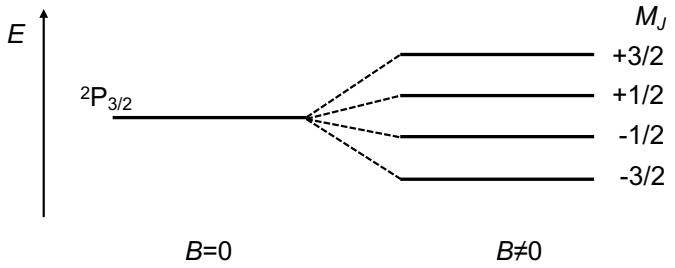

Figure 2.15. $^2P_{3/2}$ energy levels of an alkali atom without and with magnetic field.

The splitting energy of an atomic orbit under a magnetic field can be written as below:

$$\Delta E = -\mu B, \tag{2.11}$$

$$\mu = -g_J \mu_B M_J, \tag{2.12}$$

$$g_J = 1 + \frac{J(J+1)+S(S+1)-L(L+1)}{2J(J+1)}, \tag{2.13}$$

where μ is the magnetic moment of the atomic orbit, B is the out-of-plane

projection of the magnetic field, μ_B is the Bohr magneton, g_J is the Landé g-factor and M_J is the number of degenerate state. Hence, we can get:

$$\Delta E = g_J \mu_B M_J B, \tag{2.14}$$

2.4.2. Valley Zeeman effect of 1L-TMDs

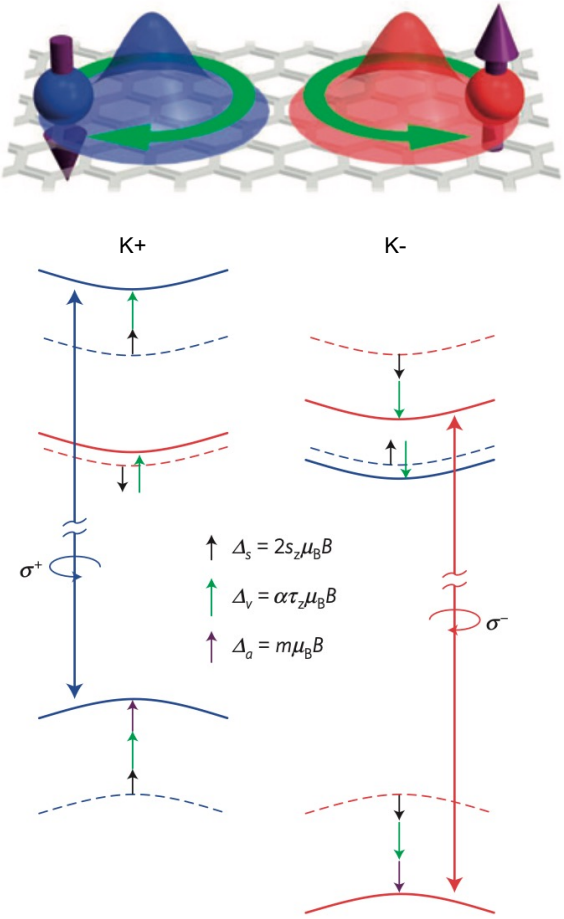

Figure 2.16. Top figure shows the schematic of valley magnetic moment. Blue (red) represents spin up (down) in K+ (K−) valleys. The magnetic moment also attributes to the atomic orbital for holes (purple arrow), which has opposite sign in the K+ and K− valleys. Bottom gives energy level diagram, which presents the three factors to the valley Zeeman shifts (black: spin, green: valley, purple: atomic orbital). Reprinted with permission from Ref.[62]. © 2015 Springer Nature.

Three factors should be considered to give a total Zeeman splitting of valley, which are from spin magnetic moment, atomic orbital, and "valley magnetic moment"

contributed from the self-rotation of the wavepacket[62,64,69], as shown in **Figure 2.16**. The contribution of spin magnetic moment shown by the black arrows can be neglected because optical transitions conserve spin. The atomic orbital contributes to the value of Zeeman splitting as indicated by purple arrow. As discussed in **Section 2.1.1**, the valence band is mainly composed of *d* orbitals with m= 2 for K+ and m= –2 for K– valley, respectively. The valence band shift with $\Delta a = 2\tau\mu_B B$ ($\tau = 1$ for K+ valley and $\tau_v = -1$ for K– valley). In the case of conduction band, it is mainly made of *d* orbitals with m= 0 for both valleys. Therefore, the splitting for the contribution band from atomic orbitals is $-4\mu_B B$, which is linear with *B*. In the case of valley magnetic moment contribution, the valley Zeeman shift for each band is given by $\Delta = a_i\tau\mu_B$. Here a_i is the valley *g*-factor for band *i* (*i* means conduction or valence band) depending on the value of m_o/m^*, where m^* is the effective mass of electron (hole).

The energy difference between two-valleys can be roughly described by[62]:

$$\Delta_v(\mathrm{K}+) - \Delta_v(\mathrm{K}-) = 2\left(\frac{m_0}{m_e^*} - \frac{m_0}{m_h^*}\right)\mu_B B. \tag{2.15}$$

In the massive Dirac fermion model, the effective mass of electron and hole are the same, which gives an identical contribution of intercellular magnetic moment. In this approximation, the valley magnetic moment would not affect the exciton resonances[62,69]. However, in more general hopping model, the effective mass of electron and hole is no more identical, resulting in the contribution of valley magnetic moment to valley Zeeman splitting[70].

From experiments such as PL measurements, the valley Zeeman splitting can be estimated by the peak energy difference of excitonic states using the following equation:

$$\Delta_v = E(K+) - E(K-), \tag{2.16}$$

here, $E(K+)$ and $E(K-)$ represent the peak energy of excitonic states at K+ valley and K– valley, respectively.

Similarly, the *g*-factor of valley excitons could be defined as bellow:

$$g_v = \frac{2[E(K+) - E(K-)]}{\mu_B B}, \tag{2.17}$$

the *g*-factor is calculated to be –4, expected to the *d*-orbital contribution to valley Zeeman splitting, consistent with experimental value[70].

Figure 2.17a shows the PL spectra of 1L-$MoSe_2$ under 0, 6.7 and −6.7 T. Clearly, the PL spectra of 1L-$MoSe_2$ with σ+ and σ– component corresponding to K+ valley and K– valley exciton, respectively are identical without magnetic field. At 6.7 T, the peak position of excitons (X) and trions (T) have a red-shift for K+ valley and move to a blue-shift for K– valley. On the contrary, the shift of excitonic states at two valleys under –6.7 T is reversed. **Figure 2.17b** presents the valley splitting energies of exciton and trion as a function of magnetic field, indicating the linear change. The slope is estimated to be –0.22±0.01 meV/T, corresponding to the *g*-factor of –3.8±0.2, which is close to the value of *g*-factor from atomic orbitals of -4.

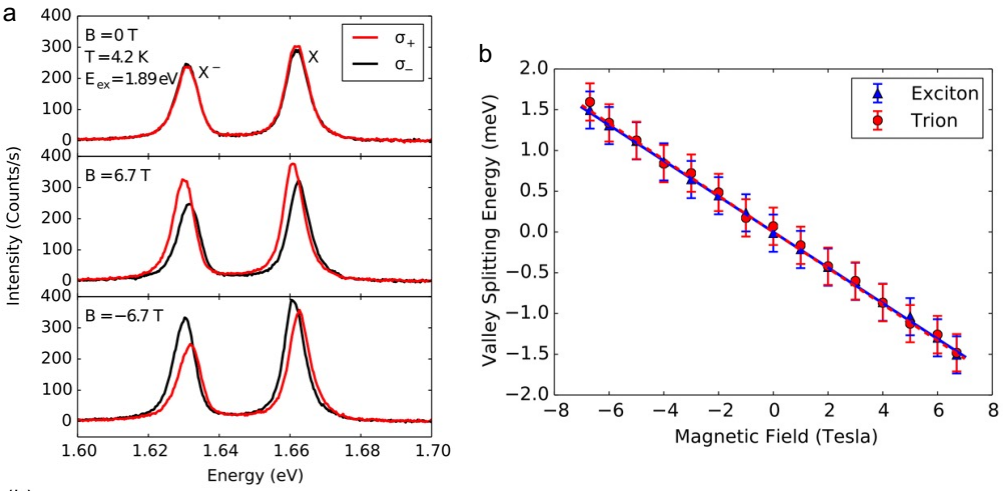

Figure 2.17. (a) PL spectra of 1L-$MoSe_2$ at various magnetic fields. (b) Peak energy differences of two-valleys as a function of magnetic fields. Reprinted with permission from Ref.[69]. © 2015 APS.

2.5. Van der Waals heterostructures

Different 2D materials can be mechanically stacked together by van der Waals force to make artificial heterostructures, as shown in **Figure 2.18**, which gives a rise to very interesting physical phenomena, and device applications.

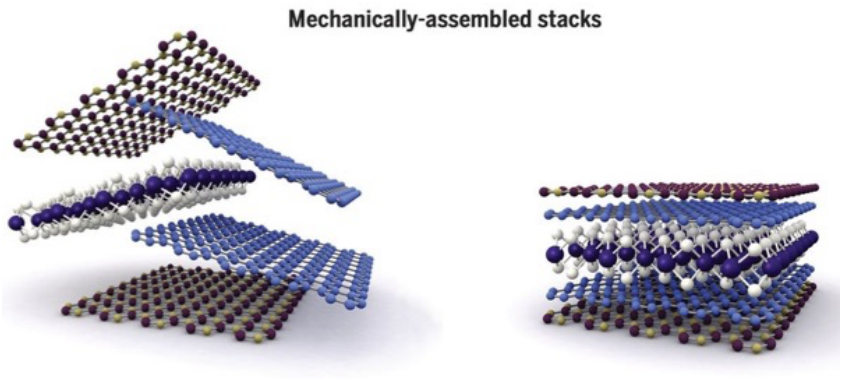

Figure 2.18. Van der Waals heterostructures by mechanically stacking. Reprinted with permission from Ref.[71]. © 2016 Springer Nature.

In this section, I will introduce two typical effects that occur in van der Waals heterostructures based on 1L-TMDs which are the focus of my PhD research.

2.5.1. Magnetic proximity effect

As introduced previously, the valley degeneracy of 1L-TMDs can be lifted with applying out-of-plane magnetic field. However, the valley Zeeman splitting is limited in this approach, which impedes the controlling of valley polarization for valleytronics application. An effective solution to the problem of small valley polarization or valley splitting is to utilize the magnetic proximity effect. The magnetic proximity effect introduces an exchange magnetic field from a ferromagnetic substrate to a monolayer TMD on top, which enhances the valley magnetic response[19]. The magnetic exchange fields with value up to ~10 T from EuS or CrI_3 substrate imposed on monolayer WSe_2 have been reported[72,73], where EuS and CrI_3 are ferromagnetic insulators.

Figure 2.19a, b shows the schematic diagram of the magnetic proximity effect of WSe_2/EuS heterostructure. With the ferromagnetic substrate, the addition magnetic spins from EuS to WSe_2 are highlighted in red arrows due to the magnetic proximity effect. **Figure 2.19c** shows the valley Zeeman splitting in WSe_2 as a function of magnetic field on EuS and on Si/SiO_2. The valley splitting in WSe_2 on EuS is enhanced significantly and deviates from linear dependence as a function of applied magnetic field *B*.

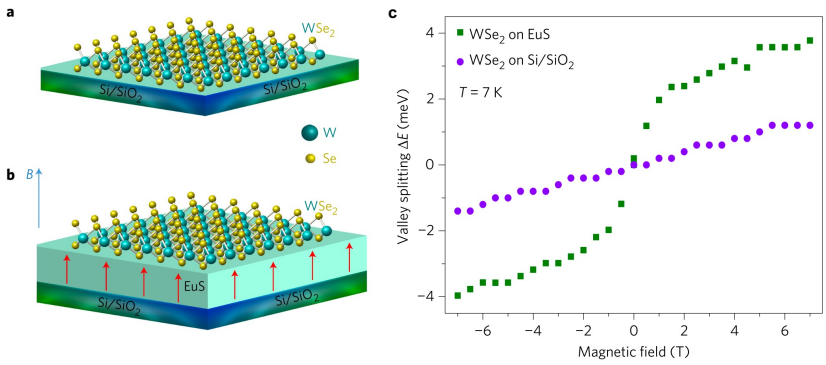

Figure 2.19. (a) Schematic diagram of WSe_2 on Si/SiO_2. (b) Schematic diagram of WSe_2 on ferromagnetic EuS substrate. (c) Valley splitting of excitonic peak as a function of magnetic field of WSe_2 on EuS (green) and on Si/SiO_2 (purple). Reprinted with permission from Ref.[72]. © 2017 Springer Nature.

2.5.2. Moiré excitons

Moiré excitons refer to the excitons confined in periodic moiré potential, which could be realized in van der Waals heterostructures with a twisted angle or lattice mismatch, as illustrated in **Figure 2.20a**. Three typical types of band alignments (straddling/type-I, staggered/type-II, and broken/type-III) can be formed in heterostructures. Moiré pattern in heterostructures by stacking two different 1L-TMDs heterostructures is usually accompanied with type II band alignment[74] (staggered gap), as shown in **Figure 2.20b,c**. The moiré period (λ) varying from several nanometers to tens of nanometers is given by following[23]:

$$\lambda = \frac{\alpha_{top}\alpha_{bottom}}{\sqrt{\alpha_{top}^2+\alpha_{bottom}^2-2\alpha_{top}\alpha_{bottom}\cos\theta}}, \quad (2.18)$$

α_{top} and α_{bottom} are lattice constant of top and bottom layer of heterostructure, and θ is the relative twist angle. It is well known that interlayer excitons usually formed in TMD heterostructures with staggered type II band alignment, because the excitons are composed of electrons and holes separated in two different layers[75]. Both interlayer (electron and hole in different layer) and intralayer excitons (electron and hole in same layer) could be trapped in moiré potentials, which leads to the formation of moiré excitons.

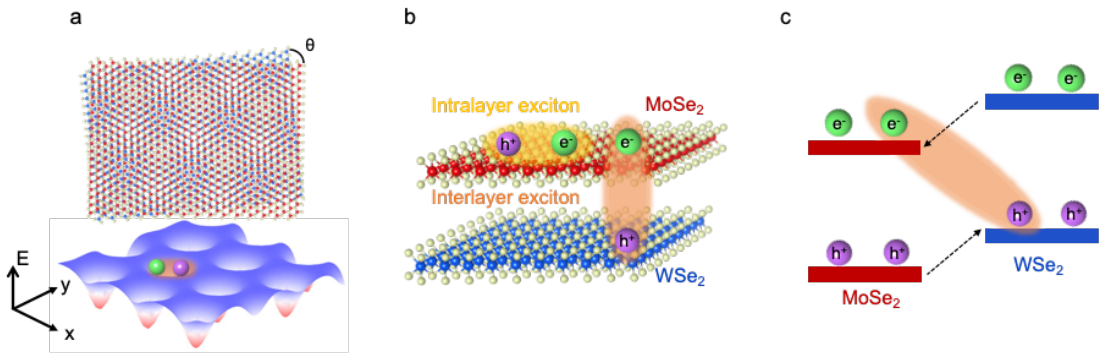

Figure 2.20. (a) Top: moiré pattern formed by stacking of two different 1L-TMDs with a twisted angle (θ). Bottom: excitons trapped in periodical moiré potential (moiré excitons). (b) Vertically stacking of $MoSe_2$ and WSe_2 with the schematic diagram of interlayer excitons and intralayer excitons. (c) Type II band alignment of $MoSe_2/WSe_2$ heterostructure.

The PL spectra from moiré excitons show extremely narrow peaks under low power excitation condition. **Figure 2.21a** shows the typical PL spectra of interlayer moiré excitons in $MoSe_2/WSe_2$ heterostructure with a twisted angle of 2° under 10 μW (red) and 20 nW (blue). Under low power excitation condition, the typical linewidth observed is on the order of 0.1 meV, suggesting there exists confined moiré potentials[30]. In contrast, the PL spectrum under high excitation power condition, a broad peak has been observed, because ensemble average from many moiré excitons with Gaussian distribution in energy were attributed to the PL spectra. Moreover, another characteristic of PL from the moiré excitons is the strong dependence on twisted angle. As shown in Figure **2.21b**, the PL intensity of moiré interlayer excitons of heterostructure with twist angle of 2° around 1.3 to 1.4 eV is much stronger than that with 20°. This behavior can be explained by the large momentum mismatch of the first Brillouin zone corners between CB and VB in 20° heterostructures, which suppresses the PL quantum yield. These studies opened the door to study quantum physics with moiré excitons, showing the potential in quantum information and nanophononics applications. Moreover, moiré systems have provided a novel way to combine different layered materials together. For example, the combination of 1L-TMDs and layered magnetic materials might pave the way to engineer the magnetic moiré excitons.

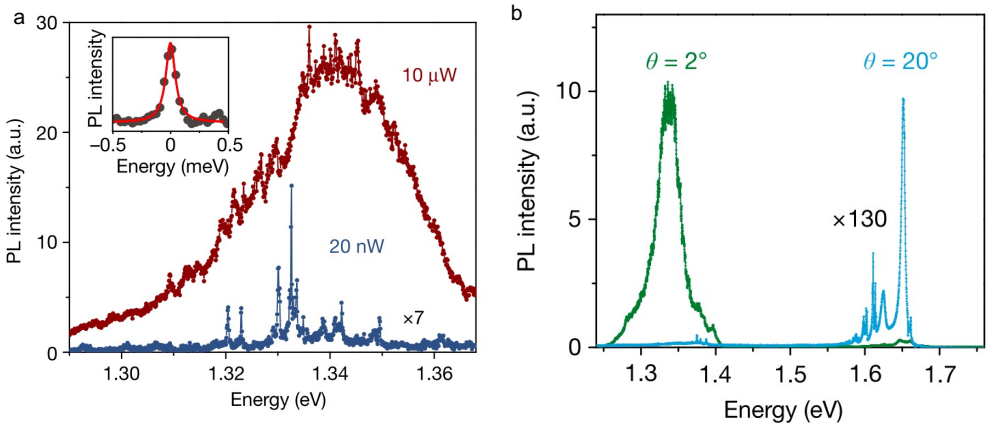

Figure 2.21. (a) PL spectra of interlayer moiré excitons in $MoSe_2/WSe_2$ heterostructure with a twisted angle of 2° under 10 μW (red) and 20 nW (blue). (b) PL spectra of moiré interlayer excitons of heterostructure with 2° (green) and 20° (sky-blue). Reprinted with permission from Ref.[30]. © 2016 Springer Nature.

Chapter 3. Experimental methods and setups

3.1. Introduction

In this chapter, I will introduce the methods of sample preparation and the optical setups, which are used through this PhD thesis.

3.2. Sample preparation

3.2.1. Monolayer fabrication

Bulk crystals were mechanically exfoliated to obtain their monolayer TMD samples. This method is well known as "scotch-tape" technique. The only necessary instruments used are bulk single crystals and adhesive tape.

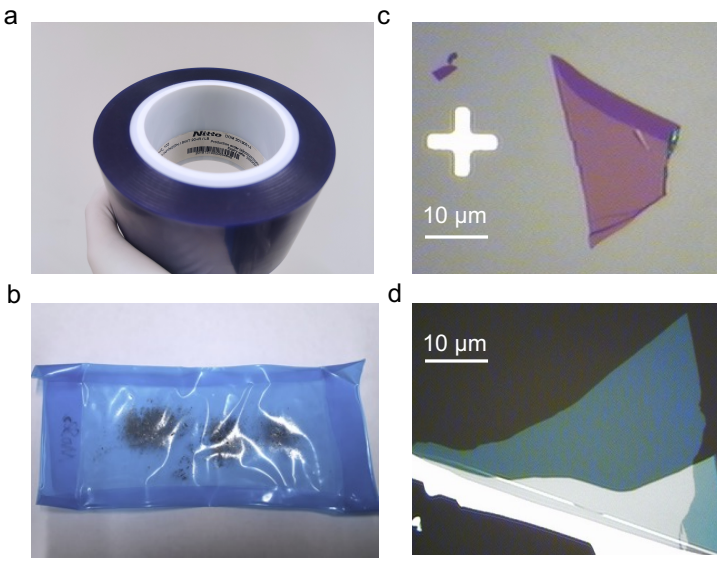

Figure 3.1. (a) Photograph of blue tape. (b) Exfoliated $MoSe_2$ flakes on the blue tape for exfoliation. (c) Fabricated monolayer $MoSe_2$ on SiO_2/Si substrate. (d) Fabricated monolayer $MoSe_2$ on PDMS film.

In this thesis, all monolayer or thin layer samples were fabricated mechanically using a blue tape (Nitto, SWT 20+R/LB), as shown in **Figure 3.1a**. The single bulk crystals of $MoSe_2$ and $MnPS_3$ were purchased from the company of hq graphene and 2D semiconductors, respectively. The high-quality crystals of *h*-BN were synthesized

using high pressure method by the groups of Dr. Kenji Watanabe and Dr. Takashi Taniguchi in national institute of material science (NIMS), Japan[76]. Prof. Yutaka Moritomo in Tsukuba University, Japan provided single crystals of $(La_{0.8}Nd_{0.2})_{1.2}Sr_{1.8}Mn_2O_7$ (Mn oxide) fabricated by floating-zone method[77]. The small pieces of flake on this blue tape (**Figure 3.1b**) were subsequently transferred on SiO_2/Si substrates with thickness of SiO_2 with a thickness of 270 nm or polydimethylsiloxane (PDMS) film (Gel-pak, GEL-FILM PF-20/17-X4). **Figure 3.1c, d** show the typical optical images of monolayer $MoSe_2$ on SiO_2/Si substrates and PDMS film, respectively.

After depositing some flakes onto the substrate, finding monolayer is necessary because monolayers are randomly distributed on the substrates, where the flakes with various thicknesses such as a few layers and thicker bulks exist. The optical contract, PL spectra, and height profile in AFM measurements are used to identify the monolayers. The setup used here will be described in detail in **Section 3.3**.

3.2.2. Heterostructure preparation

Two methods for preparation of vdW heterostructure samples are conducted thought out the studies of PhD thesis.

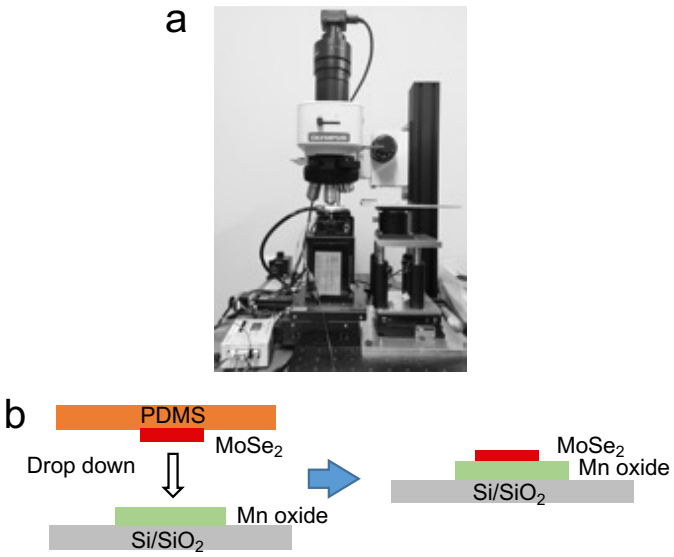

Figure 3.2. (a) Image of transfer setup. (b) Detail process of dry-transfer method using PDMS film.

Figure 3.2 shows the process of the first technique, called as "dry-transfer method", which is used for preparing the *h*-BN encapsulated monolayer $MoSe_2$ heterostructure in **Chapter 4**, 1L-$MoSe_2$/Mn oxide with *h*-BN spacer and other heterostructures in **Chapter 5**. **Figure 3.2a** shows the optical image of transfer setup. For instance, **Figure 3.2b** presents how to make 1L-$MoSe_2$/Mn oxide sample using this method. The Mn oxide fabricated by mechanical exfoliation is directly prepared on the SiO_2/Si substrate, while 1L-$MoSe_2$ is fabricated on the PDMS film. Then, 1L-$MoSe_2$ on PDMS is transferred onto the surface of Mn oxide.

The detail process of second method is explained in **Figure 3.3**, which is known as "viscoelastic dry-transfer technique". Compared with the previous way (dry-transfer method), the higher quality of vdW heterostructures can be prepared in **Chapter 6**. The impurities between layers can be reduced in this method, because the active surfaces of layers no more contact the polymer[78]. As demonstrated in **Figure 3.3**, the poly-procarbonate (PPC) is spin-coated on the PDMS to pick up and release few layers or monolayer two-dementional materials exfoliated mecanically on the SiO_2/Si substrates. After the sequentional pickup of a few (mono) layer, the PPC and PDMS are then removed by imersing them in acetone solution.

The heterostructure samples are thermally annealed at ~ 150 °C for 1 h in Ar/H_2 (97%/3%) forming gas for a good contact between each layer.

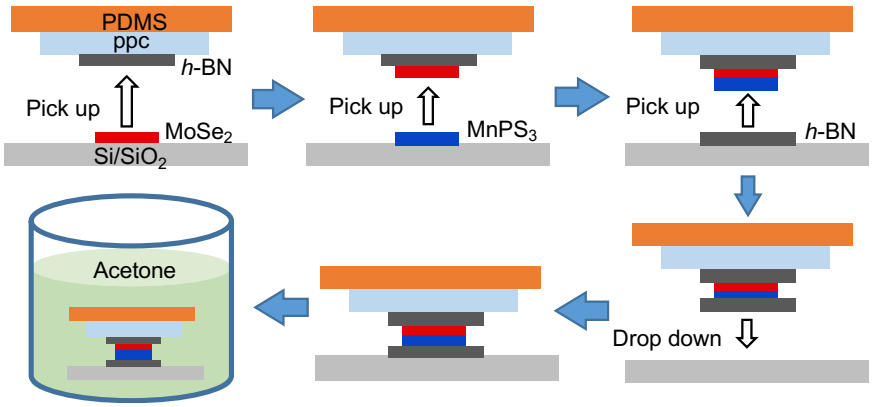

Figure 3.3. Schematic of "viscoelastic dry-transfer technique". After the sequentional pickup of a few (mono) layer, the polymer layers were then removed by imersing them in acetone solution.

3.3. Experimental setup

3.3.1. Micro-Raman spectroscopy system

The identification of 1L-TMDs from their optical contract and their typical PL spectra are conducted by commercial Micro-Raman spectroscopy system (Nanophoton, RAMAN touch). **Figure 3.4a** shows the photograph of Nanophoton, RAMAN touch. The right-side image is the inside of the part highlighted in orange line, which is controlled by the software (Raman viewer) installed in the computer. **Figure 3.4b** gives a schematic of optical pass of the Nanophoton, RAMAN touch. The semiconductor laser (532 nm) is used here to excite the samples with equipment of confocal slit, cooled CCD and spectrometer to obtain high resolution PL and Raman scattering spectra, which would provide the information the layer number of TMDs.

Moreover, the temperature-dependent PL spectra and Raman scattering measurement in **Chapter 5** and **Chapter 6**, respectively, are taken by this setup with liquid helium cooled cryostat to control the sample temperature.

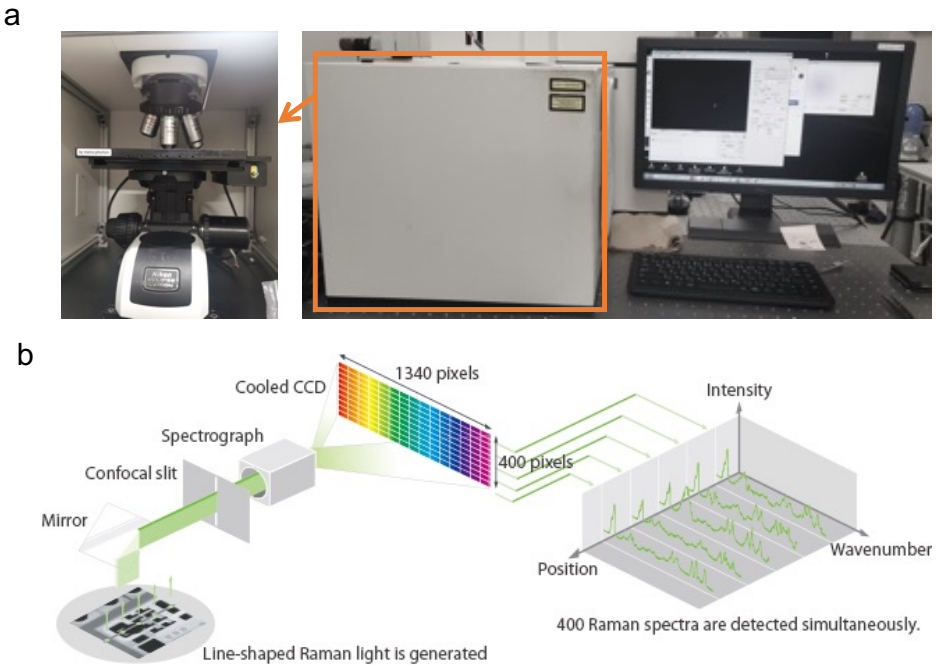

Figure 3.4. (a) Optical image of Nanophoton, RAMAN touch. (b) Schematic of optical pass inside the Nanophoton, RAMAN touch. Taken from Ref.[79].

3.3.2. Atomic force microscope measurement

Atomic force microscope (AFM) measurement was used to detect the thickness of *h*-BN spacers in **Chapter4, 5** and check the surface roughness of Mn oxide in **Chapter 5**. The image of AFM (SII, Nano Navi IIs, Nanocute) equipped with self-sensitive micro cantilever (PRC-DF40P) is shown in **Figure 3.5a**. **Figure 3.5b** presents the typical AFM image of *h*-BN layer with the scale bar of 200 nm. The line-cut along the white line in **Figure 3.5b** is shown in **Figure 3.5c**. Two-plateaus with slight fluctuations are observed here, which correspond to the surface of *h*-BN and SiO_2/Si substrate, respectively. I can estimate the thickness of the *h*-BN layer to be 3.8 nm from the height difference between two plateaus.

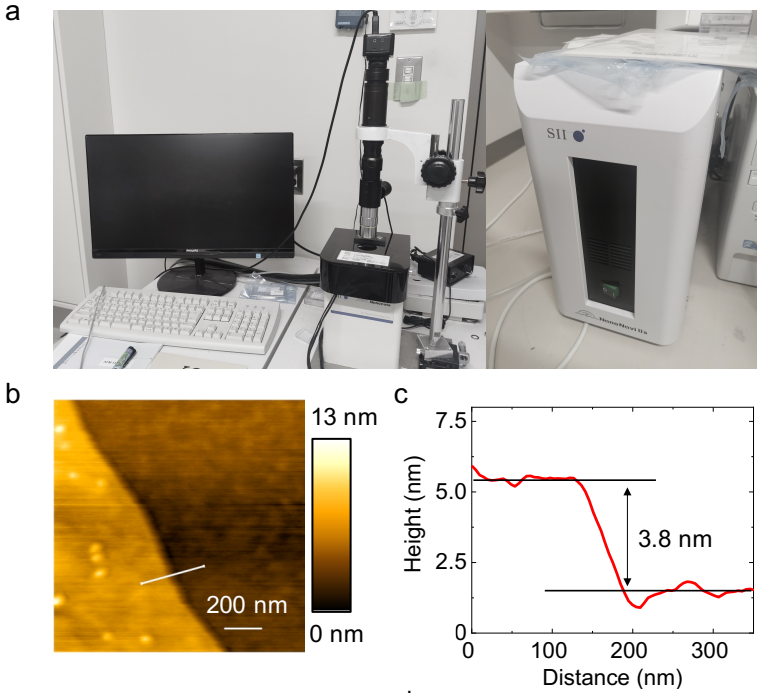

Figure 3.5. (a) Photograph of AFM measurement. (b) AFM image of *h*-BN. (c) AFM height profile of *h*-BN along the white line in the image of (b).

3.3.3. Circularly polarized PL spectra measurement under magnetic field

Figure 3.6. Photographs of the home-made setup of optical measurement under magnetic field. The photographs of compressor for He circulation and electrical circuit for generation of magnetic field are shown.

Circularly polarized PL spectra under magnetic field throughout the thesis (**Chapter 4-6**) were measured using home-made optical setups as shown in **Figure 3.6**. The optical pass of the setup is exhibited in **Figure 3.7**. The samples are set into the cryostat (ST-500, Janis), which is controlled by the cooled system with liquid helium (RH100, Air liquid) and temperature controller (Model 34, Cryo·con). The magnetic field ranging from −7 to +7 T is applied perpendicular to samples surface (Voight configuration). The continuous wave He-Ne laser (633 nm) is used for a light source to optically excite the sample. The neutral density (ND) filter after the laser source is to adjust the laser power on the samples. The quarter-wave (λ/4) plate is used to create circularly polarized light (σ+ or σ−) before objective lens (×100, NA=0.5, M Plan Apo NIR, Mitutoyo). Circularly polarized light selectively excites valley exciton of 1L-$MoSe_2$, because σ+(σ−) light excites the excitons in K+(K−) valley according to the optical valley selection rule, as explained in **Chapter 2**. However, the PL signals corresponding to σ+(σ−) circular polarized component from K+(K) valleys can be detected because of intervalley scattering between K+ and K−, and vice versa. The

signals from K+(K−) are selectively detected using polarization sensitive measurements. By rotating the half wave plate (λ/2), the PL signal can be selectivly chosen. The circularly polarized PL signals are converted to linearly poralized light with passing the quarter-wave plate after objective lens and selectively detected by passing the linear polarizer. The long pass filter (650 nm) is used for removing the strong exitaion laser light. Then, the PL signals from each valley are focused by lens (*f*=100 mm), and detected by spectrameter (Kymera 193i, Andor) equipped with a pertiler cooled CCD camera (DR-316B-LDC-DD, Andor).

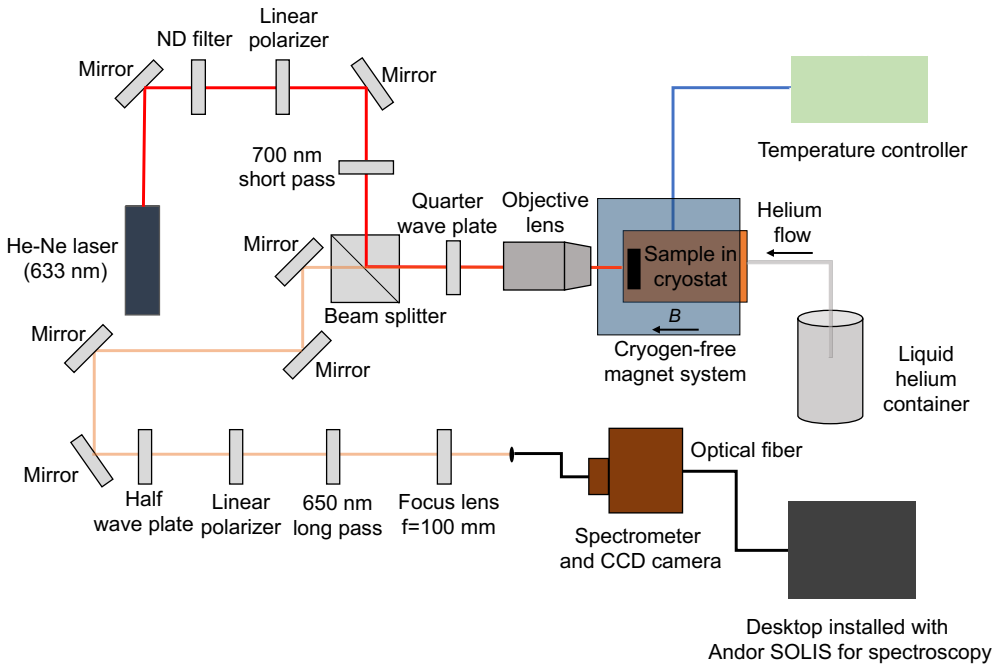

Figure 3.7. Schematic of the circularly polarized PL measurement under magnetic field.

3.3.4. Time-correlated single photon counting

Time-correlated single photon counting (TCSPC) is powerful technique among time resolved measurements, which will provide us the information of ultra-fast excitonic (carriers, excitons, trions and so on) dynamics with recording the intensity profile of emitted photons from materials in time-domain. **Figure 3.8** shows the schematic diagram of TCSPC measurement. As illustrated, single photons are repetitively emitted from sample during the reference time of periodic trigger pulse, which can be tagged like a stopwatch with a period from start to stop. After

accumulation of many repetitive cycles (events), histogram of a single photon emission is formed as shown in the final step of the process in **Figure 3.8**.

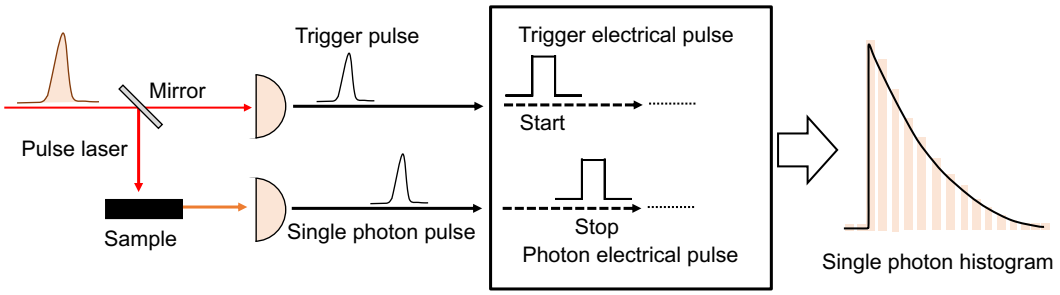

Figure 3.8. Schematic diagram of fundamentals of TCSPC measurement.

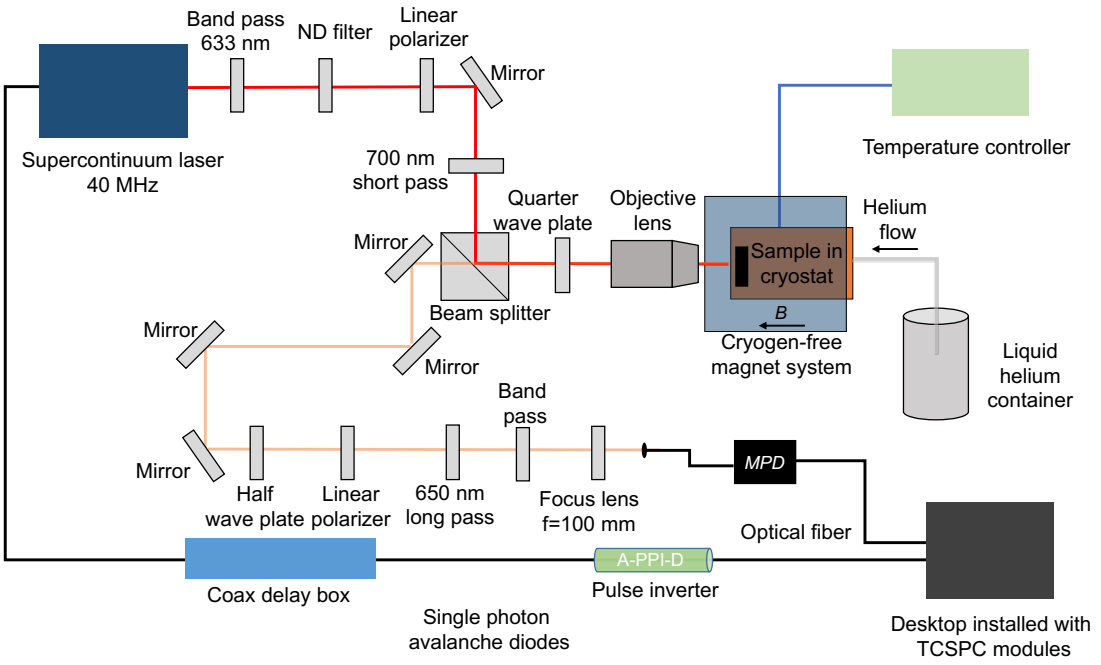

Figure 3.9. Schematic diagram of optical pass of home-made TCSPC measurement setup under magnetic field.

I have built up the TCSPC setup for time-resolved PL measurements in **Chapter 4,** as shown in **Figure 3.9**. A supercontinuum laser with pulse width of ~ 20 ps and reptation rate of 40 MHz (NKT photonics, Extream-K) is used as a light source. A linear polarized light with excitation energy of 1.96 eV is generated using the band pass filter with a bandwidth of 633 nm and linear polarizer. The objective lens (×100, NA=0.5, M Plan Apo NIR, Mitutoyo) is used for this measurement. The PL decay signals of trions and excitons are selectively detected using Si avalanche photodiode (MPD, SPD-

050-CTD-FC) through a bandpass filter with a bandwidth of 760 nm and a bandpass with a bandwidth of 750 nm, respectively. Instrumental response function (IRF) of TCSPC setup caused by the timing uncertainty of detector introducing conversion from a photon to an electrical pulse, i.e., timing-jitter is measured to check the resolution of this TCSPC setup.

In **Chapter 6**, Fourier interferometer (Gemini, NIREOS) is employed between sample and Si avalanche photodiode, which can map the PL signals from samples as a function of emission wavelength (energy) and decay time. That means that the interferometer and TCSPC give spectral- and time-resolved data. The variable spectral resolution is beneficial to measure ultra-narrow peak signals without band pass filter. The basic principle will be given, as described below.

Two replica rays of lights with changeable delay are created in the interferometer. The output spectrum is obtained from the Fourier transform of the output light, where the output spectrum is modulated at a tunable frequency by changing the delay time. The light intensity depending on the delay time between replicas at the detector is known as interferogram, from which the retrieved spectrum is obtained by the Fourier transform[80].

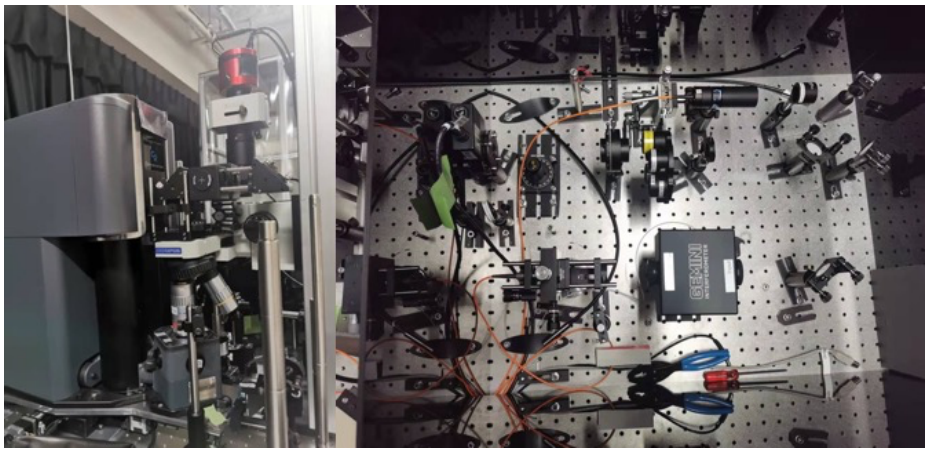

Figure 3.10. Photographs of the home-made setup of optical measurement of TCSPC with Gemini and first-order correlation measurement.

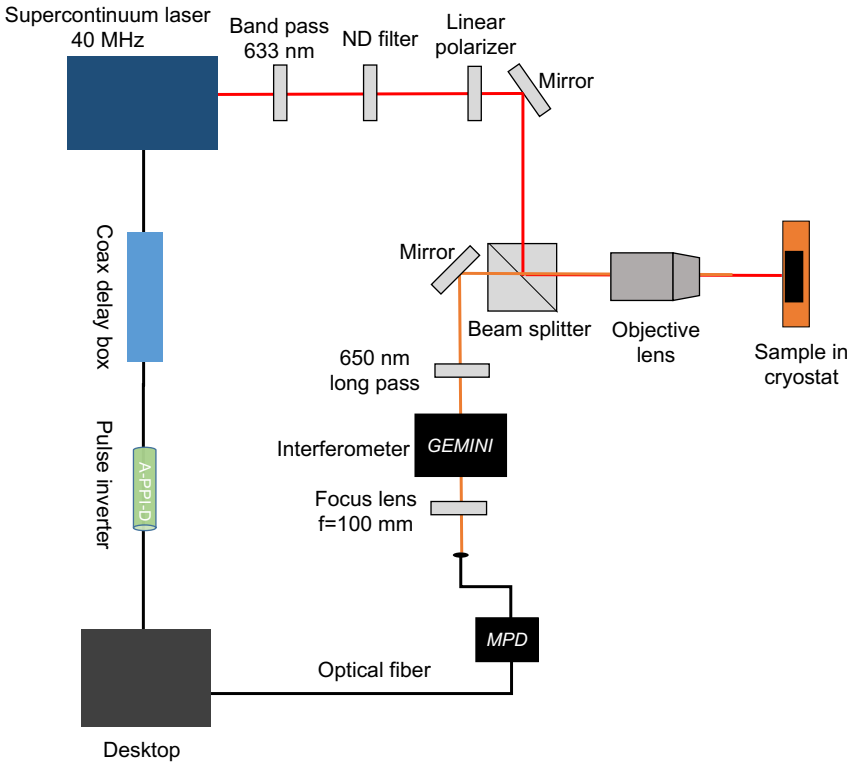

Figure 3.11. Schematic of combined setup of interferometer and TCSPC system for spectral and time-resolved PL profiles.

Figure 3.10 presents the photographs of the home-made setup of optical measurement of TCSPC with Gemini. **Figure 3.11** shows the schematic setup of combination of interferometer and TCSPC system. The sample is put in a cryogen-free cryostat (Cryostation C2, Montana Instruments). The interferometer is installed before the single photon avalanche diode to obtain the PL intensity decay map.

3.3.5. First-order correlation PL measurement

The first-order correlation function $g^1(\tau)$ of PL signals is recorded by inserting an interferometer before the monochromator, from which dephasing time (coherence time) T_2 can be estimated. T_2 is described as follows:

$$\frac{1}{T_2} = \frac{1}{2T_1} + \frac{1}{T_2^*}, \tag{3.1}$$

where T_1 is the energy relaxation time, and T_2^* is the pure dephasing time. The first term on the right-hand side represents the dephasing of population decay, which can be

experimentally obtained from the TCSPC measurement. The second term means the dephasing by the population conserving scattering.

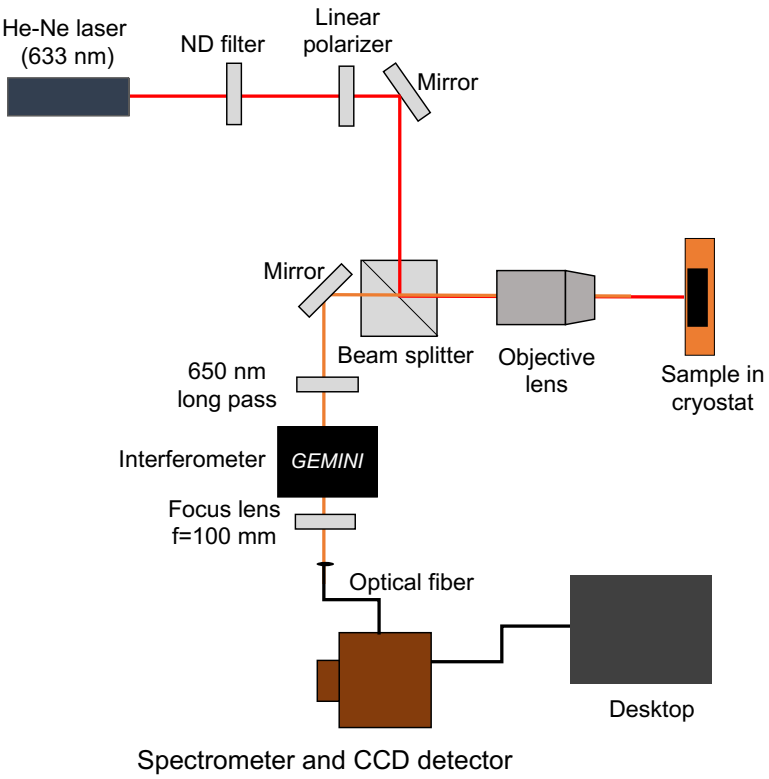

Figure 3.12. Schematic of optical setup of the first-order correlation measurement.

Figure 3.12 shows the schematic of optical setup of the first-order correlation measurement. The He-Ne laser of 633-nm (LGK7665P, LASOS) is used here as a light source. The signal is detected by spectrameter (Spectrapro 2300i, Acton Research Corporation) equipped with a cooled charged-coupled CCD camera (Spec-10, Acton Research Corporation). This setup is used for **Chapter 6**.

3.3.6. Temperature- and polarization-dependent PL measurements

The temperature- and power-dependent PL spectra of **Chapter 6** are obtained using the setup as shown in **Figure 3.13**. The sample is put in the cryogen free cryostat (ST-500, Janis) connected with air cooled compressor (CAN-11, Sumitomo) and temperature controller (9700, Scientific Instrument). The excitation wavelength of single mode fiber coupled laser (CivilLaser, 80 mW) is 635 nm, and the objective lens

(SL × 100, NA=0.55, Mitutoyo) is used here. The PL signals are detected by spectrameter (Spectrapro 300i, Acton Research Corporation) equipped with a cooled charged-coupled CCD camera (Spec-10, Acton Research Corporation). The temperature is controlled by temperature controller from 10 to 300 K. The excitation power is modulated by rotating the half-wave (λ/2) plate. The laser is focused on the sample surface using a 100× objective lens with a spot size of ~1.5 μm.

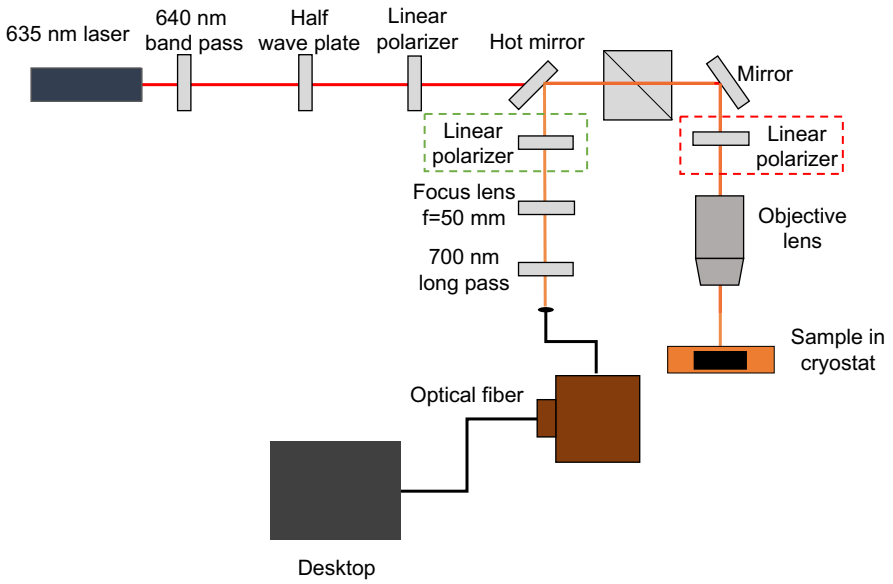

Figure 3.13. Schematic of optical setup of temperature-, and polarization dependent PL measurements

3.3.7. Linearly polarized PL measurements

The linearly polarized PL spectra in **Chapter 6** are also measured by the setup in **Figure 3.13**. There are two types of measurement configuration: one is to change the excitation polarization direction by rotating the half-wave (λ/2) plate in green dotted line, and the other is to change the detection polarization direction in red dotted line.

Chapter 4. Magnetic field induced inter-valley exciton and trion dynamics in 1L-$MoSe_2$

4.1. Introduction

External fields such as electric[81–84] and magnetic field[27,69,85–91] have been applied to extensively study valley polarization of 1L-TMDs. The lifting of valley degeneracy caused by time-reversal symmetry breaking under magnetic field gives a rise to the splitting of exciton or trion PL peak with σ^+ and σ^- circularly polarized light, corresponding to population of exciton or trion at K+ and K– valleys, respectively. The splitting is named as valley-Zeeman splitting in 1L-TMD, which was discussed in **Section 2.4**. The excitonic valley polarization could be dominated by the dynamics as following: the generation of valley-polarized excitons (trions); intra-and inter-valley relaxation of excitons (trions). The dynamics of valley polarization in lifting valley degenerate conditions without magnetic fields have been explored using ultrafast Faraday and Kerr rotation[92–96], polarization-resolved PL[97,98], and pump-probe spectroscopy[99–101]. However, dynamics of excitonic valley polarization under magnetic field have not been studied systematically. In this chapter, I will systematically introduce the dynamics of excitonic valley polarization in *h*-BN encapsulated 1L-$MoSe_2$ using polarization- and time-resolved PL spectroscopy under magnetic field.

4.2. Polarization-resolved PL spectra

Figure 4.1a shows the optical image of encapsulated 1L-$MoSe_2$ in *h*-BNs. The detail fabrication process was shown in **Chapter 3.** The 1L-$MoSe_2$ is shown in red, and top and bottom *h*-BN are shown in yellow and purple, respectively. The thickness of top and bottom layer of *h*-BN are determined by AFM (**Figure 4.1b**). Both are 14 nm as shown in **Figure 4.1c, d**.

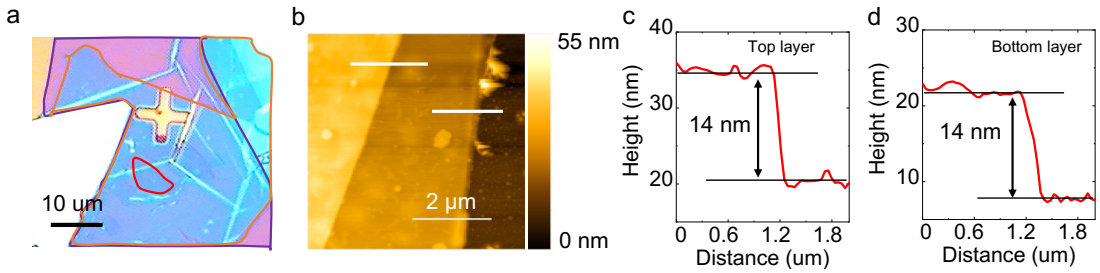

Figure 4.1. (a) Optical image of encapsulated 1L-$MoSe_2$ in *h*-BN[102]. (b) AFM image of top and bottom layer of *h*-BN. (c) and (d) show height profile and thickness of top and bottom layer of *h*-BN, respectively. Figures in this chapter are taken from Ref.[102], which I automatically have the copyright to use as one of authors.

Figure 4.2a shows the polarization-resolved PL spectra of *h*-BN encapsulated 1L-$MoSe_2$ at 20 K with σ^+ circularly polarized excitation under magnetic field from −7 to 7 T. At 0 T, the PL spectrum with σ^+ and σ^- components are almost identical with well-separated emissions. The peaks at 1.651 and 1.621 eV are assigned to exciton (X, blue) and trion (T, red) PL signals, respectively. The well-separated exciton and trion peaks suggest high quality of sample, allowing to investigate the valley physics for these excitonic states at low temperature[103]. The PL spectra are fitted by the Voight function.

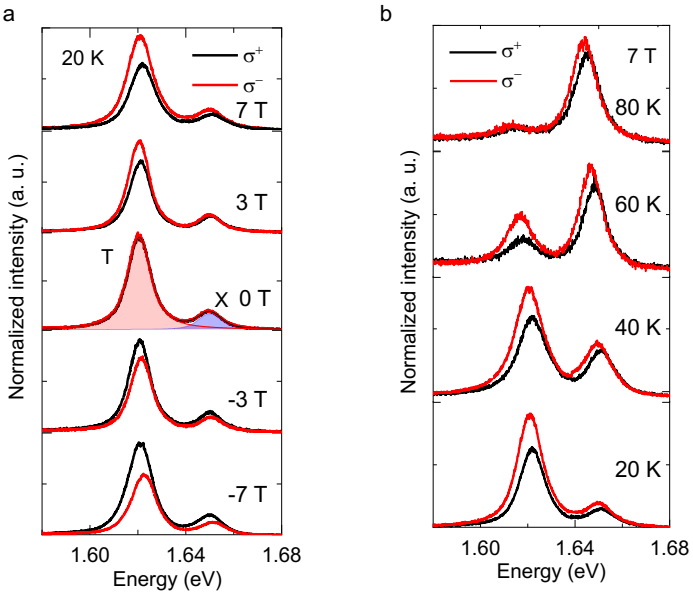

Figure 4.2. (a) Polarization-resolved PL spectra of *h*-BN encapusulated1L-$MoSe_2$ at 20 K with different magnetic fields from −7 and 7 T. (b) Polarization-resolved PL spectra of 1L-$MoSe_2$ at different temperatures under 7 T.

The fitting curves well agree with the PL spectra; therefore, the information of peak intensity and energy position could be obtained accurately. The PL spectra with σ^+ and σ^- components have the same peak energy and intensity at 0 T. As we know, the PL intensities of σ^+ and σ^- correspond to population of X or T at K+ and K– valleys, respectively, showing no valley polarization of trions and excitons without magnetic field, as previous report[104]. When magnetic field was applied, it shows the clear difference between PL spectra with σ^+ and σ^- component. The energy positions $E^{\sigma^+}_{X(T)}$ of X (T) in the σ^+ spectra shift to a higher energy side, while those of $E^{\sigma^-}_{X(T)}$ in the σ^- component shift to an opposite energy side with magnetic field increasing from 0 to 7 T. The energy positions $E^{\sigma^+}_{X(T)}$ and $E^{\sigma^-}_{X(T)}$ shift to the opposite side under negative magnetic field from 0 to -7 T. The valley Zeeman splitting of X (T) are defined as the difference between $E^{\sigma^+}_{X(T)}$ and $E^{\sigma^-}_{X(T)}$ at different magnetic field. Moreover, the valley polarization can be indicated by the difference in the PL intensity of X (T) in σ^+ and σ^- component.

In **Figure 4.2b**, the polarization-resolved PL spectra of 1L-$MoSe_2$ at various temperatures (20, 40, 60, and 80 K) under 7 T are shown. The intensity ratio component of trion and exciton (I_T/I_X) quickly drops with temperature elevated from 20 to 80 K caused by the dissociation of trion with absorbing phonons to exciton and free charge[105]. At 80 K, one can still clearly see the PL intensity difference of both trion and exciton at σ^+ and σ^- components, which suggests the stable valley polarization under magnetic field even at relatively high temperature.

4.3. Magnetic field dependent valley polarization

The $\Delta E_{T(X)}$ is difference between $E^{\sigma^+}_{T(X)}$ and $E^{\sigma^-}_{T(X)}$ which corresponds to the valley Zeeman splitting of the trion (exciton). The value of valley Zeeman splitting shows linear increase with magnetic field increasing from -7 to 7 T, as shown in black line in **Figure 4.3a, b**. The linear coefficient (slope of the black line) of both trion and exciton

is 0.21 ± 0.02 meV/T[104]. **Figure 4.3c, d** indicate the valley polarization of trion (ρ_T) and exciton (ρ_X) at 20 K, respectively, which was evaluated from the PL spectra with magnetic field from -7 to 7 T. No valley polarizations of trion (exciton) in 1L-$MoSe_2$ are observed without magnetic field (B = 0 T). The valley polarizations of trion and exciton gradually increase with applying the positive magnetic field (B > 0 T), while decreases with applying the negative magnetic field (B < 0 T). The trion (**Figure 4.3e**) and exciton (**Figure 4.3f**) valley polarization at -7 T decrease from 10 to 80 K. The valley polarization under magnetic fields is characteristic feature in valley physics of 1L-$MoSe_2$, which will be discussed in next subsections.

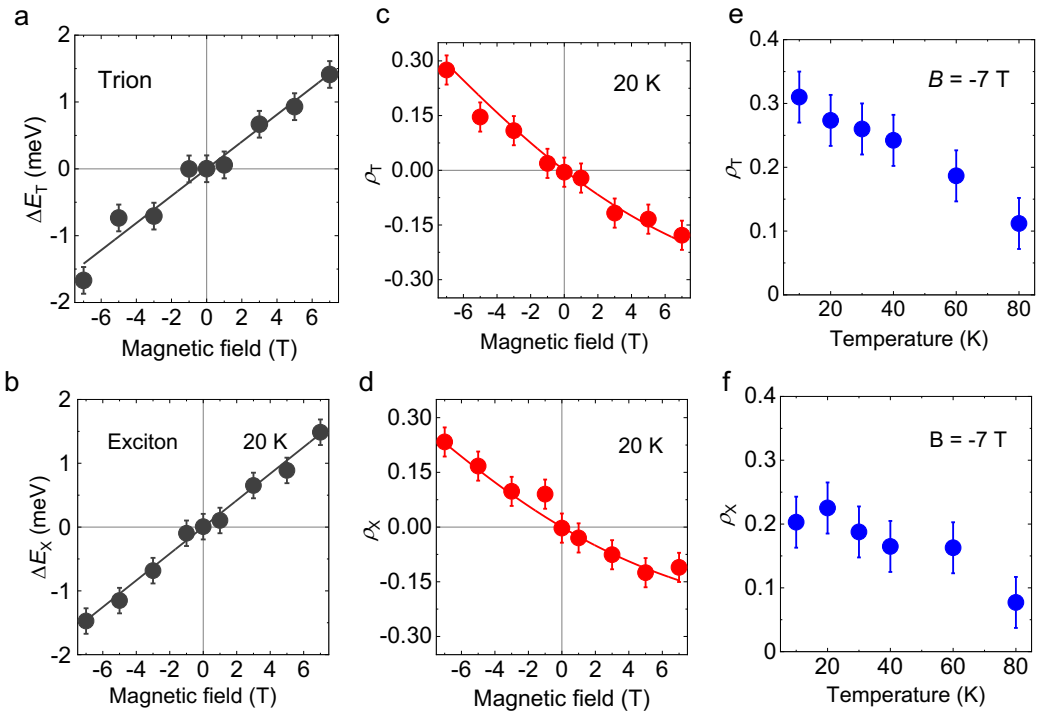

Figure 4.3. Valley Zeeman splitting as a function of magnetic field of trion (a) and exciton (b). Valley polarization ρ_T for trion (c) and (d) at 20 K. Valley polarization of trion (e) and (f) from 10 to 80 K at -7 T. Both black solid lines in (a) and (b) are linear fitting line with slope of 0.21 ± 0.02 meV/T. Red curve in (c) is fitted by Eq. (4.8). Red curve in (d) is fitted by **Eq. (4.13)**.

4.4. PL decay under magnetic field

The valley polarization $\rho_{T(X)}$ for trion (exciton) in the time-integrated

measurement is phenomenologically expressed as,

$$\rho_{\mathrm{T(X)}} = \frac{\rho_0}{1+\frac{\langle\tau_{\mathrm{T(X)}}\rangle}{\tau_v^{\mathrm{T(X)}}}}, \tag{4.1}$$

where ρ_0 is the initial valley polarization, $\langle\tau_{\mathrm{T}}\rangle(\langle\tau_{\mathrm{X}}\rangle)$ is the mean trion (exciton) lifetime, and ${\tau_v}^{\mathrm{T}}$ (${\tau_v}^{\mathrm{X}}$) is the valley relaxation time of trion (exciton) between K+ and K– valley. The trion (exciton) dynamics determined by the mean lifetime, and valley relaxation time of trion (exciton) dominates the degree of valley polarization. To understand the magnetic field dependent valley polarization, the PL decay of trion and exciton were measured using TCSPC method, which was explained in **Chapter 3**.

4.4.1. Lifetime of trion

The PL peak of trion is dominant here, therefore I will discuss trion first. The trion PL decay curves of σ^+ and σ^- components were measured by TCSPC method at 20 K under magnetic field of 7 T, as shown in **Figure 4.4a**. The instrumental response function (IRF) is plotted in **Figure 4.4a** as well. The decay curve of σ^+ and σ^- components corresponding to K+ and K– valleys are identical even under strong magnetic field. The experimentally obtained PL decay curves are fitted according to the convolution procedure with IRF and double-exponential function, $I = A_1 \exp(-t/\tau_1) + A_2 \exp(-t/\tau_2)$[103,106]. These fitted results are consistent with the experimental decay curves of trions. The mean trion lifetime is defined as $\langle\tau_{\mathrm{T}}\rangle = (A_1\tau_1 + A_2\tau_2)/(A_1 + A_2)$. The mean trion lifetimes for σ^+ and σ^- components are experimentally obtained as 67 ± 6 and 65 ± 6 ps, respectively. We can again confirm the almost no differences of trion PL decay between σ^+ and σ^- components (K+ and K– valleys) under the magnetic field.

Figure 4.4b shows the PL decay curves of the σ^+ component of the trion peak at 0 and 7 T at 20 K. The PL decay curves show the same profiles shape independent on magnetic field. **Figure 4.4c** displays the mean lifetimes of trion with increasing magnetic field. The mean lifetimes of trion reveal the constant values from 0 to 7 T taking the error bar into consideration. **Figure 4.4d** shows PL decay of trion measured

at 20, 40, and 60 K. The PL decay of trion tends to be shorter because of more efficient dissociation of trion with higher temperature[107]. The temperature-dependent mean trion lifetimes were evaluated by the same convolution procedure in **Figure 4.4e**, which indicates the decreases with elevating temperature.

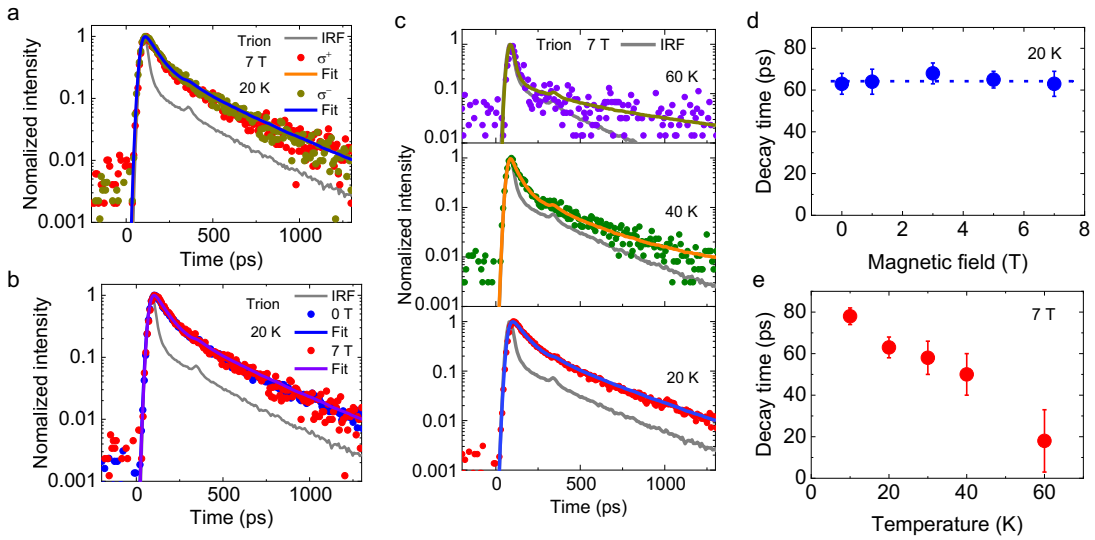

Figure 4.4. (a) Trion PL decay curves with σ^+ and σ^- components at 20 K with magnetic field of 7 T. (b) PL decay curves of trion under 0 and 7 T at 20 K. (c) Trion mean lifetime as a function of magnetic field at 20 K. (d) Trion PL decay curves at 20, 40, and 60 K under 7 T. (e) Temperature dependence of trion mean lifetime at varying temperatures under 7 T.

4.4.2. Lifetime of exciton

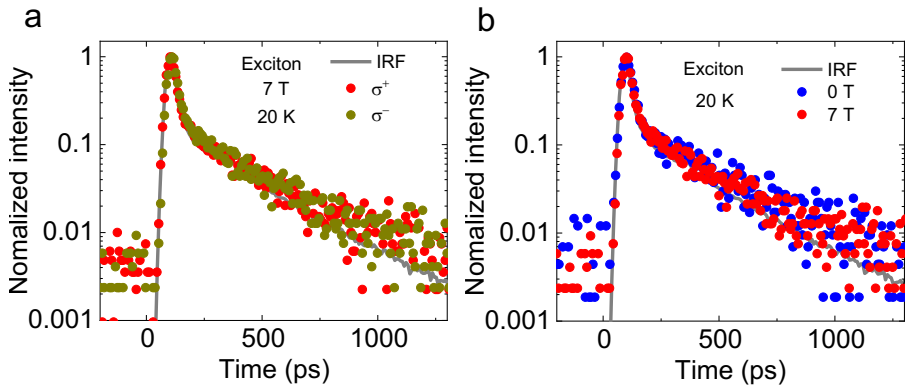

Figure 4.5. (a) PL decay of excitons with σ^+ and σ^- components under 7 T at 20 K. (b) PL decay of excitons with σ^+ component under 0 and 7 T at 20 K.

As similar to the case of trion, the decay curves of exciton of σ^+ and σ^- components

are identical even under strong magnetic field, as shown in **Figure 4.5a**. Moreover, the PL decay curves of exciton also shows no differences between 0 and 7 T (**Figure 4.5b**).

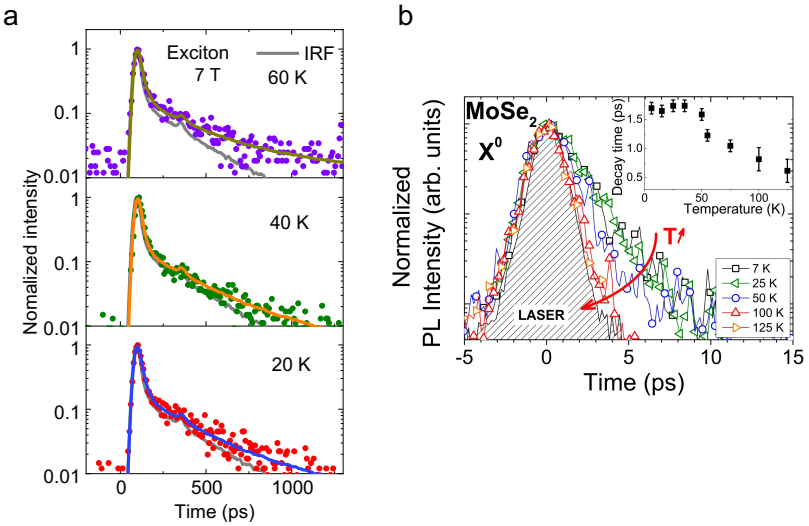

Figure 4.6. (a) PL decay of excitons at 20, 40, and 60 K under 7 T with IRF. (b) Temperature dependence of the exciton PL dynamics [108] © 2016 APS.

Figure 4.6a shows the temperature dependence of PL decays of excitons. The PL decay curves are close to IRF because of the limited time resolution of TCSPC method. These results are consistent with the reported short lifetimes of excitons with less than 10 ps[109]. The mean exciton lifetime at 10, 10, 20, 30, 40, 60, and 80 K are 1.7, 1.6, 1.8, 1.8, 1.2, and 1.0 ps **Figure 4.6b**[108].

4.5. Valley polarization dynamics under magnetic field

4.5.1. Schematic of energy diagram

Valley polarization dynamics of both trion and exciton in 1L-$MoSe_2$ under the magnetic field are revealed based on a phenomenological relaxation model combined with the rate equation. I use the four-energy level in this model, which include ground state, exciton, and trion levels at K+ and K– valleys, as displayed in **Figure 4.7**[110]. In the **Figure 4.7**, $G_{K+(K-)}$ ($g_{K+(K-)}$) is the trion (exciton) generation rate from the initial state by optical excitation. I assumed that the initial generation of a valley-polarized trion is formed from a valley-polarized exciton (ρ_X)[107] at low excitation power

condition due to the trion formation process from the exciton. No initial valley polarization of exciton is created by the circularly polarized light because the excitation photon energy is far above the exciton resonance more than 300 meV. Γ_{K+} (Γ_{K-}) is the inter-valley scattering rate of trion from K+ (K–) to K– (K+) valley, and Γ is the trion relaxation rate. $\gamma_{K+(K-)}$ is the valley scattering rate between K+ and K– valley, and γ is the exciton relaxation rate.

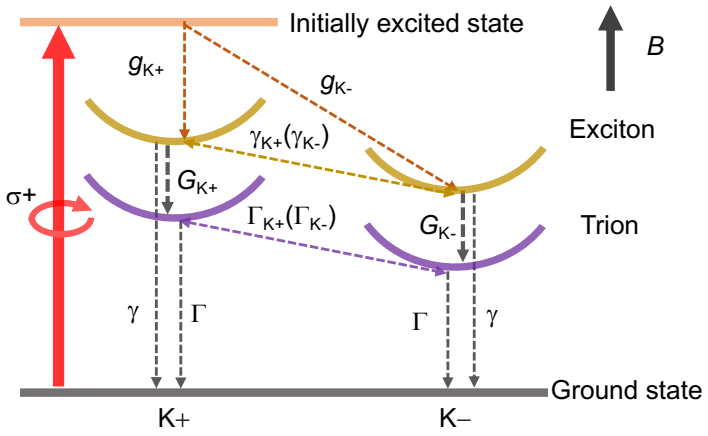

Figure 4.7. Schematic of energy diagram for intra- and inter-valley scattering dynamics of exciton and trion at K+ and K– valleys in 1L-$MoSe_2$.

4.5.2. Valley polarization dynamics of trion

According to the schematic diagram above, the temporal evolutions of trion population at K+ and K– valleys are described as

$$\frac{dN_{K+}}{dt} = G_{K+} + \Gamma_{K-}N_{K-} - \Gamma_{K+}N_{K+} - \Gamma N_{K+}, \tag{4.2}$$

$$\frac{dN_{K-}}{dt} = G_{K-} + \Gamma_{K+}N_{K+} - \Gamma_{K-}N_{K-} - \Gamma N_{K-}, \tag{4.3}$$

where $G_{K+(K-)}$ is the trion generation rate from the exciton state, the other parameters have been discussed in previous section. Since the initial generation of valley-polarized trion is created by the valley-polarized exciton, and inter-valley scattering of trion between K+ and K– is asymmetric ($\Gamma_{K+} \neq \Gamma_{K-}$), the trion populations of N_{K+} (N_{K-}) at K+ (K–) valley under steady-state conditions are by solved using **Eqs.** (**4.2**) and (**4.3**) as follows:

$$\rho_{\mathrm{T}} = \frac{N_{\mathrm{K+}} - N_{\mathrm{K-}}}{N_{\mathrm{K+}} + N_{\mathrm{K-}}} = \frac{\rho_{\mathrm{X}} - (1/\Gamma)(\Gamma_{\mathrm{K+}} - \Gamma_{\mathrm{K-}})}{1 + (1/\Gamma)(\Gamma_{\mathrm{K+}} + \Gamma_{\mathrm{K-}})}, \tag{4.4}$$

where $\rho_{\mathrm{X}} = (G_{\mathrm{K+}} - G_{\mathrm{K-}})/(G_{\mathrm{K+}} + G_{\mathrm{K-}})$ is the valley polarization of exciton. The energy degeneracy of K+ and K– valley could be lifted under magnetic field caused by valley Zeeman effect. Experimentally, I can observe the energy upshift and down shift of trion and exciton. The energy difference of trion emissions ΔE_{T} corresponds to valley Zeeman splitting because the valley scattering between K+ and K– valley is asymmetric as shown in **Figure 4.7**, which means $\Gamma_{\mathrm{K+}} \neq \Gamma_{\mathrm{K-}}$. The energy- upshift trion states have to overcome the energy barrier ΔE_{T} in inter-valley scattering process. Thus, I phenomenologically introduced asymmetric inter-valley scattering rates as following:

$$\Gamma_{\mathrm{low}} = \Gamma_0 \langle n_{\mathrm{ph}} \rangle, \tag{4.5}$$

$$\Gamma_{\mathrm{high}} = \Gamma_0 \big(\langle n_{\mathrm{ph}} \rangle + 1 \big), \tag{4.6}$$

here, Γ_{low} is the scattering rate from low to high energy valley, while Γ_{high} represents the scattering rate from high to low energy valley; $\langle n_{\mathrm{ph}} \rangle = 1/(\exp(\Delta E_{\mathrm{T}}/k_{\mathrm{B}}T) - 1)$ describes the phonon occupation number; ΔE_{T} is the valley Zeeman splitting of trion; k_{B} is Boltzmann constant, and T is temperature. As a result, I can obtain the relationship of the Γ_{low} and Γ_{high} as below:

$$\frac{\Gamma_{\mathrm{low}}}{\Gamma_{\mathrm{high}}} = e^{-\frac{\Delta E_{\mathrm{T}}}{k_{\mathrm{B}}T}}. \tag{4.7}$$

The trions at K+ and K– valley are located at the upshift and downshift energy level, respectively, as shown in **Figure 4.7** and vice versa. In the **Figure 4.7**, $\Gamma_{\mathrm{K+}}$ (Γ_{high}) equals Γ_0, and $\Gamma_{\mathrm{K-}}$ (Γ_{low}) equals $\Gamma_0 \exp(-\frac{\Delta E_{\mathrm{T}}}{k_{\mathrm{B}}T})$ at positive magnetic field ($B > 0$), where Γ_0 is the valley scattering rate without magnetic field. As above discussion, we can finally modify **Eq. (4.7)** as follows:

$$\rho_{\mathrm{T}}(B,T) = \frac{\rho_{\mathrm{X}} - (\Gamma_0/\Gamma)(1 - \exp(-\Delta E_{\mathrm{T}}(B)/k_{\mathrm{B}}T))}{1 + (\Gamma_0/\Gamma)(1 + \exp(-\Delta E_{\mathrm{T}}(B)/k_{\mathrm{B}}T))}, \tag{4.8}$$

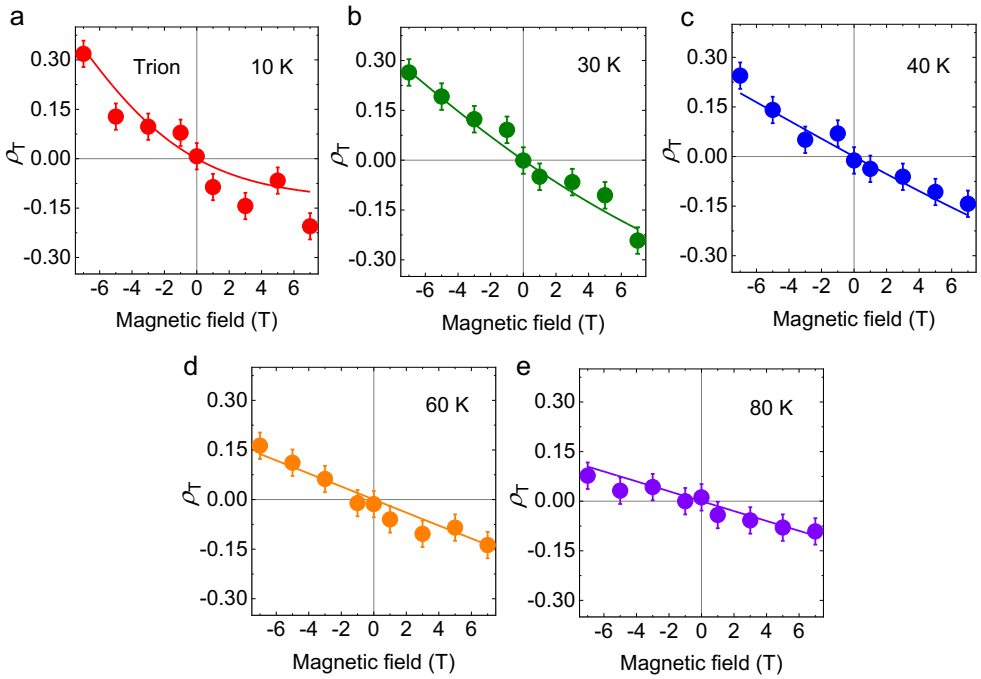

Figure 4.8. Valley polarization of trions as a function of magnetic field at 10 K (a), 30 K (b), 40 K (c), 60 K (d), and 80 K (e). The solid lines are fitted curves using **Eq. (4.8)**.

The magnetic field dependence of trion valley polarization at 20 K in **Figure 4.3c** is well-reproduced using **Eq. (4.8)**. The fitting parameters of Γ_0/Γ is (0.17 ± 0.03). Since Γ equals (64 ± 6 ps)$^{-1}$, calculated from decay time of trions in the Section 4.3.1, Γ_0 is finally obtained by the value of (376 ± 36 ps)$^{-1}$. Moreover, the magnetic field dependent-valley polarizations of trions at 10, 30, 40, and 60 K are well-fitted as well, as shown in **Figure 4.8**. At lowest temperature of 10 K in our experiment, Γ at zero magnetic field is evaluated as 650 ± 36 ps.

Figure 4.9 indicates trion inter-valley scattering time of $(\Gamma_{K+})^{-1}$ from K+ to K– valley and $(\Gamma_{K-})^{-1}$ from K– to K+ valley as a function of the magnetic field from 0 to 7 T. The inter-valley scattering time of trions from K– to K+ valley increases with increasing magnetic field, because the barrier energy (ΔE_T) from K– to K+ increases from 0 to 7 T, as discussed above. In addition, the difference of $(\Gamma_{K+})^{-1}$ and $(\Gamma_{K-})^{-1}$ significantly increases with increasing magnetic field due to the symmetry breaking of K+ and K– valleys. The inter-valley scattering time of trions from K– to K+ valley at 7 T at 10 K reaches to ~4 ns.

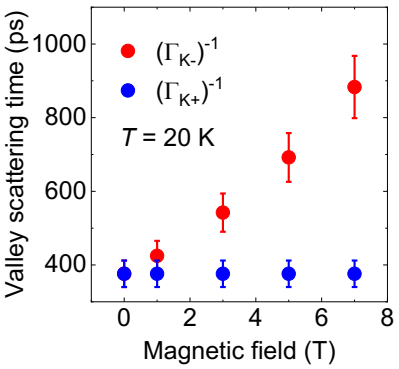

Figure 4.9. Inter-valley scattering time of trions as a function of magnetic field at 20 K.

Figure 4.10 shows the calculated temperature dependent valley scattering time of trions $(\Gamma_{K-})^{-1}$ at different magnetic field. The long trion valley scattering time from K– to K+ (~400 ps) at 0 T quickly reduces from 10 to 60 K. Besides, it has been observed similarly under high magnetic field also at 3 and 7 T in **Figure 4.10**. This is caused by temperature-dependence of phonon-mediated inter-valley scattering[111]. The solid curves are calculated using the following equation[111]:

$$\Gamma_{K-}(B,T) = \tau_0^{-1}(B) + \frac{\tau^{-1}}{\exp\left(\frac{E_{ph}}{k_B T}\right)-1}, \quad (4.9)$$

where $\tau_0(B)$ is the inter-valley scattering rate at 0 K; τ is the phonon-mediated inter-valley scattering rate of trions; and E_{ph} is the phonon energy. The calculated lines well reproduced the experimental data at typical magnetic field of 0, 3, and 7 T, using E_{ph} = ~18.5 meV, τ = ~0.1 ps, and τ_0 = ~550 ps, ~1 ns, ~4 ns, respectively. The estimated value of E_{ph} is consistent with the energy of the longitudinal acoustic (LA) mode (~19 meV). LA phonon plays a critical role in the inter-valley scattering of 1L-$MoSe_2$[112,113]. These results successfully explained why inter-valley scattering rate decreases with increasing temperature.

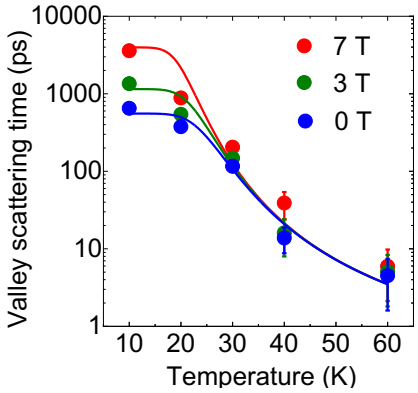

Figure 4.10. Inter-valley scattering time of trions from K– to K+ valley as a function of temperature at 0, 3 and 7 T. The solid lines are fitted by **Eq. (4.9)**.

4.5.3. Valley polarization dynamics of excitons

In this section, the valley polarization of exciton ρ_X under magnetic fields will be discussed similar with that of trions. The experimental result of ρ_X in the time-integrated measurement was described in the section 4.3. As different from the trion forming from excitons, ρ_0 of excitons is initial valley polarization, is created by the circularly polarized light. However, ρ_0 equals zero, because the excitation photon energy is more than 300 meV above the exciton resonance.

According to the energy level as shown in **Figure 4.7** in the **Section 4.4.1**, the temporal evolutions of exciton populations of K+ and K– valleys can be expressed as

$$\frac{dn_{K+}}{dt} = g_{K+} + \gamma_{K-} n_{K-} - \gamma_{K+} n_{K+} - \gamma n_{K+}, \quad (4.10)$$

$$\frac{dn_{K-}}{dt} = g_{K-} + \gamma_{K+} n_{K+} - \gamma_{K-} n_{K-} - \gamma n_{K-}, \quad (4.11)$$

where $n_{K+(K-)}$ is the exciton population at K+ (K–) valley; $g_{K+(K-)}$ is the excited state of exciton generation rate; $\gamma_{K+(K-)}$ is the exciton valley scattering rate of two valley; and $\gamma_= \langle \tau_X \rangle^{-1}$ is relaxation rate of excitons. The exciton populations of $n_{K+(K-)}$ at K+ (K–) valley are derived using **Eqs. (4.10)** and **(4.11)** under steady-state conditions. The valley polarization of excitons is the difference of exciton populations between K+

and K– valleys normalized by the total exciton population as follows:

$$\rho_X = \frac{n_{K+}-n_{K-}}{n_{K+}+n_{K-}} = \frac{\rho_0-(1/\gamma)(\gamma_{K+}-\gamma_{K-})}{1+(1/\gamma)(\gamma_{K+}+\gamma_{K-})}, \quad (4.12)$$

as similar to that of trions, asymmetric exciton scattering rate was assumed as $\gamma_{K-} = \gamma_0 \exp\left(-\frac{\Delta E_X}{k_B T}\right)$ and $\gamma_{K+} = \gamma_0$ at positive magnetic field, where γ_0 is the valley scattering rate at 0 T, and k_B is the Boltzmann constant. The valley polarization of excitons under magnetic field is finally expressed as below:

$$\rho_X(B,T) = \frac{\rho_0-(\gamma_0/\gamma)(1-\exp(-\Delta E_X(B)/k_B T))}{1+(\gamma_0/\gamma)(1+\exp(-\Delta E_X(B)/k_B T))}. \quad (4.13)$$

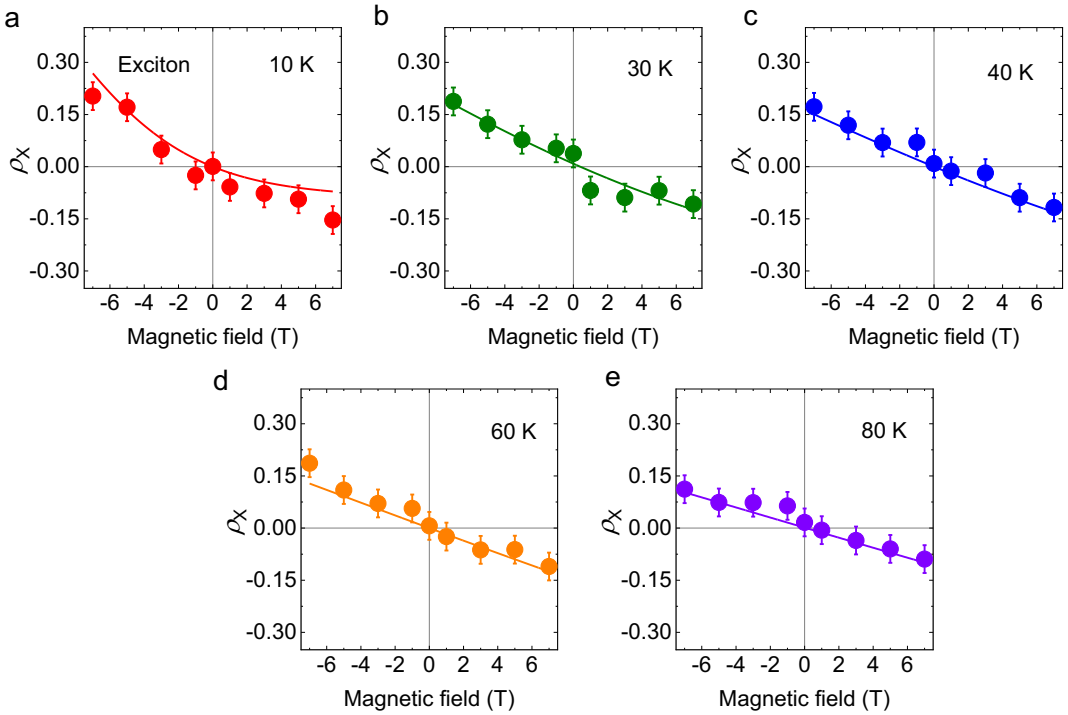

Figure 4.11. Valley polarization of excitons as a function of magnetic field at 10 K (a), 30 K (b), 40 K (c), 60 K (d), and 80 K (e). The solid lines are fitted curves using **Eq. (4.13)**.

The experimental results of magnetic field-dependent valley polarization of excitons at 10, 30, 40, 60, and 80 K are shown in **Figure 4.11,** corresponding to the calculated results $1/\gamma$ of 1.7, 1.8, 1.8, 1.2, and1.0 ps [108] (**Figure 4.6b**), respectively, using **Eq. (4.13)** and ρ_0 = ~ 0. The fitting of magnetic field-dependent valley polarization of excitons at 20 K are exhibited in **Figure 4.3** with $1/\gamma$ of 1.6 ps[108].

These results reproduced the experimental results well, as shown in **Figure 4.11 and 4.3**.

Figure 4.12 shows the obtained exciton valley scattering time at 20 K and its temperature dependence at different magnetic field. The difference between valley scattering time increases with magnetic field, leading to the larger and larger valley polarization, which is similar as the behavior of trions. The decrease of valley scattering time with elevated temperature, is consistent with the previous report[98], which strongly supports the validity of this analysis. Moreover, the inter-valley scattering time of trions at zero magnetic field is evaluated as 650 ± 36 ps at 10 K in previous section, which is much longer than that of excitons here of a few picoseconds. It also confirmed the initial generation of valley-polarized trions by the feeding of valley-polarized excitons, while the valley polarization of excitons is created by the circularly polarized light.

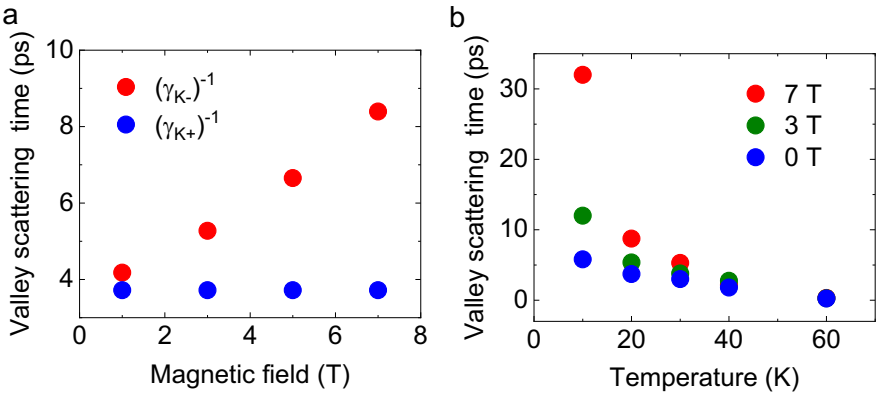

Figure 4.12. Exciton valley scattering time as a function of (a) magnetic field at 20 K and (b) temperature at different magnetic field.

4.6. Chapter summary

In this chapter, we studied the valley dynamics of excitonic states (excitons and trions) in 1L-$MoSe_2$ under magnetic field. I observed valley polarization of excitons and trions due to the external magnetic field. The rate equation combined with three-level model was used to analyze the experimental results. It is found that the magnetic field induced valley polarization of excitonic states gives a rise to the asymmetric valley scattering of emission states between K+ and K– valley because of the lifting of the

valley degeneracy of two valleys by valley Zeeman effect under external magnetic field. In addition, the feeding of valley-polarized excitons for forming tirons contributes to a longer inter-valley scattering time of trion, which reaches to a few nanoseconds than that of excitons of a few picoseconds at 10 K. This work exhibits novel physical insights for dynamics of excitonic valley polarization under magnetic field. These new insights for the dynamics of excitonic valley polarization show the guides toward keeping long-time and manipulating valley polarization, which is strongly required for future valleytronics applications.

Chapter 5. Control of magnetic proximity effects of 1L-$MoSe_2$ and double-layered perovskite manganese oxide van der Waals heterostructure

5.1. Introduction

The Coulomb interaction is enhanced in 1L-TMD, because of the strong confinement and reduced dielectric screening effect, as introduced in Chapter 2. Therefore, excitons and charged excitons (trions) have large binding energy[6,114–117]. The electric-field line between these charges extend outside the atomically thin materials, leading to the electronic structure of 1L-TMD is sensitive to the surroundings[43].

Moreover, the excitons and trions in 1L-TMD shows valley degrees of freedom, because the electrons and holes comprising the excitons and trions are located at the energy degenerate K+ and K− valleys, as discussed in **Chapter 4**. The optically generated excitons and trions are strongly dependent on the physical properties of substrate materials caused by the proximity effect[25,28,118]. The 1L-TMD on the insulating ferromagnetic substrates can be good platform to study exchange interactions between the valley spin-polarized excitonic states of 1L- TMD and ferromagnetic spins of ferromagnetic substrates via proximity magnetic-exchange effects. Using this approach, one can manipulate the valley spin polarization and large valley splitting of excitonic states. However, only ferromagnetic insulators have been used in 1L-TMD to lift the valley degeneracy. A large variety of other magnetic materials such as ferromagnetic metals is therefore not applied.

In this chapter, I will introduce a metallic ferromagnetic material of perovskite manganese oxide, which belongs to strongly correlated electron systems. The perovskite manganese oxide has been extensively studied as a model system for the

double-exchanged interactions of *d*-orbital electrons in Mn sites through O 2*p*-orbitals[119,120]. Moreover, it has exhibited intriguing several physical phenomena such as colossal magnetoresistance[121] and charge ordering[122]. The e_g electrons in this perovskite Mn oxide trigger the electronic and magnetic phase transition from the ferromagnetic metal (FM) to the paramagnetic insulator (PI) at Curie temperature (T_C) caused by double exchange interactions[119,123]. Therefore, the perovskite manganese oxide, which possesses electronic and magnetic phase transition, are ideal platforms for building artificial heterostructures together with semiconducting 1L-TMD.

Thus, I fabricate 1L-$MoSe_2$, few-layer *h*-BN, and double-layered perovskite (Ruddlesden-Popper structure)[120,124,125] Mn oxide ($(La_{0.8}Nd_{0.2})_{1.2}Sr_{1.8}Mn_2O_7$) to systematically study the interface interactions between the excitonic states (excitons and trions) and magnetic spins as well as charge carriers.

5.2. Schematic diagram of vdW heterostructure

Figure 5.1 shows the schematic diagram of the vdW heterostructure under applied magnetic field *B* in the out-of-plane direction. It is composed of the bottom layer of double-layered perovskite Mn oxide ($(La_{0.8}Nd_{0.2})_{1.2}Sr_{1.8}Mn_2O_7$) with T_C of 80 K, the interlayer of *h*-BN with different thicknesses *d* ranging from 0 to 8 nm, and the top layer of 1L-$MoSe_2$. The bottom of **Figure 5.1** shows the diagram of double-exchange interactions of *d*-electrons of the Mn sites[119,123,126]. The transferring integral of itinerant electrons in the e_g orbitals of Mn sites is strongly dependent on the alignment of localized t_{2g} electrons with magnetic moments. In addition, the alignment of localized t_{2g} electrons in ferromagnetic state makes the itinerant e_g electrons to hop through the crystal, inducing the FM to PI phase at T_C in Mn oxide[127].

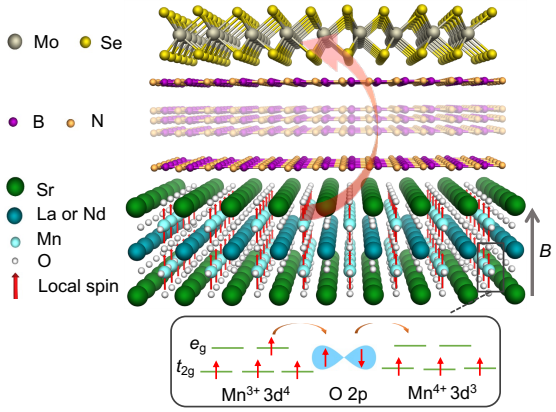

Figure 5.1. Schematic diagram of the vdW heterostructure consisting of the bottom layer of Mn oxide, the interlayer of *h*-BN with different thicknesses *d* ranging from 0 to 8 nm, and the top layer of 1L-$MoSe_2$. *B* is the external magnetic field which is applied in the out-of-plane direction. The bottom is the diagram of double-exchange interaction.

I measure the magnetic field and temperature dependent out-of-plane magnetization of Mn oxide (M_C) using a superconducting quantum interference device (SQUID) magnetometer to characterize. **Figure 5.2a** shows that Mn oxide has no coercive field at 10 K due to soft-magnetic properties. The M_C rapidly increases with magnetic field increasing to 1 T and saturates above 1 T. The measured M_C and its magnetic field dependence shows the similar results with previous report[123]. Moreover, T_C is therefore estimated to be around 80 K from the temperature dependence of M_C in **Figure 5.2b**.

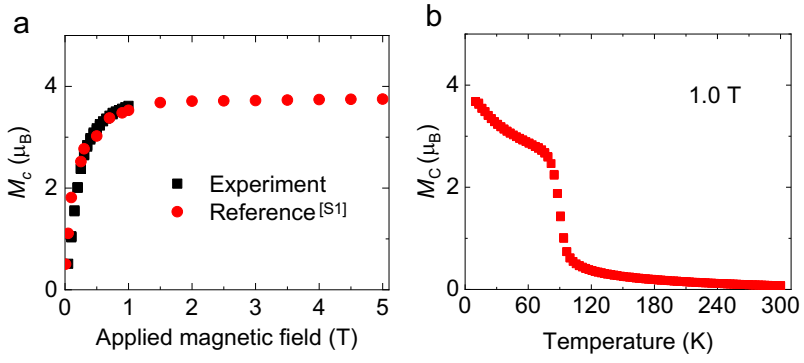

Figure 5.2. (a) Out-of-plane magnetization (M_C) of Mn oxide ($(La_{0.8}Nd_{0.2})_{1.2}Sr_{1.8}Mn_2O_7$) as a function of the applied magnetic field in this experiment (red) and the previously reported result (black) at 10 K[123]. (b) Temperature dependence of M_C from 10 to 300 K with an applied magnetic field of 1 T under zero-field cooling condition.

Figure 5.3a shows a typical optical microscope image of 1L-$MoSe_2$/*h*-BN/Mn oxide vdW heterostructure with an *h*-BN thickness (*d*) of 1.4 nm on a SiO_2/Si substrate, which is denoted as 1L-$MoSe_2$/*h*-BN/Mn oxide (*d* = 1.4 nm). The optical images of all vdW heterostructures used in chapter are shown in **Figure 5.4**. The 1L-$MoSe_2$, *h*-BN, and Mn oxide are indicated by red, yellow, and black broken curves, respectively. Moreover, the Mn oxide enables good contact with both thin-layered $MoSe_2$ and *h*-BN because the double-layered Mn oxide has an atomically flat surface morphology with a root-mean-square (RMS) roughness of only 0.2 nm, as shown in **Figure 5.3b**. This was confirmed by atomic force microscopy (AFM).

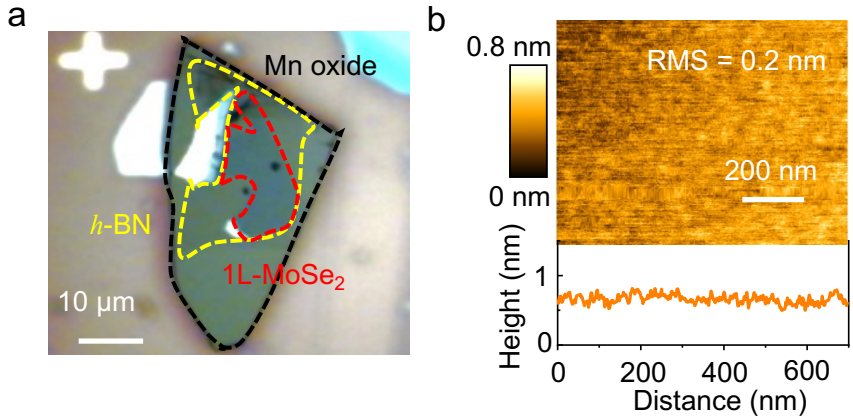

Figure 5.3. (a) Optical microscope image of the vdW heterostructure (1L-$MoSe_2$/*h*-BN/Mn oxide, *d* = 1.4 nm) with a scale bar of 10 μm. The red, yellow, and black broken curves show boundaries of $MoSe_2$, *h*-BN, and Mn oxide, respectively. (b) Surface roughness of Mn oxide measured by AFM. The scale bar is 200 nm. Figures in this chapter are taken from Ref.[128], which I automatically have the right to use as an author.

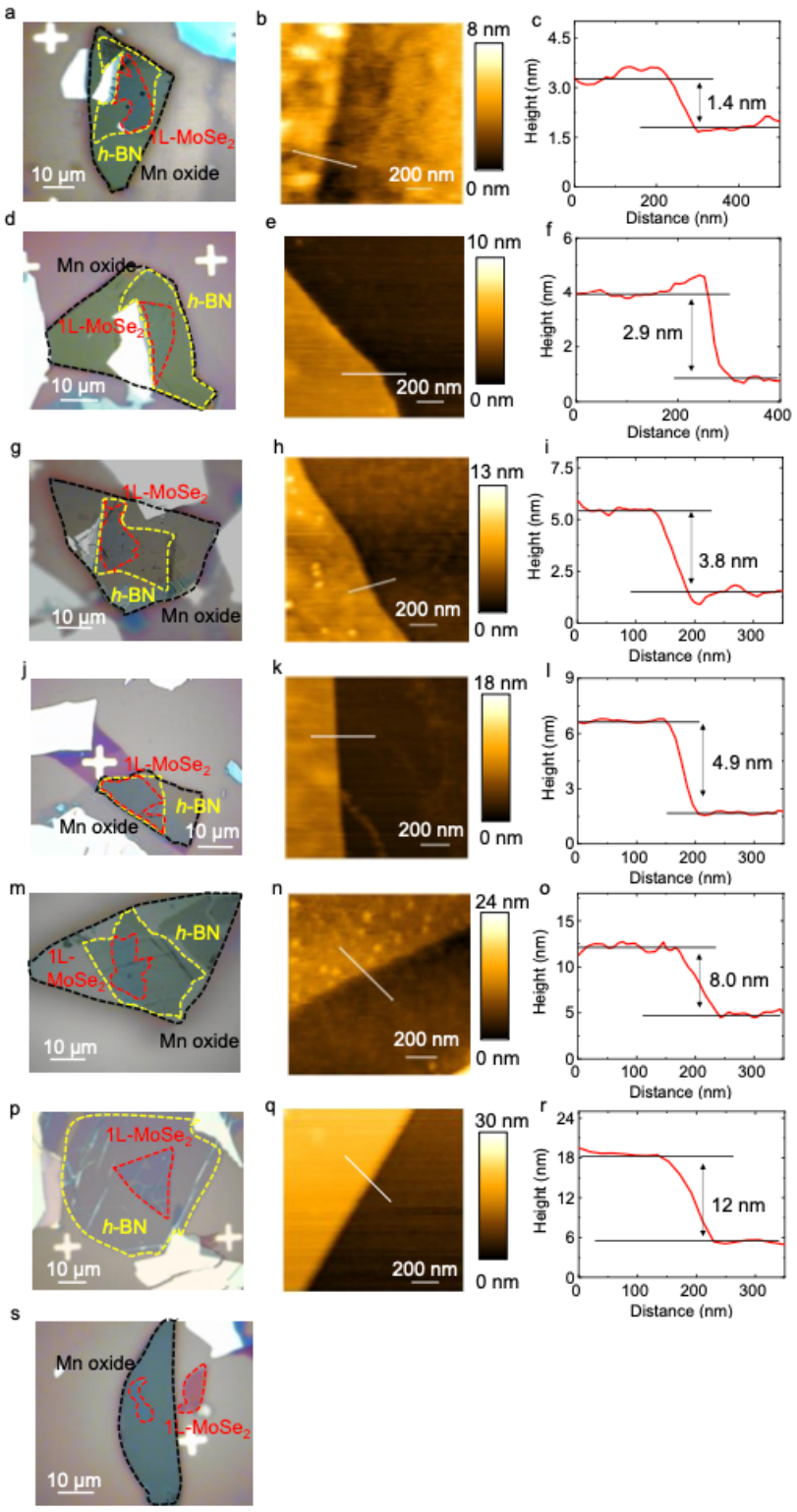

Figure 5.4. Optical and atomic force microscope images of vdW heterostructures. Optical microscope images of 1L-$MoSe_2$/*h*-BN/Mn oxide with different thicknesses of *h*-BN, shown in (a), (d), (g), (j), and (m), respectively. The red, yellow, and black dots correspond to 1L-$MoSe_2$, *h*-BN, and Mn oxide, respectively. AFM images at the edge

of *h*-BN on Mn oxide are shown in (b), (e), (h), (k), and (n), respectively. The thickness of *h*-BN is determined by height difference along the edge (white line), as shown in (c), (f), (i), (l), and (o) and the thicknesses of the respective heterostructures in (a), (d), (g), (j), and (m), are 1.4, 2.9, 3.8, 4.9 and 8.0 nm. (p) Optical microscope image of $MoSe_2$ on *h*-BN and (q) AFM image. (r) The thickness of *h*-BN is 12 nm. (s) Optical microscope image of both $MoSe_2$ on Mn oxide and on SiO_2/Si substrate.

5.3. Temperature dependent PL spectra in vdW structure

5.3.1. Results of temperature dependence of PL spectra

Figure 5.5a presents the contour maps of temperature-dependent PL spectra of a reference of 1L-$MoSe_2$/*h*-BN (left) and vdW heterostructure of 1L-$MoSe_2$/Mn oxide (right), respectively, with the temperature ranging from 10 to 300 K. The PL peaks of the neutral excitons (X) and trions (T) are clearly observed below 80 K[129–131] in both maps, while the PL intensities of trions drop significantly above 60 K with increasing temperature[105]. The PL peaks of excitons in both maps gradually shift to the lower energy side because of the shrinkage of the band gap of 1L-$MoSe_2$, due to thermal lattice expansions[132,133]. In contrast, the temperature dependence of exciton PL intensity (I_X) above T_C (80 K) shows a clear difference between the reference and the vdW heterostructure, where I_X of the reference decreases gradually, while that of the vdW heterostructure increases with increasing temperature. This clear difference in the PL behavior suggests that the excitonic properties are strongly affected by the metal-insulator phase transition of the Mn oxide substrate.

Figure 5.5b shows the PL spectra of the reference sample of $MoSe_2$/*h*-BN (left) and 1L-$MoSe_2$/Mn oxide (right) at 10 K. The PL spectra are fitted using multiple-Voigt functions which is composed of excitons (X, blue), trions (T, orange), and localized excitons from defect states (L, gray). Their peak energies, spectral integrated intensities, and homogeneous linewidths can be well obtained. The most striking difference between the two samples here is the larger spectral weight of trions in the vdW

heterostructure than that in the reference at 10 K, which will be discussed in detail in this section.

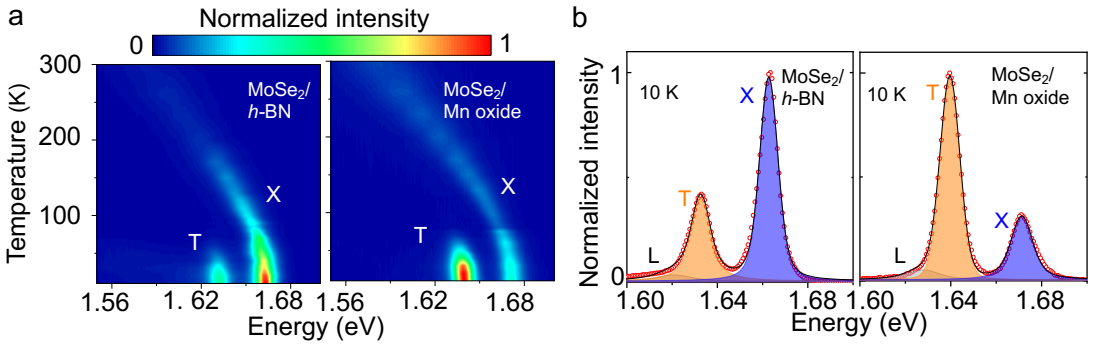

Figure 5.5. (a) Contour plots of the temperature-dependent PL spectra of the reference of $MoSe_2$/*h*-BN (left) and vdW heterostructure $MoSe_2$/Mn oxide (right) from 10 to 300 K. (b) PL spectra of $MoSe_2$/*h*-BN (left) and $MoSe_2$/Mn oxide (right) at 10 K.

Figure 5.6a and its inset show the temperature-dependent integrated PL intensity of excitons (I_X) and trions (I_T) of $MoSe_2$/Mn oxide and $MoSe_2$/*h*-BN, respectively. The normalized I_T of both the vdW heterostructure and reference decrease with elevated temperature. The temperature dependence of normalized I_X in the $MoSe_2$/*h*-BN monotonically decreases, which is consistent with the previously reported result[129]. In contrast, normalized I_X of the vdW heterostructure decreases firstly with increasing temperature from 10 K to the phase transition temperature T_C (80 K) of Mn oxide. This result is similar to that observed for $MoSe_2$/*h*-BN without Mn oxide substrate below 80 K, while it turns up and gradually increases above 80 K. The drastic change in the exciton PL signal across the phase transition temperature suggests that the exciton dynamics of $MoSe_2$ in vdW heterostructure is sensitively dependent on the metal-insulator transition of Mn oxide underneath.

The typical temperature dependence of exciton PL intensity of monolayer 2D semiconductors can be explained by stronger temperature dependence of the radiative decay rate of 2D excitons ($\gamma_X \propto 1/T$), which is in competition with weaker temperature dependent non-radiative decay rate[54,108,134,135]; this result agrees well with that of $MoSe_2$/*h*-BN. The temperature dependence of the radiative decay rate of excitons also can explain the experimental results of 1L-$MoSe_2$ on metallic Mn oxide below its phase

transition temperature (80 K). In contrast, the significant deviation from the temperature dependence of the exciton radiative decay rate above 80 K in the vdW heterostructure is reflected by the change in the dielectric screening of excitons in the range of its binding energy (a few hundreds of meV) across the metal-insulator transition[136]. The dielectric functions of Mn oxide in the energy range of a few hundreds of meV tend to sensitively change depending on the elevating temperature, due to the opening of the charge transfer gap (energy gap) toward the metal-insulator transition[120] from lower to higher temperature above T_C. The reduced screening of excitons on Mn oxide would increase its radiative decay rate with increasing temperature, which enhances the exciton PL intensity of the vdW heterostructure. This scenario explains the increasing exciton PL intensity toward higher temperatures and suggests that the exciton dynamics of 1L-$MoSe_2$ are strongly affected by the phase transition of Mn oxide.

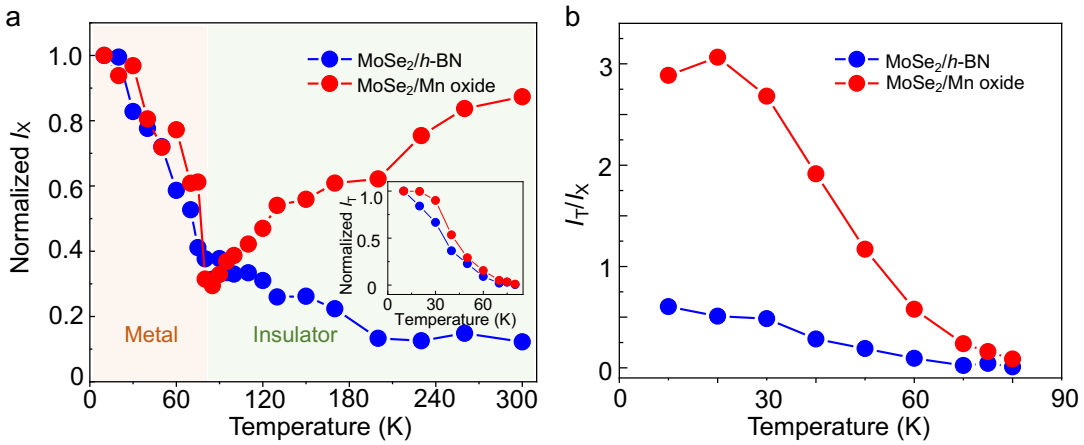

Figure 5.6. (a) Exciton PL intensity (I_X) of the $MoSe_2$/*h*-BN and $MoSe_2$/Mn oxide as a function of temperature. Both curves are normalized by the intensity at 10 K. Inset shows the normalized trion PL intensity (I_T) from 10 to 80 K. (b) PL intensity ratio of trions and excitons (I_T/I_X) from 10 to 80 K.

Figure 5.6b shows the integrated PL intensity ratio of the trion and exciton components (I_T/I_X) as a function of temperature below T_C (80 K) of Mn oxide. I_T/I_X in the vdW heterostructure is significantly larger than that in the reference, when the Mn oxide is in the metallic state below 80 K, which suggests higher doped carrier density of $MoSe_2$ on Mn oxide than that of the reference $MoSe_2$/*h*-BN[137].

5.3.2. Characteristic charge transfer effect in vdW heterostructure

To have a deeper understanding of the above experimental results, I derive the relationship between the PL intensity ratio of the exciton and trion (I_T/I_X) and the doped carrier density of $MoSe_2$ (n_e). Based on the rate equation analysis within the framework of the three-level model including the exciton (X), trion (T), and ground state (G) as shown is **Figure 5.7**.

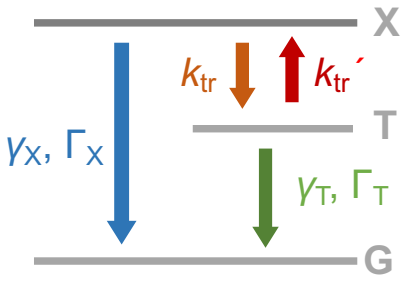

Figure 5.7. The exciton and trion dynamics within a three-level model consisting of the exciton (X), trion (T), and ground state (G).

The time evolution of populations of excitons (N_X) and trions (N_T) in the three-level model can be described as follows[138]:

$$\frac{dN_X}{dt} = G - \gamma_X N_X - \Gamma_X N_X - k_{tr} N_X + k'_{tr} N_T, \tag{5.1}$$

$$\frac{dN_T}{dt} = -\gamma_T N_T - \Gamma_T N_T + k_{tr} N_X - k'_{tr} N_T, \tag{5.2}$$

where G is the exciton generation rate, $\gamma_{X(T)}$ and $\Gamma_{X(T)}$ are the radiative and nonradiative relaxation rate of the exciton (trion), and k_{tr} (k_{tr}') is the formation rate of the trion from the exciton (dissociation rate of trion). The numbers of excitons and trions derived from the steady-state solutions of these equations are expressed as:

$$N_X = \frac{G\cdot(\gamma_T+\Gamma_T+k'_{tr})}{(\gamma_X+\Gamma_X+k_{tr})(\gamma_T+\Gamma_T+k'_{tr})-k'_{tr}k_{tr}}, \tag{5.3}$$

$$N_T = \frac{G\cdot k_{tr}}{(\gamma_X+\Gamma_X+k_{tr})(\gamma_T+\Gamma_T+k'_{tr})-k'_{tr}k_{tr}}. \tag{5.4}$$

Assuming a single phonon absorbed and emitted, the formation and dissociation rates between the exciton and trion states are described as $k_{tr} = k_0 n_e(1 + \langle n_{ph}\rangle)$, and

$k_{\mathrm{tr}}^{'} = k_0 n_{\mathrm{e}} \langle n_{\mathrm{ph}} \rangle$, respectively, where n_{e} is the doped carrier density, k_0 is the transition rate between the exciton and trion at low carrier density limit[138–141]. $\langle n_{\mathrm{ph}} \rangle = 1/\{\exp(\Delta E/k_{\mathrm{B}}T) - 1\}$ is the phonon occupation number, where ΔE is the splitting of exciton and trion state. The PL intensity of the exciton (I_{X}) and trion (I_{T}) can be expressed by the relationship where the PL intensity is proportional to the number of excitons (trions):

$$I_{\mathrm{X}} = A\gamma_{\mathrm{X}} N_{\mathrm{X}}, \tag{5.5}$$

$$I_{\mathrm{T}} = A\gamma_{\mathrm{T}} N_{\mathrm{T}}, \tag{5.6}$$

where A is the collection efficiency of PL intensity. Consequently, the PL intensity ratio $I_{\mathrm{T}}/I_{\mathrm{X}}$ can be described as

$$\frac{I_{\mathrm{T}}}{I_{\mathrm{X}}} = \frac{\gamma_{\mathrm{T}}}{\gamma_{\mathrm{X}}} \cdot \frac{k_{\mathrm{tr}}}{(\gamma_{\mathrm{T}}+\Gamma_{\mathrm{T}}+k_{\mathrm{tr}}^{'})} = \frac{\gamma_{\mathrm{T}}}{\gamma_{\mathrm{X}}} \cdot \frac{\exp\left(\frac{\Delta E}{k_{\mathrm{B}}T}\right)}{\frac{\gamma_{\mathrm{T}}+\Gamma_{\mathrm{T}}}{k_0 n_{\mathrm{e}}}\left\{\exp\left(\frac{\Delta E}{k_{\mathrm{B}}T}\right)-1\right\}+1}. \tag{5.7}$$

At low temperature ($k_{\mathrm{B}}T << \Delta E$) and low carrier density region, the radiative decay rates of excitons and trions are constant.[134] Under these conditions, **Eq. (5.7)** can be described as $\frac{I_{\mathrm{T}}}{I_{\mathrm{X}}} \approx \left(\frac{\gamma_{\mathrm{T}}}{\gamma_{\mathrm{X}}}\right) \cdot \left(\frac{k_0}{\gamma_{\mathrm{T}}+\Gamma_{\mathrm{T}}}\right) \cdot n_{\mathrm{e}} \propto n_{\mathrm{e}}$, suggesting that the intensity ratio of trions and excitons $I_{\mathrm{T}}/I_{\mathrm{X}}$ is proportional to the doped carrier density n_{e}. From this relation, the higher intensity ratio of the vdW heterostructure compared with that of the reference (**Figure 5.6)** can be understood by the higher doped carrier density in the vdW heterostructure because of the charges transfer from metallic Mn oxide to 1L-$MoSe_2$.

5.4. Length scale of charge transfer

5.4.1. Temperature dependent PL spectra of heterostructure with different *h*-BN thickness

In this section, I investigate the length scales of the charge transfer in the vdW heterostructure of $MoSe_2$/*h*-BN/Mn oxide by changing the *h*-BN thickness, using the temperature dependent PL spectral measurements.

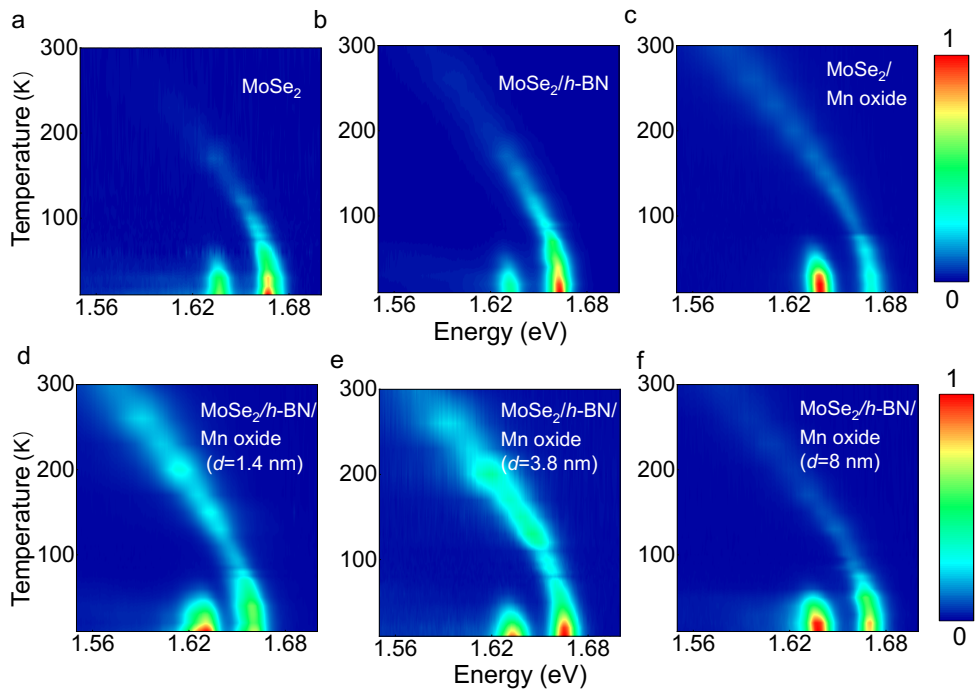

Figure 5.8. Temperature dependence of the PL spectra in vdW heterostructures with different *h*-BN thicknesses (*d*). Contour plot of the temperature-dependent PL spectra of 1L-$MoSe_2$ on SiO_2/Si (a), $MoSe_2$ on *h*-BN (b), 1L-$MoSe_2$/Mn oxide (c), 1L-$MoSe_2$/*h*-BN/Mn oxide (*d* =1.4 nm) (d), 1L-$MoSe_2$/*h*-BN/Mn oxide (*d* =3.8 nm) (e), and 1L-$MoSe_2$/*h*-BN/Mn oxide (*d*=8 nm) (f).

Figure 5.8 and 5.9 show contour plot and waterfall plot of temperature dependence of the PL spectra in vdW heterostructures with different *h*-BN thicknesses, respectively. Two well-separated trion and exciton peaks are observed. With elevated temperature, peak position shifted to the lower energy side due to the temperature-dependent band gap shift[142]. The trion is dominant in vdW heterostructure with Mn oxide, and component of trion in PL spectra decreased with the thickness of inserted *h*-BN spacer increasing.

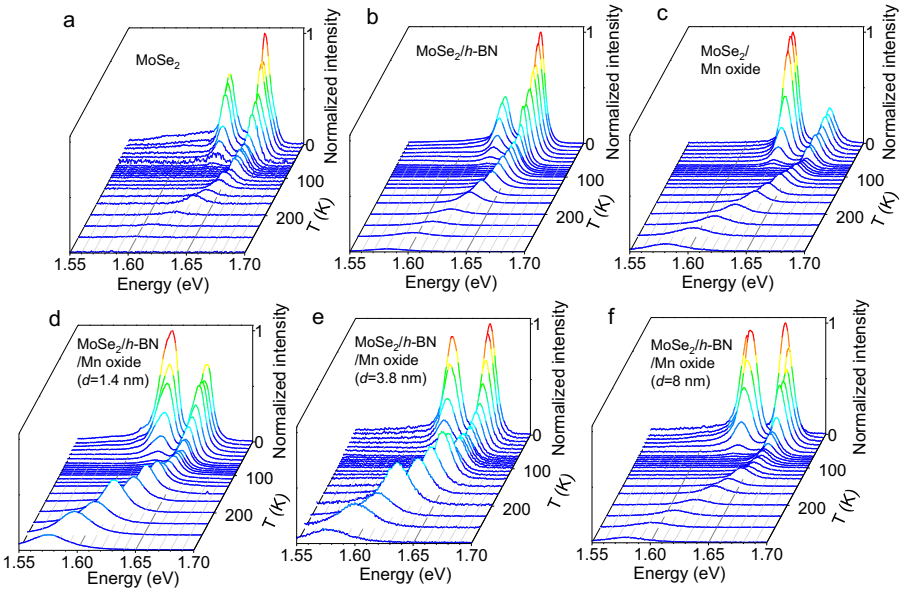

Figure 5.9. Temperature dependence of PL spectra of vdW heterostructures with different *h*-BN thicknesses. Waterfall plot of the temperature-dependent PL spectra of 1L-$MoSe_2$ on SiO_2/Si (a), $MoSe_2$ on *h*-BN (b), 1L-$MoSe_2$/Mn oxide (c), 1L-$MoSe_2$/*h*-BN/Mn oxide (d =1.4 nm) (d), 1L-$MoSe_2$/*h*-BN/Mn oxide (d =3.8 nm) (e), and 1L-$MoSe_2$/*h*-BN/Mn oxide (d=8 nm) (f).

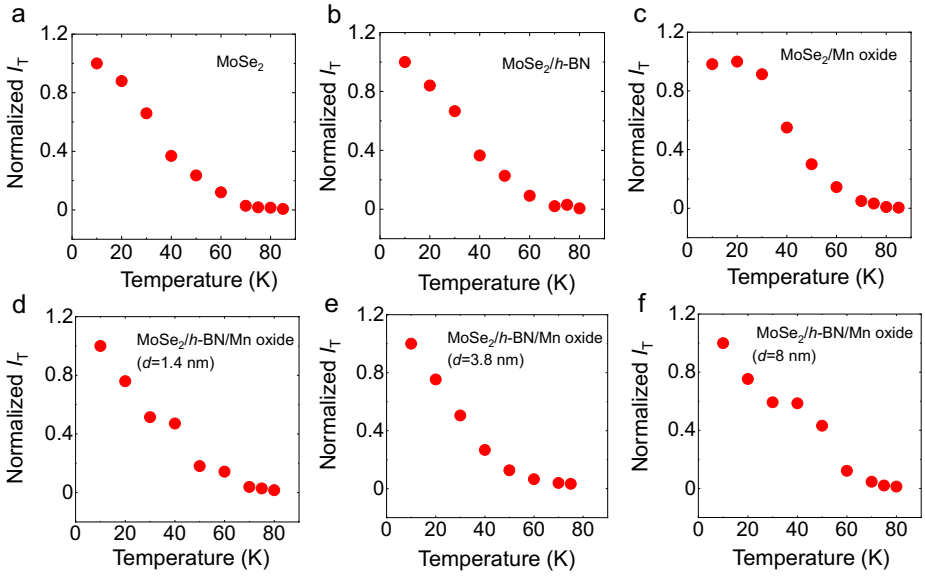

Figure 5.10. Temperature dependence of trion intensity of vdW heterostructures with different *h*-BN thicknesses (d). Temperature dependence of PL intensity of the trion of 1L-$MoSe_2$ on SiO_2/Si (a), $MoSe_2$ on *h*-BN (b), 1L-$MoSe_2$/Mn oxide (c), 1L-$MoSe_2$/*h*-BN/Mn oxide (d=1.4 nm) (d), 1L-$MoSe_2$/*h*-BN/Mn oxide with *h*-BN thickness (d= 3.8 nm) (e), and 1L-$MoSe_2$/*h*-BN/Mn oxide (d= 8 nm) (f).

Figure 5.10 shows the normalized trion PL intensity as a function of temperature with different *h*-BN thickness. The trion PL intensity decreases with increased temperature in all samples.

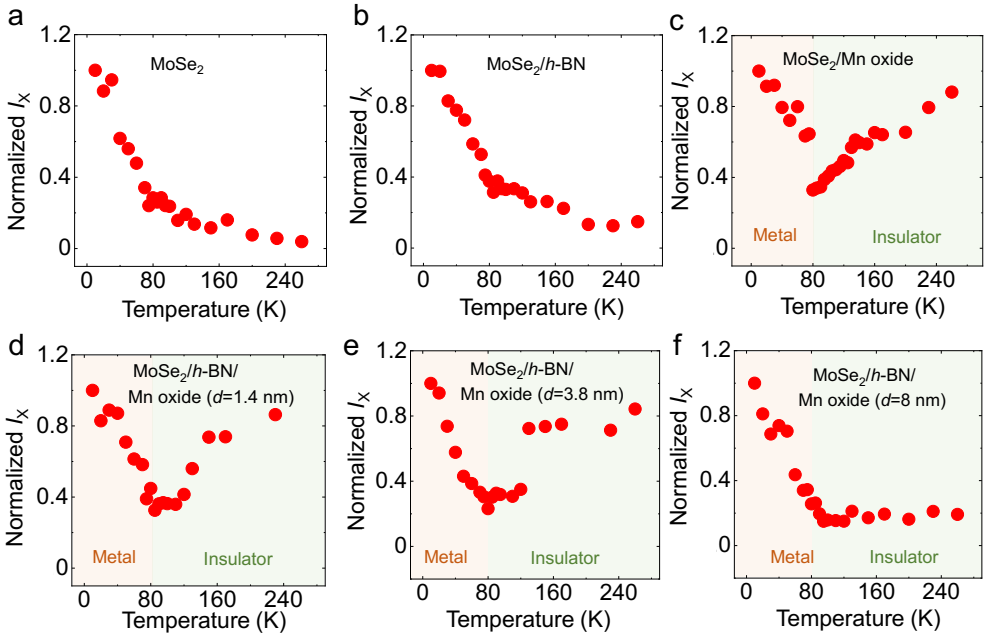

Figure 5.11. Temperature dependence of exciton PL intensity of vdW heterostructures with different *h*-BN thicknesses. Temperature dependence of normalized PL intensity of exciton of 1L-$MoSe_2$ on SiO_2/Si (a), $MoSe_2$ on *h*-BN (b), 1L-$MoSe_2$/Mn oxide (c), 1L-$MoSe_2$/*h*-BN/Mn oxide (*d*=1.4 nm) (d), 1L-$MoSe_2$/*h*-BN/Mn oxide (*d*= 3.8 nm) (e), and 1L-$MoSe_2$/*h*-BN/Mn oxide (*d*=8 nm) (f).

Figure 5.11 presents the temperature dependent exciton PL intensity. In samples without Mn oxide substrate (**Figure 5.11a, b**), the exciton PL intensity monotonously decreases. In contract, the exciton PL intensities of the heterostructures (**Figure 5.11c-e**) with thin *h*-BN decrease until the Curie temperature (80 K) of Mn oxide and then increase over 80 K. However, the exciton PL intensity in heterostructure with thick *h*-BN decreases until 300 K due to the dielectric screening effect of Mn oxide blocked by thick *h*-BN.

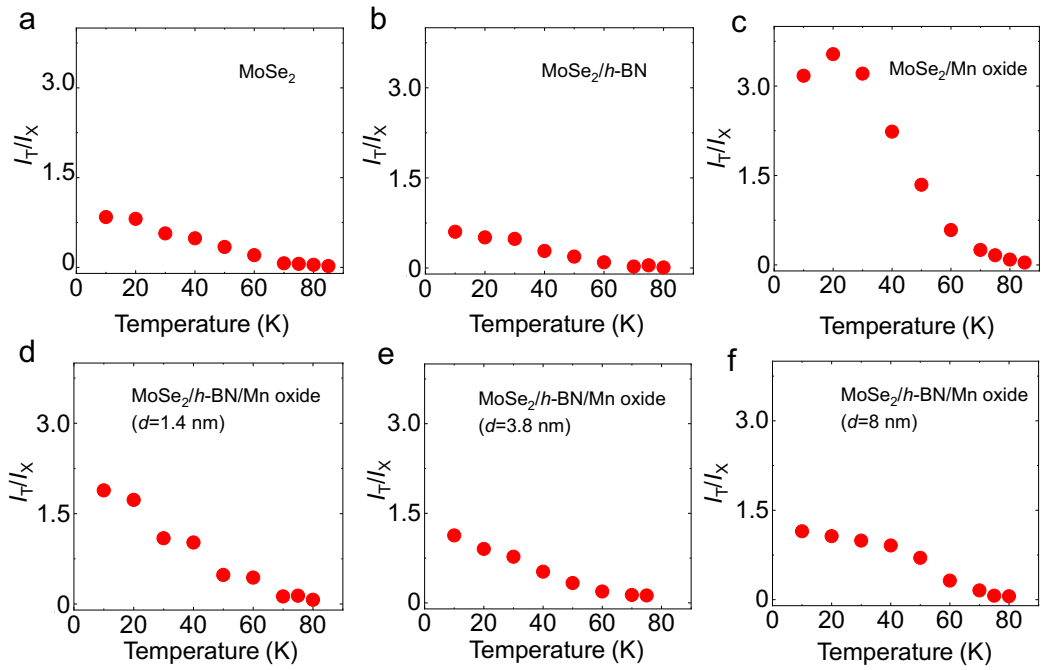

Figure 5.12. Temperature dependence of trion and exciton intensity ratio of vdW heterostructures with *h*-BN thicknesses. Temperature dependence of PL intensity ratio of the trion and exciton components of $MoSe_2$ on SiO_2/Si (a), $MoSe_2$ on *h*-BN (b), 1L-$MoSe_2$/Mn oxide (c), 1L-$MoSe_2$/*h*-BN/Mn oxide (*d*=1.4 nm) (d), 1L-$MoSe_2$/*h*-BN/Mn oxide (*d*= 3.8 nm) (e), and 1L-$MoSe_2$/*h*-BN/Mn oxide (*d*=8 nm) (f).

Figure. 5.12 shows temperature dependence of trion and exciton intensity ratio of vdW heterostructures with *h*-BN thicknesses. The 1L-$MoSe_2$ (**Figure 5.12a, b**) without Mn oxide have a lowest trion and exciton intensity ratio at 10 K. The $MoSe_2$ on Mn oxide (**Figure 5.12c**) has a largest trion exciton intensity. With the thickness of spacer *h*-BN increasing from 1.4 to 8 nm (**Figure5.12d-f**), the PL intensity ratio of I_T/I_X becomes smaller and smaller at 10 K. The physical reason can be explained by the density of doped carrier, is decreased with increasing thickness of *h*-BN. As discussed in **Section 5.3.2**, the trion and exciton PL intensity ratio is proportional to the doped carrier density

5.4.2. Estimated doped carrier density from PL intensity ratio

Figure 5.13 shows the derived PL intensity ratio I_T/I_X as a function of doped carrier density n_e[105] according to the relationship between geometric capacitance and

the back-gate voltage V_{Gate} using $n_e = |V_{\mathrm{Gate}} - V_0|\varepsilon\varepsilon_0/t_{SiO_2}$, where $V_0 = -4$ V is the back-gate voltage at charge neutrality point, ε=3.9 is the dielectric constant of silicon dioxide, ε_0 is the dielectric constant of vacuum, and the t_{SiO_2}=270 nm is the thickness of silicon dioxide. In the low carrier density regime below 2×10^{12} cm^{-2}, the PL intensity ratio linearly changes with increasing the doped carrier density[105,143] in the consideration of the effect of residual carriers (~6×10^{11} cm^{-2}), which is consistent with the analysis of the rate equation model. In this region, the relationship between PL intensity ratio and doped carrier density of $I_T/I_X = 1.4\times10^{-12}n_e$ is obtained.

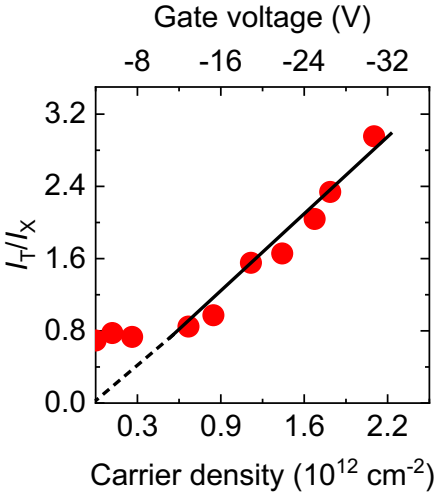

Figure 5.13. The relationship of trion and exciton intensity ratio and carrier density. The relationship between the PL intensity ratio and doped carrier density for 1L-$MoSe_2$ on SiO_2/Si under applied back-gate voltage was derived using the previously reported data[105].

5.4.3. Estimation of length scale of charge transfer

As discussed in previous sections (**5.4.1 and 5.4.2**), the linear relationship of intensity ratio and doped carrier density with slope of 1.4×10^{-12} cm^2 is calculated. Thus, I can apply this information to evaluate the doped carrier density by charge transfer from the PL spectra at 10 K in $MoSe_2$ and Mn oxide heterostructure with different *h*-BN thickness. **Figure 5.14** shows normalized PL intensity of heterostructure with different thickness of *h*-BN at 10 K.

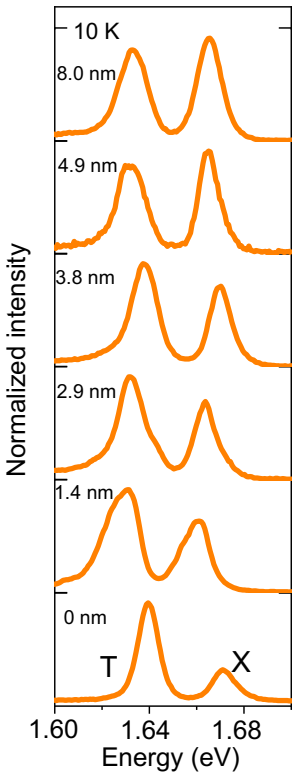

Figure 5.14. PL spectra of $MoSe_2$/*h*-BN/Mn oxide with *h*-BN thicknesses of 0, 1.4, 2.9, 3.8, 4.9, and 8.0 nm at 10 K.

The carrier density in 1L-$MoSe_2$/*h*-BN/Mn oxide vdW heterostructure with *h*-BN thickness of 0, 1.4, 3.8, and 8 nm are estimated as 2.1×10^{12}, 1.2×10^{12}, 7.1×10^{11}, and 6.2×10^{11} cm^{-2} by using I_T/I_X of 3.0, 1.7, 1.0, and 0.88, respectively, as shown in **Figure 5.15**. The error bars represent the variation of I_T/I_X depending on the position of samples (**Figure 5.16**). The evaluated doped carrier density rapidly decays with increasing distance between monolayer $MoSe_2$ and Mn oxide (thickness of *h*-BN), suggesting that the charge transfer from metallic Mn oxide to 1L-$MoSe_2$ via the tunneling barrier of *h*-BN with a higher band gap occurring within a few nanometers scale[144]. The decay profile of the charge transfer is well represented by an exponential decay with a decay length of 2.0 nm from ferromagnetic metallic Mn oxide and a constant term from residual carriers (~6×10^{11} cm^{-2}, dotted line in **Figure 5.15**) in 1L-$MoSe_2$.

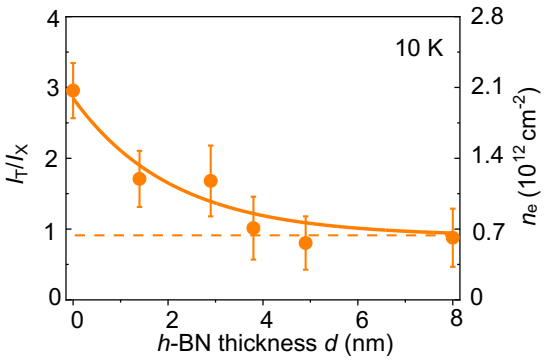

Figure 5.15. Trion and exciton intensity ratio (I_T/I_X) as a function of *h*-BN thickness (*d*). The right axis indicates the doped carrier density of $MoSe_2$ estimated from I_T/I_X. The dotted line shows the residual carrier density of ~6×10^{11} cm^{-2} in $MoSe_2$. The curve shows the fitting result with a single exponential function.

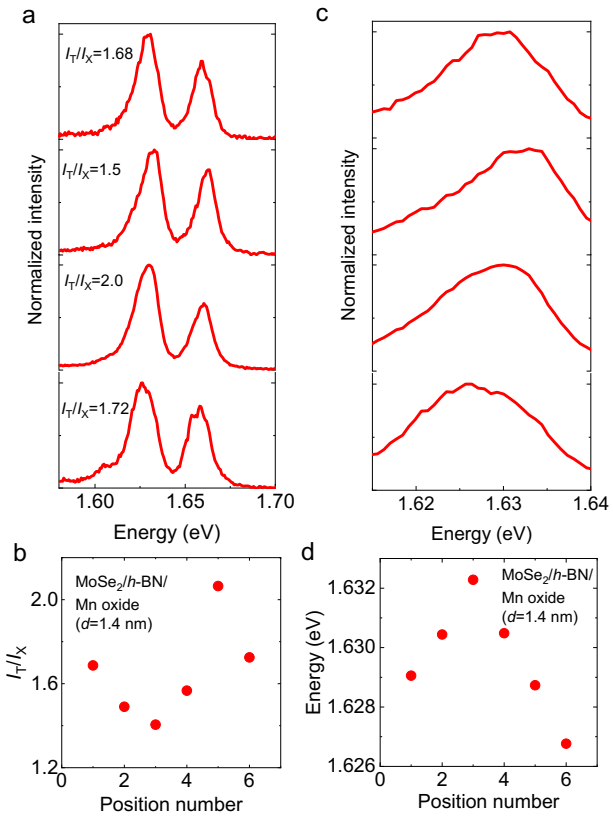

Figure 5.16. Position dependent PL spectra (a) trion and exciton intensity ratio of 1L-$MoSe_2$/*h*-BN/Mn oxide (*d* = 1.4 nm) (b). Position dependent trion PL spectra (c) and energy position (d) of 1L-$MoSe_2$/*h*-BN/Mn oxide (*d* = 1.4 nm).

5.5. Magnetic proximity effect

5.5.1. Circularly polarized PL spectra

As I have discussed previously, the Mn oxide has a phase transition from FM to PM at T_C of 80 K. In this section, I will introduce the magnetic proximity effect of 1L-$MoSe_2$ and ferromagnetic Mn oxide vdW heterostructures. **Figures 5.17a–c** show polarization-resolved PL spectra of trion in the reference (1L-$MoSe_2$/*h*-BN), vdW heterostructure (1L-$MoSe_2$/Mn oxide), and vdW heterostructure (1L-$MoSe_2$/*h*-BN/Mn oxide, d = 1.4 nm) under an out-of-plane applied magnetic field of 1 T at 10 K. The PL spectra of 1L-$MoSe_2$ with σ+ and σ− circularly polarized light components excited under σ+ excitation are shown in red and blue, respectively. Enhanced valley polarization and Zeeman splitting are not observed in 1L-$MoSe_2$/Mn oxide (**Figure 5.17b** and **Figure 5.18**) compared with the reference (**Figure 5.17a**).

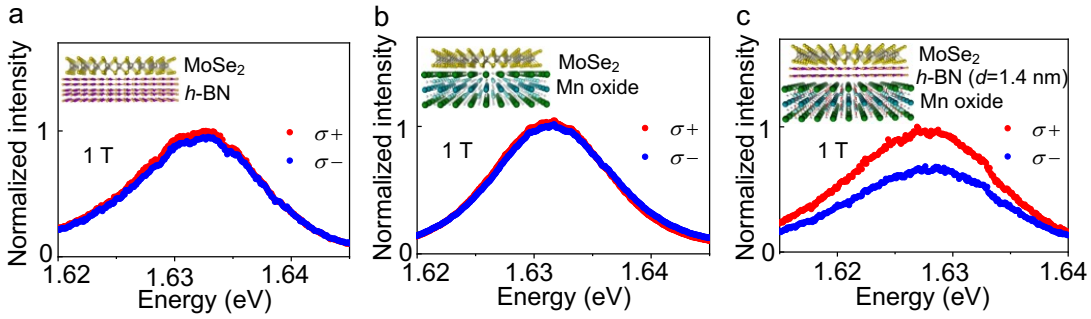

Figure 5.17. (a) Circular polarization-resolved PL spectra for the trion of the reference (1L-$MoSe_2$/*h*-BN), (b) vdW heterostructure (1L-$MoSe_2$/Mn oxide), and (c) vdW heterostructure (1L-$MoSe_2$/*h*-BN/Mn oxide, d = 1.4 nm) at 10 K under 1 T, where red and blue dots correspond to σ+ and σ− components, respectively.

However, large valley splitting, and polarization are obtained when a thin *h*-BN layer (d = 1.4 nm) is inserted between $MoSe_2$ and Mn oxide, which suggests that a thin insulating layer, such as *h*-BN, plays an important role in the enhancement of valley splitting. This behavior could be explained by the simultaneous ferromagnetic and metallic properties of Mn oxide below T_C, which is caused by the double-exchange

interactions between Mn^{3+} and Mn^{4+} ions[123]. The e_g electron states of Mn sites are strongly hybridized with O 2*p* states and change from localized to itinerant nature in the MnO_3 network[119]. In the vdW heterostructure (1L-$MoSe_2$/Mn oxide) below T_C, metal-induced gap states (MIGS) are formed at the interface between metallic Mn oxide and MoSe[145–147]. The itinerant e_g electrons, thus, move to new conductive channels formed by MIGS, instead of hoping between Mn^{3+} and Mn^{4+} sites; this prevents the formation of the ferromagnetic phase in the Mn oxide. Moreover, the orbital hybridization at the interface between the Mn oxide and $MoSe_2$ disturbs the electronic states of the MnO_3 network, which would cause the loss of magnetization at the surface of the Mn oxide[148]. In contrast, for the vdW heterostructure (1L-$MoSe_2$/*h*-BN/Mn oxide) comprising an extremely thin *h*-BN that possesses a large band gap, the MIGS and orbital hybridization are not formed at the interfaces between Mn oxide and 1L-$MoSe_2$ by inserting the *h*-BN, leading to the magnetic proximity effect for $MoSe_2$[149].

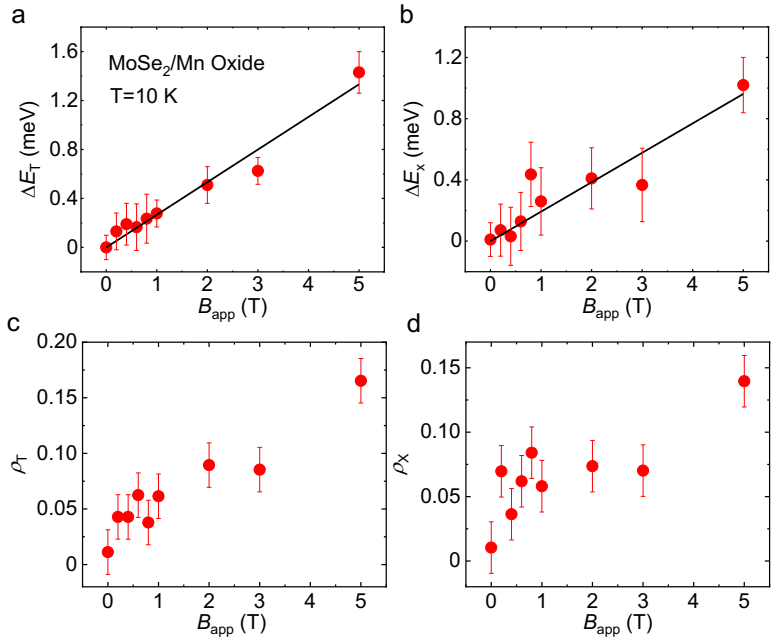

Figure 5.18. Valley splitting of the trion (a) and exciton (b) peak of 1L-$MoSe_2$/Mn oxide at 10 K, which are linearly fitted. Valley polarization of the trion (c) and exciton (d) peak of 1L-$MoSe_2$/Mn oxide at 10 K. The error bars of valley splitting come from the CCD pixel size (about 0.1 meV) and the fitting procedure. The error bars of valley polarization represent the uncertainties of polarization-resolved measurements.

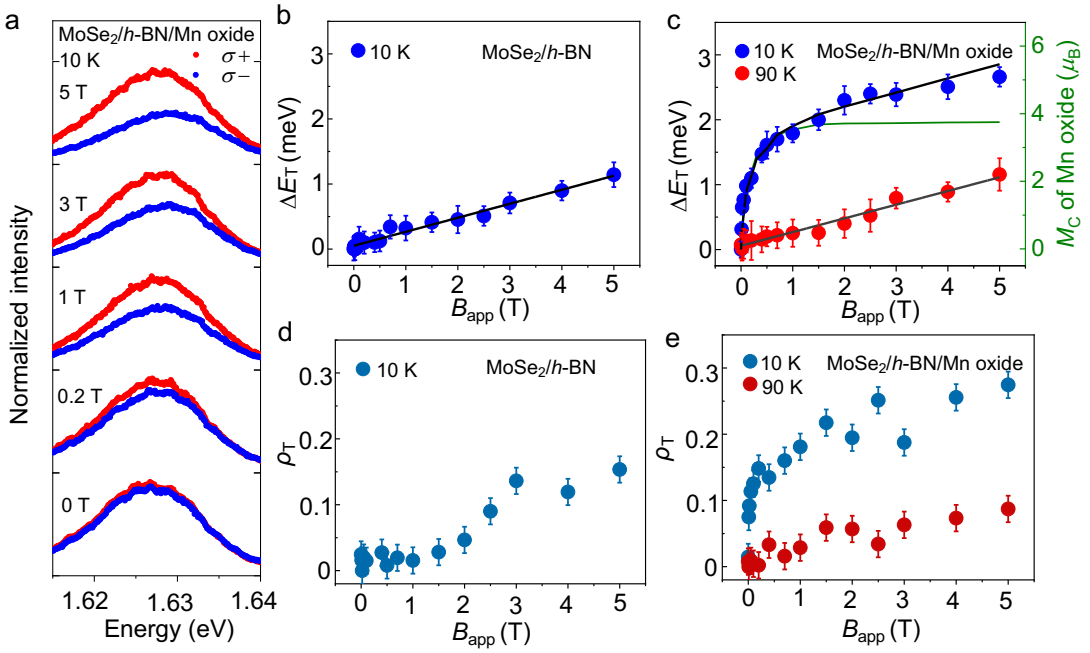

Figure 5.19. (a) Valley splitting of the trion in vdW heterostructure (1L-$MoSe_2$/*h*-BN/Mn oxide, d = 1.4 nm) at 10 K under different magnetic field conditions. (b) Trion valley splitting of 1L-$MoSe_2$/*h*-BN as a function of applied magnetic field at 10 K. The line is linear fit to the experiment data. (c) Applied magnetic field dependence of trion valley splitting of vdW heterostructure (1L-$MoSe_2$/*h*-BN/Mn oxide, d = 1.4 nm). The blue and red dots show data at 10 and 90 K, where the Mn oxide is ferromagnetic and paramagnetic state, respectively. The solid green curve shows the out-of-plane magnetization (M_C) of Mn oxide at 10 K under an applied magnetic field of 0.5 T after cooling down to zero field. The grey line is linear fit at 90 K. The black line shows the fitted curve at 10 K, considering the applied magnetic field and the effect of localized spin in Mn oxide. (d) Magnetic field-dependent valley polarization of the trion in the reference at 10 K. (e) Magnetic field-dependent valley polarization of the trion in the vdW heterostructure at 10 and 90 K. The error bars in **Figure 5.19e, f** come from uncertainties of determination of peak energy due to the CCD pixel size (about 0.1 meV) and fitting procedures. The error bars in **Figure 5.19g, h** represent the uncertainties of polarization-resolved PL measurements.

Figure 5.19a shows the polarization-resolved PL spectra of the trion of 1L-$MoSe_2$/*h*-BN/Mn oxide (d = 1.4 nm) at 10 K under different magnetic fields from 0 to

5 T. The σ+ and σ− components of the PL spectra of the vdW heterostructure have an identical intensity and spectral shape under a zero-magnetic field[62,64], because the net magnetization of ferromagnetic Mn oxide with soft magnetic properties is zero at 0 T [123]. By increasing the applied magnetic field, the PL spectrum of the σ+ component shows a higher intensity than that of the σ− component. In addition, the shift of σ+ and σ− PL peaks to lower and higher energy positions for $E_{\sigma+}$ and $E_{\sigma-}$, respectively, is observed, corresponding to the valley splitting of $MoSe_2$ under a magnetic field.

Valley splitting of trions in the vdW heterostructure quantifies the Zeeman effect and magnetic proximity effect[72,89,104,150]. **Figure 5.19b** shows the trion valley splitting of the reference (1L-$MoSe_2$/*h*-BN) as a function of applied magnetic field. The trion valley splitting shows a linear increase as a function of the applied magnetic field, and the coefficient of valley splitting is evaluated as ~0.21 meV/T, which is quantitatively consistent with the previously reported results for monolayer TMD induced by the Zeeman effect under external magnetic fields[89,104]. **Figure 5.19c** shows the applied magnetic field-dependent valley splitting of trions in the vdW heterostructure (1L-$MoSe_2$/*h*-BN/Mn oxide, d = 1.4 nm) at 10 K (blue) below T_C and 90 K (red) above T_C. The trion valley splitting also linearly increases with the applied magnetic field at 90 K, where the Mn oxide of the vdW heterostructure is in the PM phase. The value of the linear coefficient of trion valley splitting is evaluated as 0.22 meV/T, and the effective *g*-factor can be extracted to be 3.6, both of which are consistent with the values of the reference (1L-$MoSe_2$/*h*-BN, **Figure 5.19b**).

Large and nonlinear trion valley splitting of the vdW heterostructure was experimentally observed at 10 K in the FM phase of Mn oxide below T_C. The valley splitting of trions increases rapidly and nonlinearly from 0 to 1 T and gradually increases above 1 T, suggesting that 1L-$MoSe_2$ in the vdW heterostructure experiences both the effective magnetic field (B_{eff}) due to the magnetic proximity effect from ferromagnetic Mn oxide and the applied external magnetic field (B_{app}). The valley splitting of trions is described, considering the magnetic proximity effect from Mn oxide, as follows:

$$\Delta E_{\mathrm{T}} = \Delta E_{\mathrm{eff}} + \Delta E_{\mathrm{app}} = g\mu_{\mathrm{B}}\left(B_{\mathrm{eff}} + B_{\mathrm{app}}\right), \tag{5.8}$$

where ΔE_{eff} and ΔE_{app} are the valley splitting caused by B_{eff} and B_{app}, respectively[151]. The experimental result of valley splitting in **Figure 5.19c** can be reproduced using **Eq. (5.8),** as shown in the black curve with a maximum effective magnetic field of ~7.6 T, when the out-of-plane magnetization (M_{C}, green line in **Figure 5. 19c**) in Mn oxide becomes saturated. In addition, the valley splitting of the exciton is enhanced at 10 K in the vdW heterostructure with a thin *h*-BN of d = 1.4 nm (**Figure 5.20**). These results indicate that the large and nonlinear enhancement in the valley splitting of 1L-$MoSe_2$ is induced by the magnetic proximity effect from Mn oxide in the vdW heterostructure.

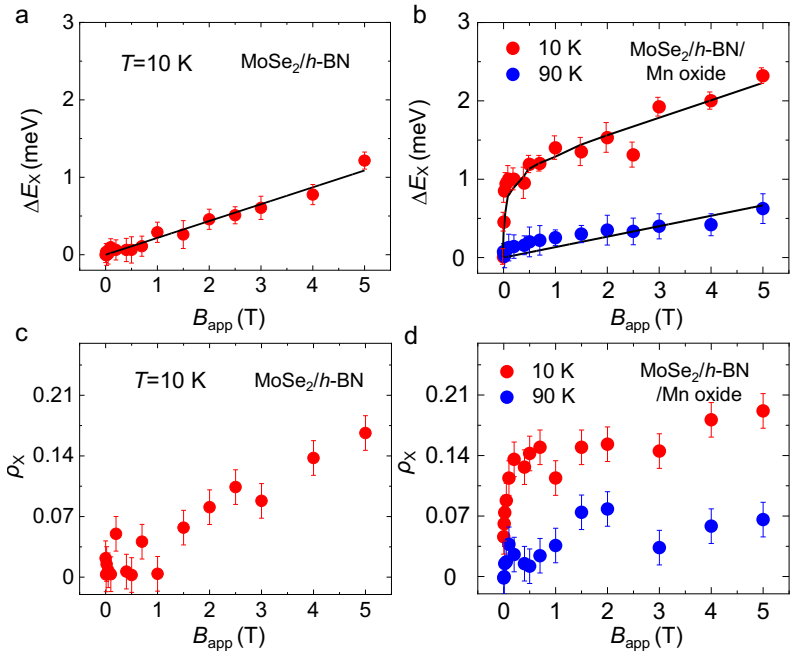

Figure 5.20. (a) Valley splitting of exciton PL peak in 1L-$MoSe_2$/*h*-BN at 10 K. (b) Valley splitting of exciton PL peak in 1L-$MoSe_2$/*h*-BN/Mn oxide (d = 1.4 nm) at 10 and 90 K under applied magnetic field from 0 to 5 T. (c) Valley polarization of exciton PL peak in reference (1L-$MoSe_2$/*h*-BN) at 10 K (b) Valley polarization of exciton PL peak in 1L-$MoSe_2$/*h*-BN/Mn oxide (d = 1.4 nm) at 10 and 90 K. The error bars of **Figure 5.20a** come from the CCD pixel size (about 0.1 meV) and the fitting procedure. The error bars of **Figure 5.20b** represent the uncertainties of polarization-resolved measurements.

Valley splitting in the magnetic field breaks the valley degeneracy, enabling the control of valley polarization[62]. **Figures 5.19d, e** show the magnetic field dependence of the valley polarization of trions (ρ_T) in the reference and vdW heterostructure at 10 K, respectively. The ρ_T of the reference shows a linear increase with the applied magnetic field. In contrast, the ρ_T of the vdW heterostructure exhibits a nonlinear behavior, similar to the valley splitting due to the magnetic proximity effect of ferromagnetic Mn oxide underneath at 10 K. Moreover, a smaller valley polarization of the vdW heterostructure is observed at 90 K above T_C, as shown in **Figure 5.19e**, which is attributed to the disappearance of the magnetic proximity effect from the paramagnetic phase of Mn oxide.

5.5.2. Length scale of magnetic proximity effect

Figure 5.21 shows the circular polarization-resolved PL spectra of trions in vdW heterostructures (1L-$MoSe_2$/*h*-BN/Mn oxide) under an out-of-plane magnetic field of 1 T at 10 K. With increasing the *h*-BN thickness from 1.4 to 8.0 nm, the valley splitting and valley polarization of trions are reduced, indicating a weaker magnetic proximity effect of ferromagnetic Mn oxide. Note that no enhanced valley lifting is observed in 1L-$MoSe_2$/Mn oxide (d = 0 nm) (**Figure 5.17b** and **Figure 5.18**). By inserting an extremely thin *h*-BN, valley splitting, and polarization become obvious due to the magnetic proximity effect compared with the reference (1L-$MoSe_2$/*h*-BN). Importantly, the anomalous behavior of small valley splitting appears in 1L-$MoSe_2$/Mn oxide without *h*-BN, showing no magnetic proximity effect of ferromagnetic Mn oxide underneath. The reason for the behavior was explained in the previous section.

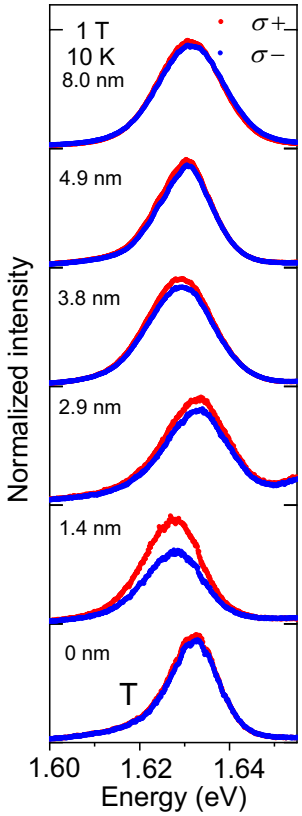

Figure 5.21. Circular polarization-resolved PL spectra for the trion of 1L-$MoSe_2$/*h*-BN/Mn oxide with *h*-BN thicknesses of 0, 1.4, 2.9, 3.8, 4.9, and 8.0 nm under 1 T at 10 K.

Figure 5.22 shows the decay behavior of the magnetic proximity effect arising from ferromagnetic Mn oxide on 1L-$MoSe_2$ at 10 K under 1 T. The left axis is the effective valley splitting (ΔE_{eff}) due to the magnetic proximity effect, and the right axis is the effective magnetic field (B_{eff}) calculated using **Eq. (5.8)**. The magnetic proximity effect in 1L-$MoSe_2$ from FM Mn oxide quickly decays with increasing *h*-BN thickness. The length scale of a few nanometers cannot be understood by the leakage magnetic field obeying the Biot–Savart law from FM Mn oxide because the typical size of ferromagnetic Mn oxide in the vdW heterostructure is a large value of several tens of micrometers. A decay of a few nanometers in the experimental result suggests a direct exchange interaction between the ferromagnetic spins of Mn oxide and the excitonic states in K+ and K– of 1L-$MoSe_2$ via the magnetic proximity effect. Experimentally, a large effective magnetic field reaching over 7 T is obtained in the vdW heterostructure

with the bilayer *h*-BN. A larger effective magnetic field of over 15 T is predicted in the 1L-$MoSe_2$/*h*-BN/Mn oxide using a thinner *h*-BN monolayer, according to the extrapolation of experimental results in **Figure 5.22** and the *ab initio* theoretical calculation.[152,153] These results reveal that the effective magnetic field decays within a few nanometers due to exchange interactions between 1L-$MoSe_2$ and atomically flat ferromagnetic materials via the magnetic proximity effect.

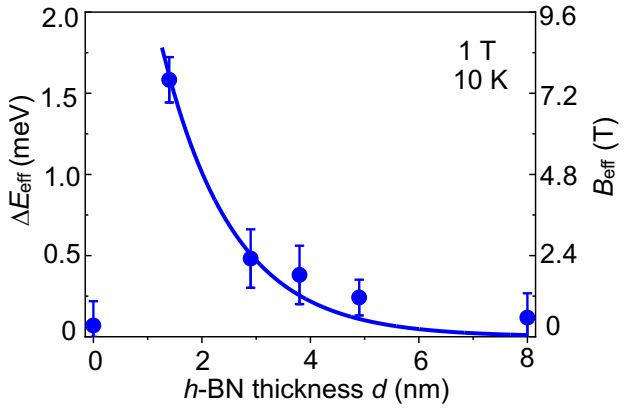

Figure 5.22. Effective valley splitting of trion as a function of *d*. The right axis shows the effective magnetic field arising from the localized spins of Mn oxide to $MoSe_2$. The solid curve shows the fitting result with a single exponential function.

5.6. Chapter summary

In summary, I have studied the charge transfer and magnetic proximity effect for excitons and trions in the 1L-$MoSe_2$/*h*-BN/Mn oxide vdW heterostructure. The discontinuous change in the dielectric screening of excitons is attributed to the metal-to-insulator transition of Mn oxide. The higher I_T/I_X of the vdW heterostructure than that of the reference is caused by the charge transfer to 1L-$MoSe_2$ from metallic Mn oxide below T_C. Moreover, large excitonic valley splitting and polarization have been demonstrated by the ferromagnetic spins of the ferromagnetic-metallic states of Mn oxide with a bilayer *h*-BN between semiconducting TMD and ferromagnetic metal, which provides a new experimental approach to introduce a ferromagnetic metal substrate, thereby lifting the valley degeneracy of TMD with a strong magnetic proximity effect. The vdW structures using electronic and magnetic phase transition

materials demonstrated here can provide new opportunities for the modulation and controllability of excitonic states via dielectric screening, charge carriers, and magnetic spins.

Chapter 6. Magnon coupled intralayer moiré trion in 1L-$MoSe_2$ and antiferromagnet heterostructure

6.1. Introduction

Artificial vdW heterostructures composed of monolayer 2D materials have attracted much attention, because it provides novel platform for studying both fundamental physics and device applications[71,154]. The vdW heterostructures give new approaches towards emerging physical properties of interfaces between individual 2D layers. The vertically stacked 2D materials such as graphene and TMDs with a twisted angle or lattice mismatch in the artificial vdW heterostructures could lead the formation of moiré pattern because of the spatially varying atomic registry, which gives rise to pronounced physical phenomena including strongly-correlated insulator phase[31,155], superconductivity[156] and moiré exciton[30,157,158]. Here, the moiré exciton arising from a bound electron-hole pair by Coulomb interaction, is confined in the periodic potential of moiré pattern. Moreover, both intralayer and interlayer excitons formed by layer-locked and layer-separated bound electrons and holes, respectively, exhibit obvious moiré signatures in semiconducting bilayer TMDs vdW heterostructures[29,158,159]. The intralayer and interlayer excitons modulated by the moiré potential result in a spatially organized array of excitons ensemble in the moiré superlattice. The moiré excitons in moiré superlattice have the potential for quantum simulation of many-body physics and dense array of coherent quantum emitters, which could be useful for applications in quantum optics.

Since the discovery of ferromagnetic and antiferromagnetic layered 2D materials, the intriguing magnetic properties of 2D materials have been considerably interesting in the research fields of material science. Among 2D layered magnetic materials, transition metal phosphorous dichalcogenides ($TMPX_3$, TM=Mn, Ni, Fe, Co; X=S, Se) have been extensively studied as a model system of layered magnetic materials[160,161].

For instance, the free exciton coupled by magnon was reported in both $MnPS_3$ bulk[162] and the heterostructure of semiconducting $MoSe_2$ and antiferromagnetic $MnPSe_3$[163]. Moreover, a novel exciton with an ultra-narrow PL peak was found in bulk $NiPS_3$[164–166], which arises from many-body states of Zhang-rice singlet and reaches a coherent state assisted with antiferromagnetic order[166]. However, the interaction between the moiré excitonic states (exciton and trion) and magnetic elementary excitation in the magnetic materials has yet to be fully studied in experiment. To explore novel quantum phenomena in moiré superlattices, it is important to prove the moiré excitonic states (exciton and trion) coupled with magnetic elementary excitation, which will provide the intriguing properties of moiré excitonic system with magnetic functionalities.

In this chapter, I will introduce the emergence of intralayer trions localized in the moiré potentials formed by twisted monolayer $MoSe_2$ and antiferromagnetic $MnPS_3$ vdW heterostructure.

6.2. Optical image and typical PL spectrum

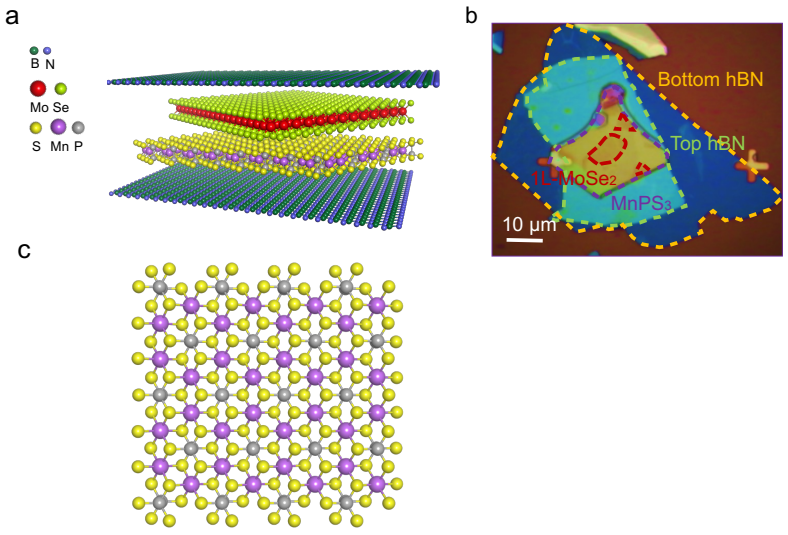

Figure 6.1. (a) Schematic diagram of *h*-BN encapulated 1L-$MoSe_2$/$MnPS_3$ vdW heterostructure. (b) Optical image of 1L-$MoSe_2$/$MnPS_3$ vdW heterostructure with scale bar of 10 μm. The top and bottom *h*-BN are shown in green and yellow dotted line, respectively. The 1L-$MoSe_2$ is highlighted in red, and $MnPS_3$ is shown in purple dotted line. (c) Structure of $MnPS_3$.

Figure 6.1a shows the schematic diagram of *h*-BN encapsulated $MoSe_2/MnPS_3$ heterostructure. **Figure 6.1b** shows the optical image of 1L-$MoSe_2/MnPS_3$ vdW heterostructure, where the edges of 1L-$MoSe_2$ and $MnPS_3$ are highlighted in red and purple dotted lines, respectively. $MnPS_3$ has been of great interest from its realization in the antiferromagnetic 2D anisotropic Heisenberg model on a honeycomb lattice as shown in **Figure 6.1c**[167]. $MnPS_3$ is a layered antiferromagnetic material with Néel temperature of T_N at about 78 K as suggested in **Figure 6.2**.

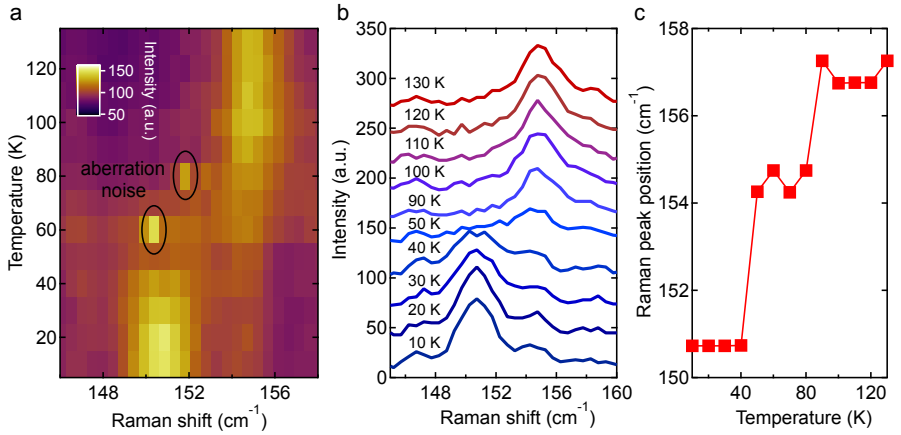

Figure 6.2. (a) Contour map of temperature dependent Raman shift of $MnPS_3$. (b) Raman spectra of $MnPS_3$ at various temperatures. (c) Raman peak position as a function of temperature. From these results, I can estimate T_N of $MnPS_3$ is around 78 K, which is consistent with the previous report[167].

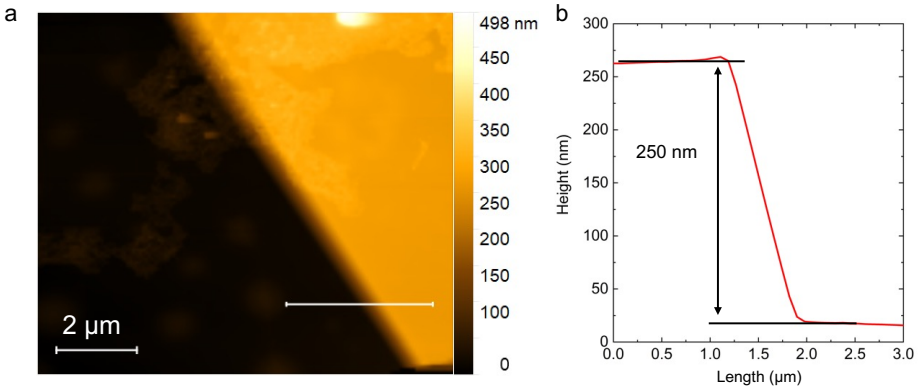

Figure 6.3. (a) Atomic force microscopy (AFM) image of $MnPS_3$ encapsuled with layers of *h*-BN. (b) Height profile corresponding to the thickness of $MnPS_3$ obtained along the edge, as indicated by the white line in the image. The thickness of $MnPS_3$ is determined by about 250 nm.

The thickness of $MnPS_3$ measured by atomic force microscopy (AFM) was ~250 nm as shown in **Figure 6.3**. The vdW heterostructures were prepared by poly-procarbonate (PPC) based viscoelastic dry-transfer techniques[78]. The stacking angle between individual layers was controlled to be nearly commensurate according to the cleaved flake and crystal edges[168]. The zigzag direction of 1L-$MoSe_2$ is parallel to that of honeycomb structure of $MnPS_3$.

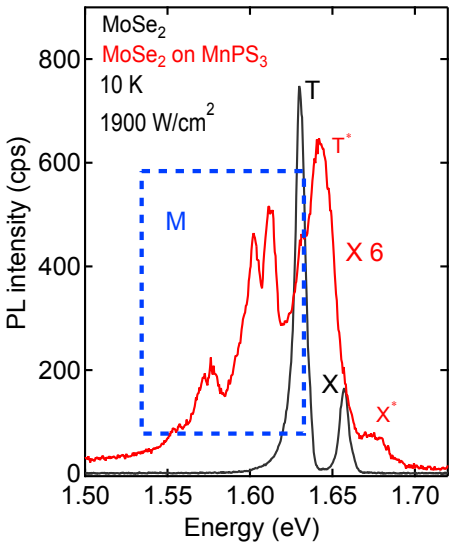

Figure 6.4. PL spectra of 1L-$MoSe_2$ and 1L-$MoSe_2$/$MnPS_3$ vdW heterostructure, which are presented in black and red line, respectively. The PL intensity of the heterostructure shown here is multipled 6 times. The peaks of T* and X* are assigned as emissons from trion and excitons, respectively. The lower enegy additional peaks is denoted in the blue dotted box as M.

Figure 6.4 presents the PL spectra of 1L-$MoSe_2$/$MnPS_3$ vdW heterostructure (red line) and 1L-$MoSe_2$ (black line) for reference at 10 K under a low excitation power condition. The PL spectrum of 1L-$MoSe_2$ shows well-separated and narrow two excitonic emissions assigned as neutral free excitons (X) at 1.657 eV and free charged excitons, free trions (T) at 1.631 eV, which is well consistent with the previous reported results[24,169]. In contrast, the PL spectrum of 1L-$MoSe_2$/$MnPS_3$ heterostructure is strikingly different from 1L-$MoSe_2$. The PL spectrum of 1L-$MoSe_2$/$MnPS_3$ heterostructure has additional fine peaks (M) at lower energy side, besides exciton peak (X*) at 1.671 eV and trion peak (T*) at 1.643 eV. The large upshift of two PL peaks

(X* and T*) in the vdW heterostructure with antiferromagnetic $MnPS_3$ is observed, which suggests that the magnons in an antiferromagnetic material strongly couple with excitonic states in 1L-$MoSe_2$[163]. This behavior will be explained in the next section.

6.3. Magnon-exciton coupled excitonic states

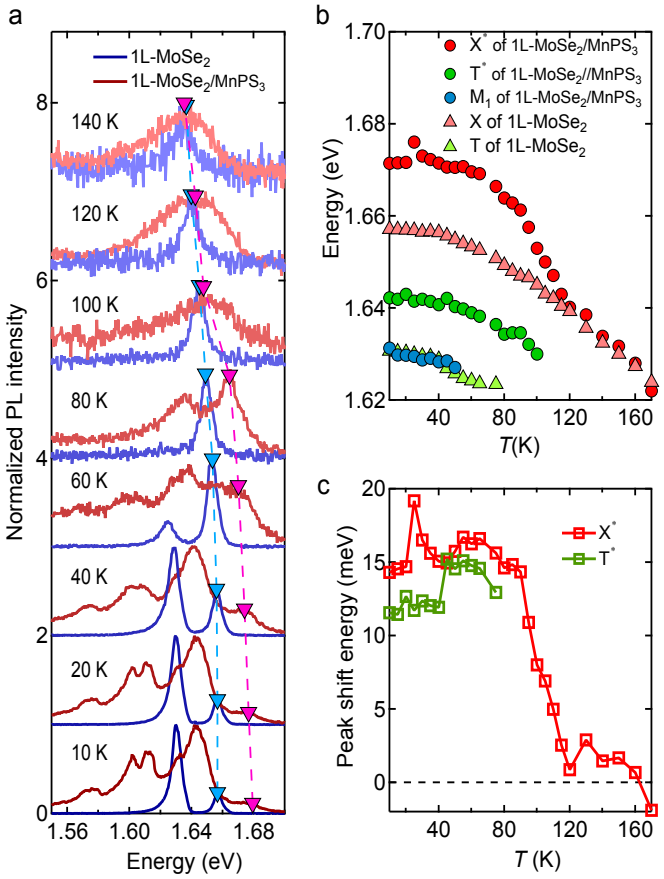

Figure 6.5. (a) Temperature dependence of PL spectra in 1L-$MoSe_2$ (blue) and 1L-$MoSe_2$/$MnPS_3$ (red), respectively. The dotted curves with makers are guidelines for peak energy positions for exciton related peaks of 1L-$MoSe_2$ and 1L-$MoSe_2$/$MnPS_3$. (b) Temperature (T) dependent PL peak position of free excitons (X) in 1L-$MoSe_2$ (red dots), excitons (X*) in 1L-$MoSe_2$/$MnPS_3$ heterostructure (red triangles), trions (T) in 1L-$MoSe_2$ (green dots), trions (T*) in 1L-$MoSe_2$/$MnPS_3$ heterostructure (green triangles), and M_1 in 1L-$MoSe_2$/$MnPS_3$ heterostructure (blue dots) at 10 K. (c) Peak shift of exciton (red square line) and trion related peak (green square line) of 1L-$MoSe_2$/$MnPS_3$ heterostructure compared with corresponding exciton and trion in 1L-$MoSe_2$ at 10 K.

Figure 6.5a shows the temperature dependence of PL spectra in 1L-$MoSe_2$ and 1L-$MoSe_2$/$MnPS_3$ vdW heterostructure. The PL peak of exciton (X) in 1L-$MoSe_2$ shows gradually downshift (light blue dotted line), while that of exciton (X*) in the vdW heterostructure shows sudden shift below ~90 K with additional gradual downshift in elevating temperature (red dotted line), which is around Néel temperature of $MnPS_3$ (78 K, **Figure 6.3**)[167] . The PL peaks energies of exciton (X) and trion (T) and those (X* and T*) and lower energy peak (M_1) are shown as a function of temperature in **Figure 6.5b**.

The peak energies of trion (T: blue dots) and exciton (X: black dots) in 1L-$MoSe_2$ well follow the temperature dependent band gap shifts[132,170], as shown in **Figure 6.6**. The band gap of 1L-$MoSe_2$ as a function of temperature can be described using the relationship as bellow[132]:

$$E(T) = E_0 - S\hbar\omega \left[\coth\left(\frac{\hbar\omega}{2k_BT}\right) - 1\right], \quad (6.1)$$

where E_0 is the energy positions of exciton (trion) at the lowest temperature limit, S represents a dimensionless coupling constant, and $\hbar\omega$ is an average phonon energy. **Figure 6.6** illustrates temperature dependent peak energy position of X (black dots) and T (blue dots) in 1L-$MoSe_2$. The black and blue solid curves are fitting results using **Eq. (6.1)** for X and T, respectively. From the fitting results, I extract for X(T) with the value of E_0=1.657 (1.630) eV, S= 1.99 (2.55), and $\hbar\omega$= 15 (15) meV, which are consistent with previous report[170]. Thus, the 1L-$MoSe_2$ sample is a reliable reference to compare its PL emission peak position with 1L-$MoSe_2$/$MnPS_3$ heterostructure.

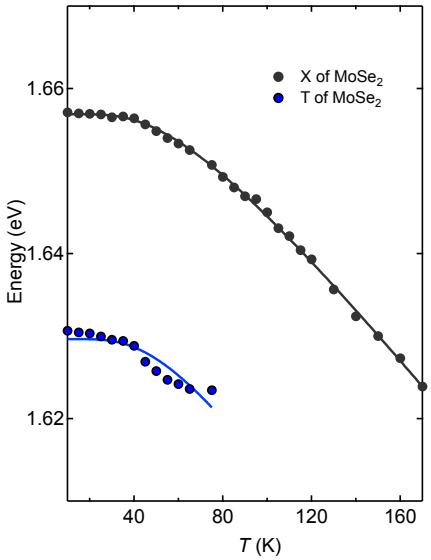

Figure 6.6. Temperature dependent peak energy positions of X (black dots) and T (blue dots) of 1L-$MoSe_2$.

Both peak energies of trion (T*: green squares) and exciton (X*: red squares) in vdW heterostructure are clearly upshifted below ~90 K and gradually reach to those (T and X) in reference of 1L-$MoSe_2$, which is consistent with the previously reported results[170]. The peak energy difference of exciton and trion between 1L-$MoSe_2$ and 1L-$MoSe_2$/$MnPS_3$ vdW heterostructure are plotted in **Figure 6.5c**. Peak energy positions were determined by fitting procedures using Voight functions. The upshifted peak energy of exciton is about 15 meV and significantly decreases at ~90 K, which is very close to Néel temperature of T_N (~78 K) in $MnPS_3$. Moreover, the upshifted peak energy difference tends to be zero at high temperature. The value of peak upshifted energy (15 meV) below T_N is close to magnon energy near the Brillouin zone edge along the direction of basal plane, which is revealed by neutron scattering measurement of bulk $MnPS_3$[171]. In **Figure 6.5c**, the upshift of trion peak is observed as well. The energy upshifted excitonic states (exciton and trion) suggest the exciton (trion)-magnon complex with assist of magnon absorption in the 1L-$MoSe_2$/$MnPS_3$ vdW heterostructure below antiferromagnetic ordering temperature (T_N)[163].

6.4. Confirmations of moiré trion-magnon complex

6.4.1. Moiré superlattice

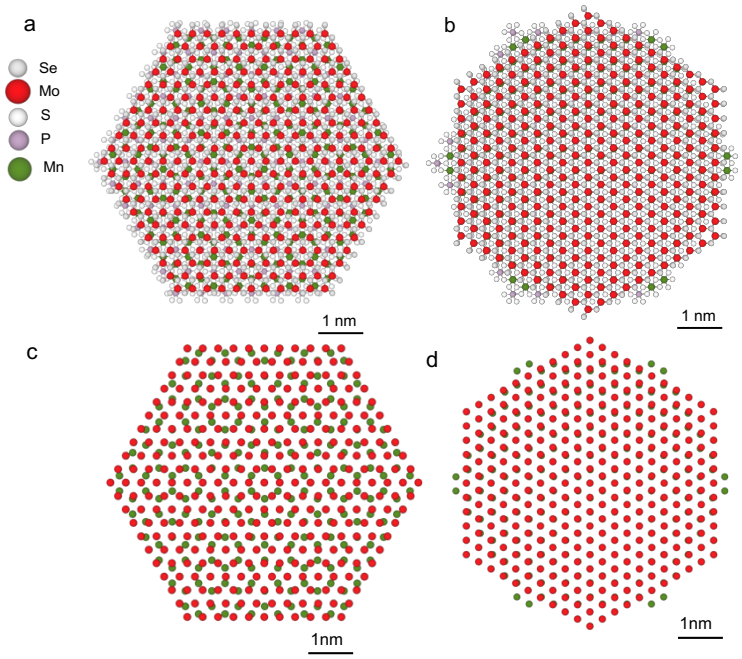

Figure 6.7. (a) Top view of 1L-$MoSe_2$ and the $MnPS_3$ vdW heterostructure with parallel configuration. (b) Top view of 1L-$MoSe_2$ and the $MnPS_3$ vdW heterostructure with perpendicular configuration. (c) The top view of heterostructure of parallel configuration with Mo and Mn atoms. (d) The top view of heterostructure of perpendicular configuration with Mo and Mn atoms. The Mo atoms of $MoSe_2$ and Mn atoms of $MnPS_3$ play an important role to the formation of moiré patterns.

The moiré superlattice can naturally form due to the lattice mismatch and/or rational alignment between 1L-$MoSe_2$ and $MnPS_3$ in the stacking vdW heterostructure. The lattice mismatch of monolayer $MoSe_2$ (2×2 superlattice) and bulk $MnPS_3$ ($Mn_2P_2S_6$) with parallel and perpendicular configuration is 12.5 and 1%, respectively, with considering the difference of lattice constant ($MoSe_2$:3.32 Å, $Mn_2P_2S_6$:5.81 Å), as shown schematically in **Figure 6.7**. The parallel (perpendicular) configuration means zigzag-edge of $MoSe_2$ parallel (perpendicular) to the zigzag-edge of Mn^{2+} with forming a honeycomb lattice in $MnPS_3$. **Figure 6.7a** shows the superlattice in parallel configuration, indicating a clear moiré pattern with a period of ~2.3 nm. **Figure 6.7b**

shows the superlattice in perpendicular configuration with the same atomic scale to **Figure 6.7a**, however, the moiré pattern is no longer observed, because of smaller lattice mismatch with much larger moiré period.

6.4.2. Temperature dependence of PL spectra

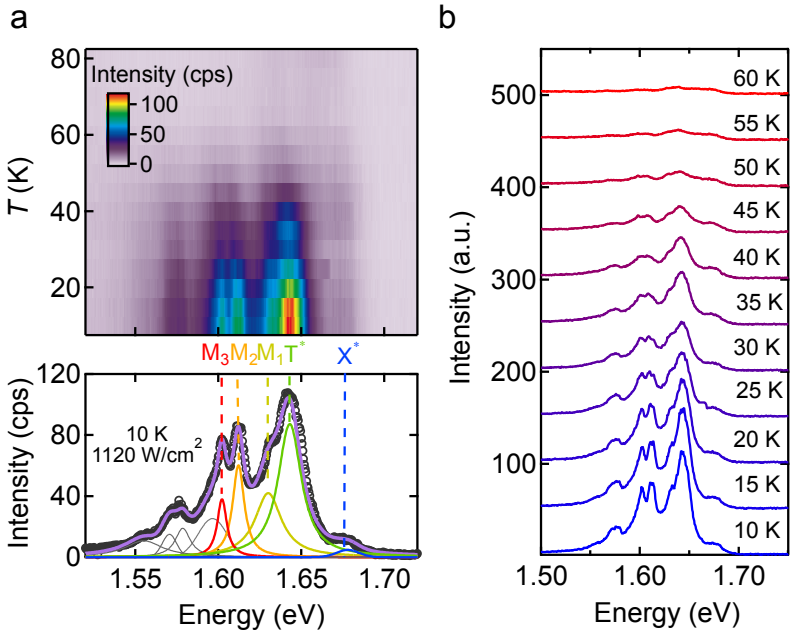

Figure 6.8. (a) Contour plot of temperature dependent PL in 1L-$MoSe_2$/$MnPS_3$ (Top). The bottom figure shows the PL spectrum of 1L-$MoSe_2$/$MnPS_3$ at 10 K under an excitation power density of 1120 W/cm^2 from the contour plot. The M_1, M_2, and M_3 are assigned as intralayer excitons trapped by moiré potentials. T* and X* are trion and excitons, respectively. (b) PL spectra at various temperatures from 10 to 60 K.

The top of **Figure 6.8a** shows contour map of temperature-dependence of PL spectra reveals the origins of additional spectral fine-structures of M in 1L-$MoSe_2$/$MnPS_3$ vdW heterostructure. The PL spectrum from the line cut of a contour map at 10 K with spectral fitted results is shown in the bottom of **Figure 6.8b**. The spectral fitted results by multiple-Voight functions can well reproduce the experimentally obtained PL spectrum. The spectral fine structures with peak positions of 1.631 (M_1), 1.612 (M_2) and 1.602 eV (M_3) are well resolved for further analysis. **Figure 6.8b** presents the PL spectra from 10 to 60 K from the horizontal line cut of a

contour map in the top of **Figure 6.8a**. All PL peaks show the redshift with increasing temperature owing to the temperature-dependent band gap shift[142], as explained in the previous subsection.

Figure 6.9 illustrates the temperature dependence of integrated PL intensities of low energy (M_1, M_2, and M_3) and trion state (T*). The PL intensities of low energy states M rapidly decrease in comparison of that of T* and vanish at temperatures higher than ~ 60 K. The strong quenching of PL intensities with elevating temperature in the low energy emissions suggests the thermal disassociation of excitonic bound states associated with assist of thermal excitation by phonons[172,173].

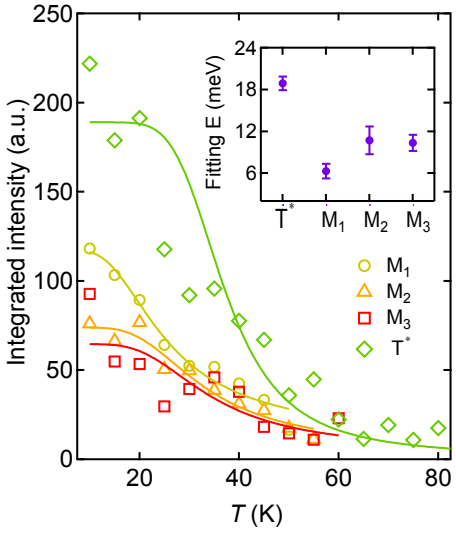

Figure 6.9. The integrated PL intensities as a function of temperature. The solid curves are fitted by **Eq. (6.4)**. The inset shows the fitted parameter of activation energy (E).

The temperature-dependence of integrated intensities with the thermal excitation process (Arrhenius-type) are used to explain the experimental results, which is derived from the rate equation as following:

$$\frac{dN}{dt} = G - \gamma_{\mathrm{rad}}N - \gamma_{\mathrm{nrad}}N, \tag{6.2}$$

where G is the generation rate of trapped excitons (trions), γ_{rad} and γ_{nrad} represent decay rate of radiative and non-radiative recombination of trapped excitons (trions), respectively. The non-radiative recombination could be mainly from trapped excitons detrapping from the potentials. Therefore, the non-radiative decay rate is

expressed as:

$$\gamma_{\mathrm{nrad}} = \gamma_0 \exp\left(-\frac{E}{k_{\mathrm{B}}T}\right), \tag{6.3}$$

where γ_0 is a rate constant and E is the thermal activation energy, corresponding the potential depth. Under steady condition of **Eq. (6.2)**, the PL intensity I can be expressed as:

$$I = I(0)\gamma_{\mathrm{rad}}N = I(0)\frac{G}{\left\{1+\frac{\gamma_0}{\gamma_{\mathrm{rad}}}\exp(-\frac{E}{k_{\mathrm{B}}T})\right\}}, \tag{6.4}$$

where $I(0)$ is the PL intensity at the lowest temperature limit. The $\frac{\gamma_0}{\gamma_{\mathrm{rad}}}$ corresponds to the factor (A).

The experimental results are well fitted by **Eq. (6.4)** as shown in the solid curves of **Figure 6.9**. The inset of **Figure 6.9** summarizes the obtained values of activation energies of excitonic bound states from the fitting procedures. T* is assigned as free excitonic state same as T of 1L-$MoSe_2$ by comparing their binding energy and lifetime as shown in **Figure 6.8** and **Figure 6.21**, respectively. The activation energy of T* is calculated to be 18.9±1 meV, which is also close to the calculated binding energy of 1L-$MoSe_2$ that extracted from the difference between exciton (X) and trion peak (T) in the PL spectrum in **Figure 6.8a**. The derived activation energies of M_1, M_2, and M_3 are 6.3±1, 10.7±2, and 10.4±1 meV, respectively. The error bar here is from fitting process. The smaller activation energies are consistent with faster quenching of PL intensities than that of trions with elevating the temperature. The values of activation energies of lower energy states are comparable to the moiré potential depths of 9–12 meV for intralayer moiré excitonic states in semiconducting heterostructures[174,175], suggesting that these additional peaks are from moiré potential trapped intralayer excitonic states. Moreover, the derived activation energies of M peaks are almost consistent with the energy difference between trion states (T*), rather than exciton (X*), suggesting these M peaks are much more likely to be moiré trions.

The inset of **Figure 6.9** shows the activation energies of T*, M_1, M_2, and M_3. The moiré trapped state at higher energy (M_1) has a smaller moiré potential confinement

energy than M_2 and M_3, because M_1 can be delocalized more easily from the moiré potentials by thermally assisted process. The pre-factor of A in **Eq. (6.4)** corresponds to $\frac{\gamma_0}{\gamma_{rad}}$. The fitted A value of T* (487) shows one-order larger than those of M_1 (13), M_2 (33), and M_3 (31), which indicates T* has a faster nonradiative recombination process[13], while M_1, M_2, and M_3 states are well confined in the minima of moiré potentials. These are consistent with the results in the previously reported intralayer moiré excitons[23,173], implying that the additional peaks come from the confined states by moiré potentials.

6.4.3. Power dependence of PL spectra

The excitation power dependence of PL spectroscopy provides an effective method to further confirm the existence of moiré potential confinement of intralayer trions in the $MoSe_2/MnPS_3$ heterostructure[30,176]. **Figure 6.10a** shows the normalized PL spectra at various power densities at 10 K. The PL spectrum at relatively lower excitation power density of ~340 W/cm^2 shows that the intralayer moiré excitonic peaks (M_1, M_2, and M_3) dominate in the spectrum, however, trion (T*) and exciton (X*) peaks gradually gain the weight in the spectrum, as the power density increased from 1.1 to 16 kW/cm^2 as shown in **Figure 6.11**.

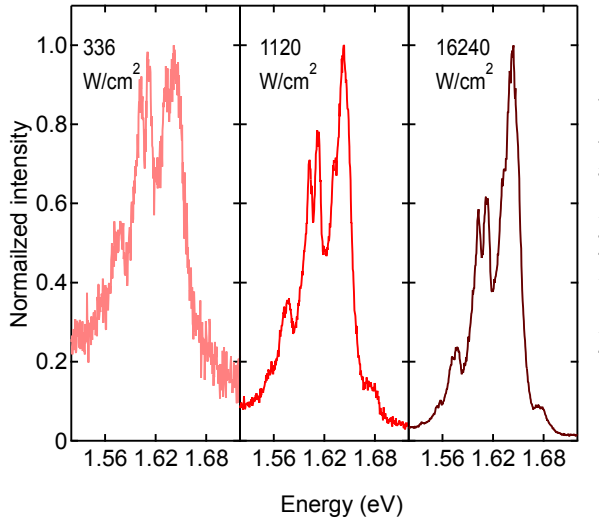

Figure 6.10. (a) Normalized PL spectra at various excitation power densities.

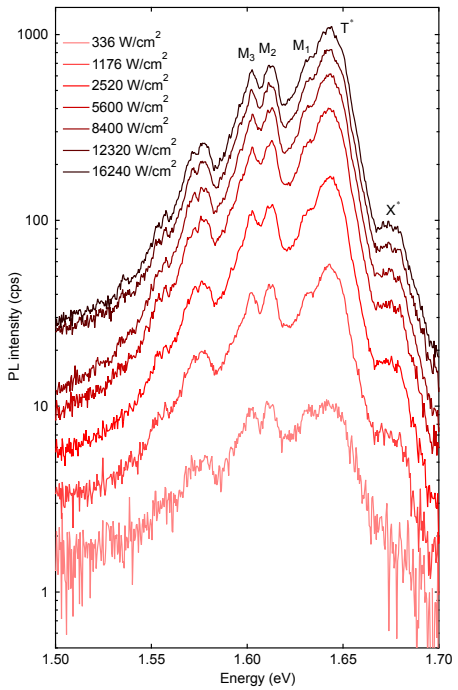

Figure 6.11. PL spectra under various excitation power densities at 10 K.

Figure 6.12 shows integrated PL intensities of M_1, M_2, and M_3 as a function of excitation power density. The inset shows the power density dependent integrated PL intensities of T* and X*. The saturation of PL intensities of M_1, M_2, and M_3 indicates that the number density of excitonic states confined in the moiré potential are quantitatively estimated from the photoexcited electron-hole pair density as follow:

The excited exciton density is calculated using the following equation[177]:

$$\frac{dN}{dt} = g - \frac{N}{\tau_{\mathrm{nrad}}} - \frac{N}{\tau_{\mathrm{rad}}}, \tag{6.5}$$

$$g = \frac{(1-R)\alpha d P}{E_{\mathrm{photon}}}, \tag{6.6}$$

where N is the excited density, g is the generation rate of exciton, τ_{nrad} and τ_{rad} represent non-radiative and radiative lifetime, respectively, R is the reflectivity of 0.05[178], $\alpha = \sim 4 \times 10^5\ \mathrm{cm}^{-1}$ is absorption coefficient[53], d is the thickness of 1L-$MoSe_2$ with a value of 0.7 nm, P is the excitation power density, E_{photon} is the photon energy that equals 1.94 eV.

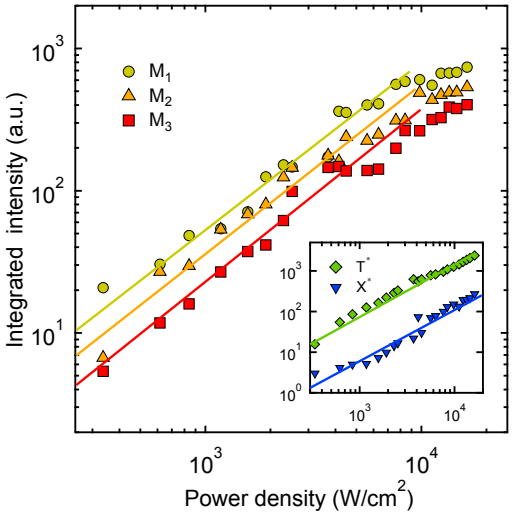

Figure 6.12. Integrated PL intensities of M_1, M_2, and M_3 as a function of excitation power density. The inset shows the power density dependent integrated PL intensities of T* and X*.

I can obtain the exciton density *N* using **Eq. (6.5)** and **Eq. (6.6)** under steady state condition as following:

$$N = \left(\frac{1}{\tau_{\mathrm{nrad}}} + \frac{1}{\tau_{\mathrm{rad}}}\right)^{-1} \times \frac{(1-R)\alpha dP}{E_{\mathrm{photon}}}. \tag{6.7}$$

The term of $\frac{1}{\tau_{\mathrm{nrad}}} + \frac{1}{\tau_{\mathrm{rad}}}$ can be measured experimentally from decay time τ_{decay}, which is defined as $\frac{1}{\tau_{\mathrm{decay}}} = \frac{1}{\tau_{\mathrm{nrad}}} + \frac{1}{\tau_{\mathrm{rad}}}$. The decay time is evaluated as 130 ps from time-resolved PL measurements, which will be discussed later. The exciton density was estimated to be ~1.1×10^{11} cm^{-2}, when PL intensities of moiré excitons tend to be saturated under a power density of ~10^4 W/cm^{-2}.

The saturation of the PL intensities indicates that the density of the excitonic states confined in the moiré potential can be quantitatively estimated as ~1.1×10^{11} cm^{-2} from the photoexcited electron–hole pair density, which is two orders of magnitude smaller than the density of the calculated moiré potential with a period of 2.3 nm (2.0×10^{14} cm^{-2}). This result also strongly suggests that these excitonic states with low-energy emissions (M: M_1, M_2, and M_3) come from the intralayer moiré trions rather than moiré excitons. Moreover, these magnon coupled excitonic states would be localized to form

the moiré trion-magnon complex, as depicted in **Figure 6.13**.

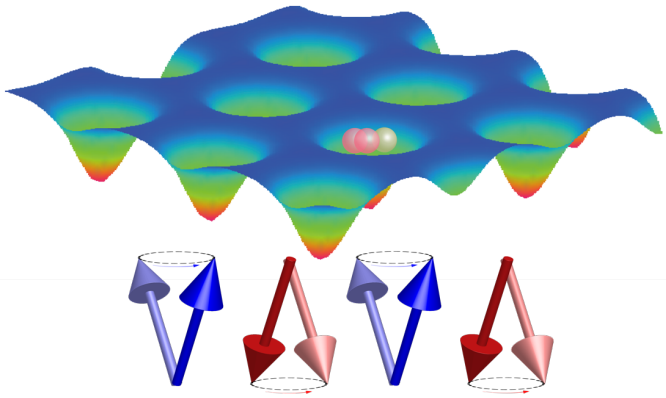

Figure 6.13. Illustration of intralayer trion trapped in moiré potentials, which is coupled with magnon in antiferromagnetic $MnPS_3$ (moiré trion-magnon complex).

6.4.4. Linearly polarized PL spectra

The polarization dependence of PL spectroscopy was performed to investigate the symmetry of moiré trion-magnon complex. I will discuss the results of polarization dependence of PL spectroscopy measurements in this section.

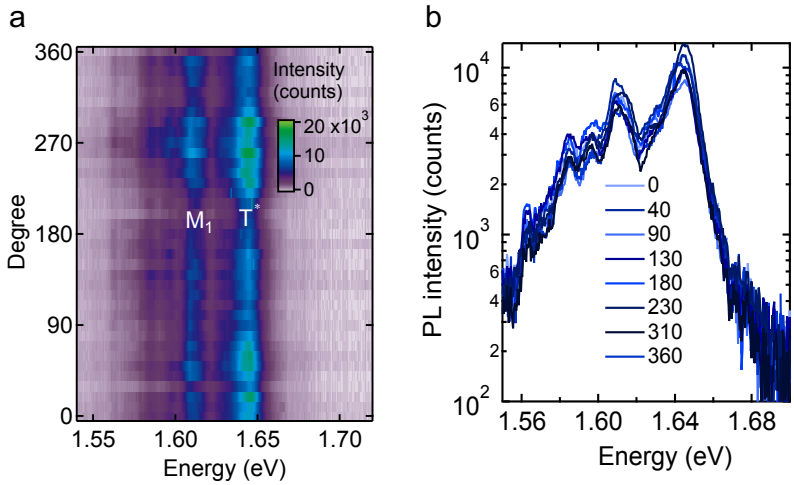

Figure 6.14 (a) Contour map of PL spectra at 10 K in 1L-$MoSe_2$/$MnPS_3$, as a function of detection angle via rotating the linear polarizer. (b) Typical PL spectra with various rotation angle of linear polarizer at detection side.

Figure 6.14a shows the contour map of PL spectra as a function of detection angle via rotating the linear polarizer. The PL spectra with different detection angles do not show significant differences (**Figure 6.14b**). **Figure 6.15a-c** show the polar plot of PL

intensity of M_1, M_2 and T* as a function of detection angle, respectively. The polar plot shows almost isotropic circular pattern. The degree of linear polarization (P_L) is defined as $P_L=(I_{max}-I_{min})/(I_{max}+I_{min})$, where I_{max} (I_{min}) is the maximum (minimum) PL emission intensity. The calculated value of P_L shows small values of 18, 15, and 14% in M_1, M_2 and T*, respectively.

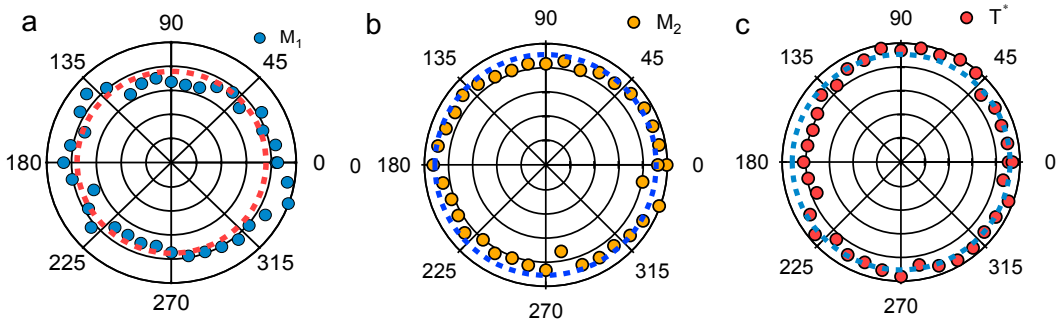

Figure 6.15 Polar plot of normalized PL intensity of M1 (a), M2 (b), and T* (c) at 10 K with various rotation angle of linear polarizer at detection side.

Figure 6.16a shows the PL spectra with various rotation angle of linear polarizer at excitation side. The PL spectra with different excitation angles do not show significant differences as well. The degree of linear polarizations of T*, M_1, and M_2 are 10, 16, and 12%, respectively.

Compared with other strained heterostructures with higher linear polarization value reaching up to 89%[179], these small linear polarizations (**Figure 6.15** and **6.16**) are unlikely caused by strain, which suggests that intralayer moiré trion-magnon complex in 1L-$MoSe_2$/$MnPS_3$ vdW heterostructure well keeps the characteristic of C_3 symmetry.

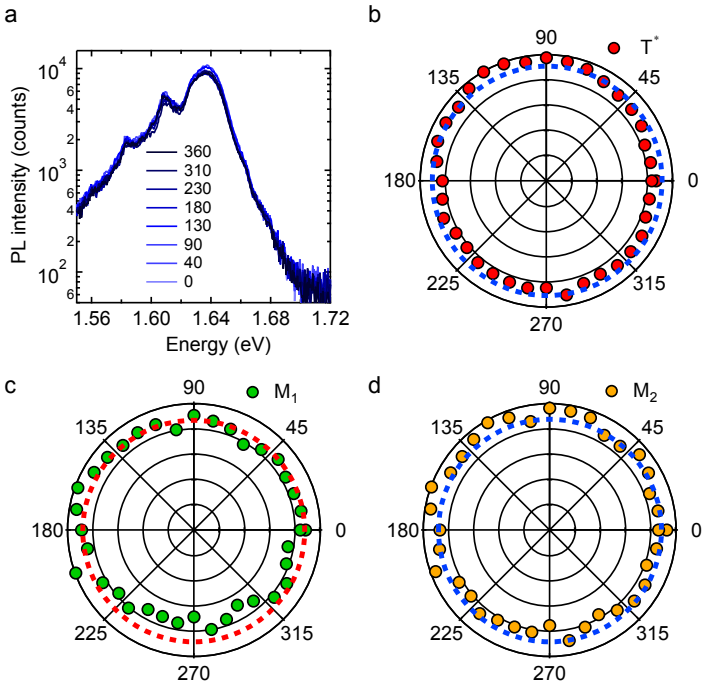

Figure 6.16. (a) PL spectra with various rotation angle of linear polarizer at excitation side. Polar plot of PL intensity at 10 K of T*. (b), M_1 (c) and M_2 (d), as a function of detection angle of linear polarizers.

6.4.5. DFT analysis

I will introduce the results of density functional theory (DFT) by Prof. Okada in Tsukuba University to calculate the moiré potential depths of commensurate stacking of 1L-$MoSe_2$/$MnPS_3$ vdW heterostructure without considering the magnetic spin structure of $MnPS_3$. DFT[180,181] calculations are conducted using the STATE package[182,183]. For the exchange-correlation potential energy among interacting electrons, the generalized gradient approximation was used with the functional forms of Perdew-Burke-Ernzerhof[184]. The dispersive interaction between $MoSe_2$ and $MnPS_3$ layers was treated by vdW-DF2 with the C09 exchange-correlation functional[185,186]. An ultrasoft pseudopotential was used to describe electron-ion interactions[187]. A plane-wave basis set with the cutoff energies of 36 and 324 Ry was adopted to expand the valence wave functions and deficit charge density, respectively. Self-consistent electronic structure calculations were conducted with 2×2×1 *k*-meshes. Structural optimization was performed until the remaining forces on each atom were less than 5

mRy/AA.

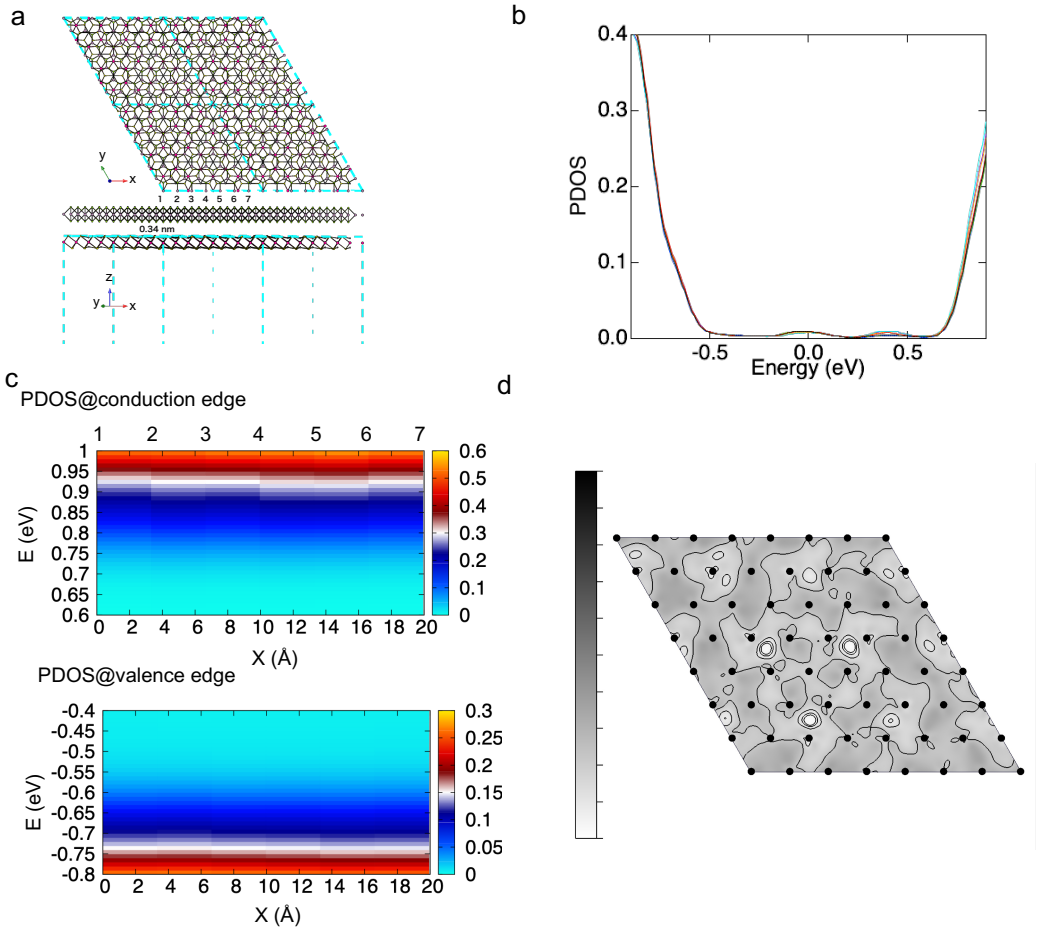

Figure 6.17. (a) Top and side view of atomic structure of $MoSe_2/MnPS_3$ vdW heterostructure. (b) Projected density of states (PDOS) of $MoSe_2/MnPS_3$ vdW heterostructure. (c) Contour map of PDOS of conduction band edge (top) and valence band edge (bottom), where the *x* axis indicates the positions of Mo atoms. (d) Spatial map of electrostatic potential at atom of Mo.

Figure 6.17a shows the schematic of top and side view of atomic structure of 1L-$MoSe_2$ (7×7)/1L-$MnPS_3$ (4×4) stacking with the distance between bilayers of 0.34 nm. The number of 1 to 7 in the figure indicates the position of Mo atom. **Figure 6.17b** shows the projected density of states (PDOS) on Mo atoms of vdW heterostructure. To clarify the relationship of electronic and geometric structure, the contour map of PDOS near conduction band edge and valence band edges of Mo atoms are plotted in **Figure 6.17c**. I clearly observe that the conduction band edges are spatially modulated in a moiré supercell along the zigzag direction of $MoSe_2$ layer, while the valence edge

presents almost identical along one moiré period. The calculated result clearly suggests that the modulation of lowest band gap in 1L-$MoSe_2$ on $MnPS_3$. Moreover, the electrostatic potential at Mo atom is spatially modulated by the $MnPS_3$ (**Figure 6.17d**), which are also consistent with the modulation of band gap in a moiré supercell.

The periodical spatial modulations of electrostatic potentials within a moiré period are clearly observed in the PDOS. Moreover, the calculated potential depth is estimated as 10-20 meV, which also affects the potential modulation for excitonic states. As discussed above, both experimental and theoretical results strongly suggest that these additional peaks are arising from intralayer exitonic states localized in moiré potentials.

6.4.6. Circularly polarized PL spectra under magnetic field

The polarization of excitation light using He-Ne laser (1.96 eV) was controlled by a quarter-wave (λ/4) plate, and σ^+ and σ^- components of polarization dependent PL spectra were detected. The magnetic field from −7 to 7 T was applied perpendicular to samples. **Figure 6.18a** shows circularly polarized PL spectra at various magnetic fields (-7, 0, and 7 T) at 10 K. The PL spectra are resolved with σ^+ and σ^- components, corresponding to the signals from K+ and K– valley, respectively. The spectra shown here are different from the one in **Figure 6.4** due to spatial inhomogeneity of vdW heterostructure (**Figure 6.19**). The spatial inhomogeneity is also observed in previously reported results in TMD bilayer heterostructures[30,158].

The σ^+ and σ^- components of T* are almost identical without magnetic field in 1L-$MoSe_2$/$MnPS_3$ vdW heterostructure, which is consistent with the previously reported results in 1L-$MoSe_2$[69,102,128], while intralayer moiré excitons show slightly difference between PL intensity of σ^+ and σ^- components. The degree of valley polarization of T* and M_1 under 0 T were calculated to be 2 and 11%, respectively. **Figure 6.18b** shows magnetic field dependent Zeeman splitting (ΔE) of T* and M_1, where the Zeeman splitting is defined as the peak energy difference of σ^+ and σ^- components. Both the Zeeman splitting (ΔE) in T* and M_1 present a linear change with increasing the magnetic field from -7 to 7 T, as shown in the solid line in **Figure 6.18b**. The slope of

the Zeeman splitting in T* is estimated to be 0.28±0.01 meV/T, which is consistent with that of T in 1L-$MoSe_2$[69]. Noted that that the slope of Zeeman splitting in M_1 (0.24±0.01 meV/T) shows the similar value in T*. Thus, the calculated g factor of T* and M_1 are evaluated as to be 4.8 and 4.1, respectively. The g factor is given by the relationship as $\Delta E = g\mu_B$, where μ_B is the Bohr magneton.

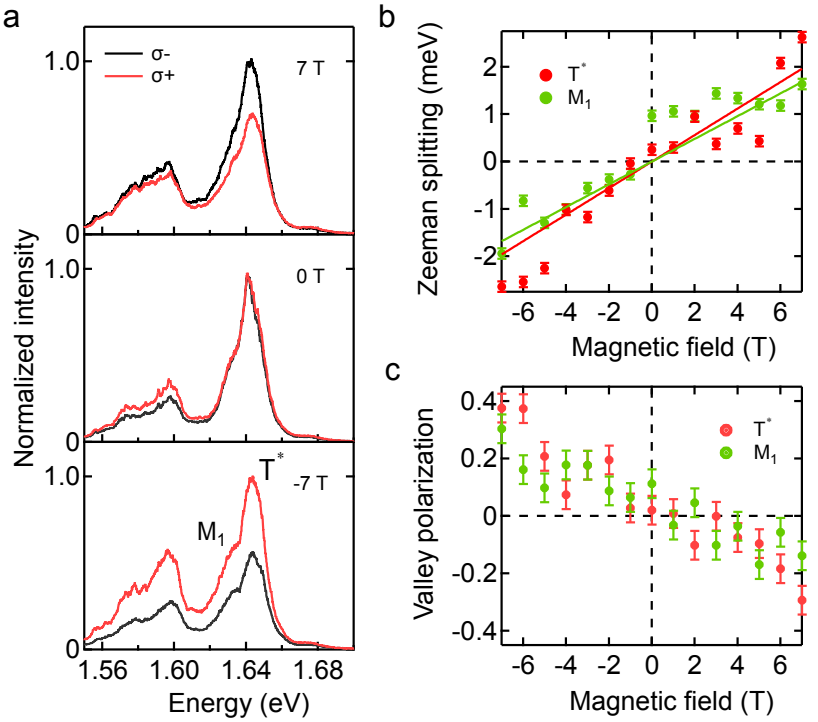

Figure 6.18. (a) PL spectrum of σ- component in 1L-$MoSe_2$/$MnPS_3$ vdW heterostructure at -7, 0, and 7 T. (b) Valley polarization of T* and M_1 as a function of magnetic field from -7 to 7 T. (c) Magnetic field dependent Zeeman splitting of T* and M_1.

I further plot the valley polarization of T* and M_1 as a function of magnetic field from -7 to 7 T in **Figure 6.18c**. The valley polarizations of T* and M_1 show a linear increase and almost identical with a linear change as a function of magnetic fields. The g factor and valley polarization of intralayer moiré trion-magnon complex are contrast to interlayer moiré excitons (trions), which can be caused by the well-kept rotational symmetry C_3 of transitions in the intralayer excitons (trions)[23].

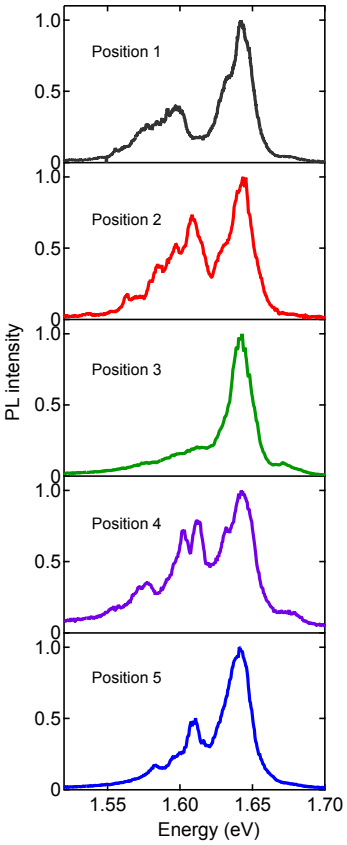

Figure 6.19. PL spectra measured at 5 different positions in the same 1L-$MoSe_2$/$MnPS_3$ vdW heterostructure at 10 K.

6.5. Dynamics of moiré trion-magnon complex; Lifetime and coherence time

I determined the lifetimes of intralayer moiré trion-magnon complex using time-resolved PL spectroscopy with the combination of TCSPC and Michelson interferometric technique under a pulsed supercontinuum laser light in this section. **Figure 6.20a** shows the time-resolved PL spectral map of 1L-$MoSe_2$/$MnPS_3$ vdW heterostructure as a function of photon energy and time under a low excitation power condition. The PL signals at around 1.666, 1.643, and 1.664 eV are assigned as emissions from X*, T* and M_1, respectively, according to **Figure 6.20b**.

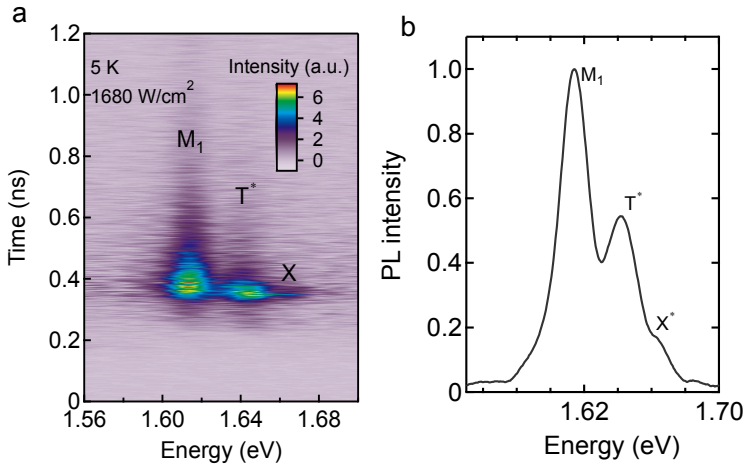

Figure 6.20. (a) Transient PL intensity map of 1L-$MoSe_2$/$MnPS_3$ vdW heterostructure as a function of emission energy (*x* axis) and decay time (*y* axis) at 5 K at excitation power density of 1680 W/cm^2 in the linear power condition. (b) Normalized PL intensity obtained from **Figure 6.20a** by integrating the map along the horizontal direction, in which the energy resolution is 0.6 meV.

Figure 6.21a displays the PL decays of moiré trion-magnon complex (M_1), extracted along the vertical direction at the peak position of M_1 from **Figure 6.20a**. The instrumental response function (IRF) is also shown in the figure. The solid blue curve is fitted results of M_1, using the convolution procedure with IRF and double-exponential function as $I = A_1 \exp(-t/\tau_1) + A_2 \exp(-t/\tau_2)$ [103,106], where $A_{1(2)}$ and $\tau_{1(2)}$ are coefficients and decay times, respectively. The fitted results are well consistent with the experimental PL decay curves. The mean lifetime can be estimated as $\langle\tau\rangle = (A_1\tau_1 + A_2\tau_2)/(A_1 + A_2)$. The decay times of X* and T* were ~15 ps and ~ 70 ps (**Figure 6.21b, c**), respectively. These lifetimes are similar to previously reported results in 1L-$MoSe_2$[107]. In contrast, the mean lifetime of moiré trion-magnon complex (M_1) of ~ 130 ps is much longer than those of exciton (X*) and trion (T*). The defects bound exitonic states are also excluded because they have much longer lifetime reaching up to 200 ns as reported in 1L-WSe_2[188]. Therefore, it also proves that these states with lifetime of ~100 ps derive from intralayer excitonic states that tapped by moiré potentials rather than defects.

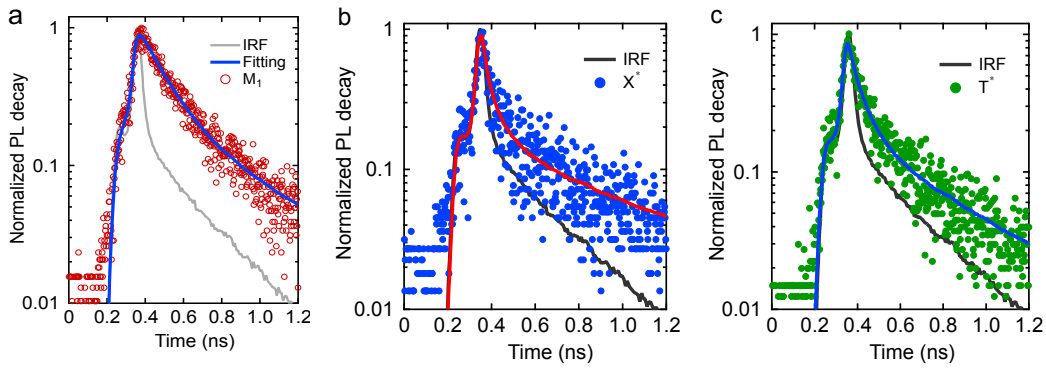

Figure 6.21. Normalized PL decay profiles of (a) M_1, (b) X*, and (c) T* as a function of decay time, extracted from PL intensity map. The instrumental response function (IRF) is also shown in the grey or black curve.

The further information of excitonic coherence provides more important evidence to distinguish free and moiré trapped excitonic states[30,158,189,190]. The coherent correlation spectroscopy with a Michelson interferometer is applied to record the first order correlation function $g^{(1)}(\tau)$, as previously demonstrated in quantum dots and carbon nanotube[191,192]. **Figure 6.22a** shows the interferogram of PL intensity monitored at emission of M_1 at 5 K under a low excitation power density of 560 W/cm^2. The fringes with very high value of visibilities of M_1 reach up to 99% and envelop of fringes is clearly observed.

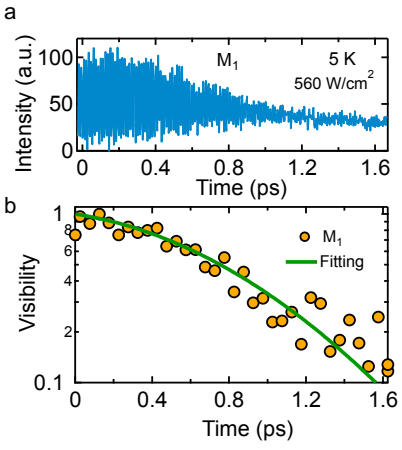

Figure 6.22. (a) Temporal interferogram of M_1 at 5 K under 560 W/cm^2. (b) Visibility of M_1. The solid curves are given by the product of exponential and Gaussian function.

Figure 6.22b shows fringe visibilities $V(\tau)$ of M_1 (red dots) as a function of delay

time (τ) evaluated from **Figure 6.22a**. The $V(\tau)$ was estimated using the relationship as $V(\tau) = (I_{\max}(\tau) - I_{\min}(\tau))/(I_{\max}(\tau) + I_{\min}(\tau))$, where $I_{\max}(\tau)$ and $I_{\min}(\tau)$ are the maxima and minima of fringes at various delay times. The decay curve of fringe visibilities for M_1 is well fitted with a product of an exponential and a Gaussian function as $f(\tau) = e^{-B_1\tau}e^{-{B_2}^2\tau^2}$, as shown in green solid curve in **Figure 6.22d**[193]. The Lorentzian and Gaussian components in a spectral full width at half maximum (FWHM), corresponding to homogeneous and inhomogeneous spectral broadening are therefore described as $2\hbar B_1$ and $4\hbar\sqrt{\ln 2}B_2$, where $\hbar$ is the Plank constant divided by 2π. The fitting parameters of B_1 and B_2 for M_1 are 0.4 and 0.83 ps^{-1}, respectively. The fitting parameters of B_1 and B_2 for are T* are 1.44 and 1.2 ps^{-1}, respectively.

I could estimate the coherence time T_2 of M_1 as 2.5 ps. T_2 of T* was also estimated to be 0.69 ps (**Figure 6.23a, b**), which is consistent with the previous result[143]. The experimentally obtained T_1 from PL decay curve is much longer than T_2. The pure dephasing time T_2^* of moiré trion-magnon complex (M_1) is evaluated as ~2.5 ps using **Eq. (3.1)**, which is about threefold longer than that of trion (T*).

The longer pure dephasing time (narrower homogeneous linewidth) of moiré-trion-magnon complex caused by the confinement in moiré potentials, are less prone to scattering of phonons. These results in the time-domain are also consistent with the PL spectral analysis using multiple-Voigt functions. The fitting linewidths of Gaussian and Lorentzian components of T* (M_1) are 7.9 (7.4) and 5.2 (1.3) meV, respectively. Spectral linewidths of M peaks from moiré-trion-magnon complex are much sharper than those of trion coupled with a magnon (T*).

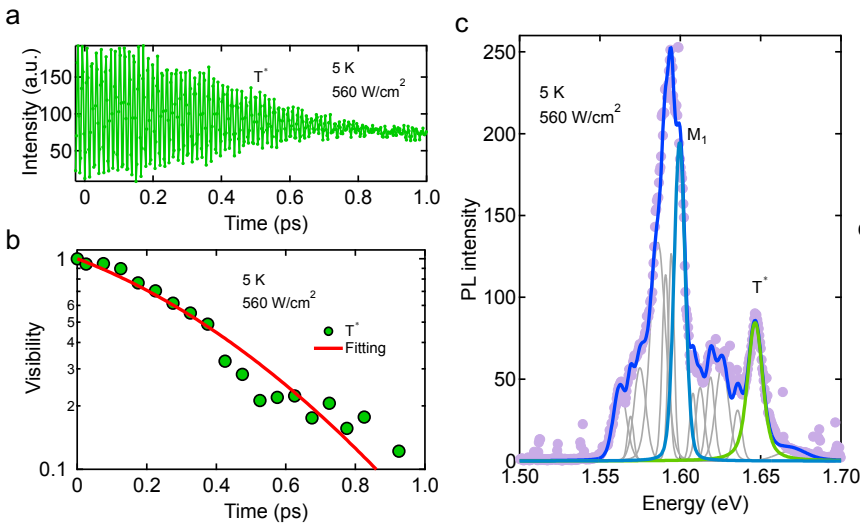

Figure 6.23. (a) Temporal interferogram of T* at 5 K under 560 W/cm^2. (b) Calculated visibility of T* under 560 W/cm^2. The solid curves are given by the product of an exponential and a Gaussian function. (c) PL spectrum at 5 K under the excitation power density of 560 W/cm^2. The blue curve is a spectral fitting results by multiple-Voight functions.

Moreover, the coherence time of both M_1 and T* is shorter under higher excitation power condition, which is less than saturation power density, as shown in **Figure 6.24**. The obtained parameters of B_1 and B_2 for are T*(M_1) are 2.9 (0.5) and 1.2 (1.1) ps^{-1}. The coherence time of T* and M_1 are 0.34 and 2 ps, respectively. This behavior obeys the homogeneous broadening under higher excitation power condition.

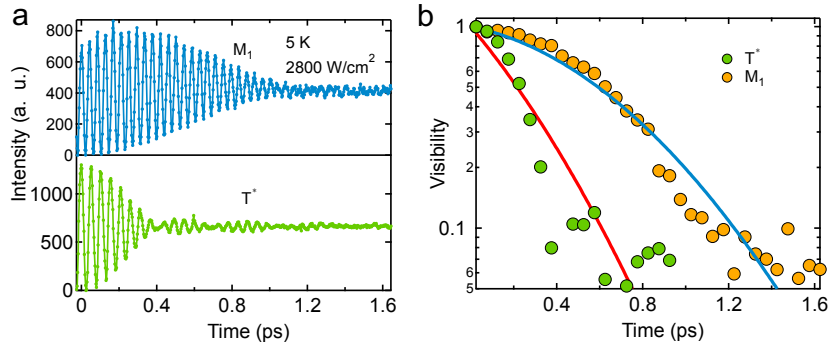

Figure 6.24. (a) Temporal interferogram of M_1 (blue line) and T* (green line) at 5 K under 2.8 kW/cm^2. (b) Calculated visibility of M_1 (yellow dots) and T* (green dots) from the interferograms under 2.8 kW/cm^2. The solid curves are given by the product of an exponential and a Gaussian function.

6.6. Chapter summary

I have demonstrated the emergence of intralayer trions localized in the moiré potentials formed by twisted monolayer $MoSe_2$ and antiferromagnetic $MnPS_3$ vdW heterostructure in this work. I carefully investigated the low-temperature PL spectra of $MoSe_2/MnPS_3$ vdW heterostructure with additional fine spectral structures at low energy side of coupled magnon-trion peaks under Néel temperature. The fine spectral structures with longer lifetime and coherence time are assigned as localized intralayer magnon-trion complex in the moiré potentials (moiré magnon-trion complex), which makes the moiré excitons different from those frequently observed in bilayer semiconducting TMD heterostructure, implying the appearance of magnetic moiré excitonic states. I thus foresee that novel vdW heterostructure with combination of monolayer semiconductor TMD and antiferromagnetic $TMPX_3$ emerges the magnetic moiré excitonic states. The precise energies and light emission intensities of these magentic moiré-excitonic states can be tuned and controlled by applying external magnetic fields. Therefore, these states also provide a good platform toward for future application of quantum emitters with magnetic functionalities.

Chapter 7. Conclusion and outlook

In this thesis, I have studied the novel optical properties of excitonic states (excitons, and trions) in 1L-TMDs and magnetic artificial vdW heterostructures using advanced optical spectroscopy. In this chapter, I will summarize the obtained main results and discuss the outlook based on this study.

In **Chapter 4**, I systematically studied the dynamics of excitonic valley polarization 1L-$MoSe_2$ encapsulated by *h*-BN, using polarization- and time-resolved PL spectroscopy. I found that the excitonic valley polarization under magnetic field is caused by the asymmetry of valley scattering of excitons and trions between K+ and K– valley. Moreover, extremely long trions inter-valley relaxation time up to few nanoseconds was obtained at 10 K under 7 T. These results indicate new physical understandings for valley polarization dynamics of excitonic states under magnetic field and provide guidance towards long-time keeping and easy controlling of valley polarization.

In **Chapter 5**, I designed a novel interface between 1L-$MoSe_2$ and a strongly correlated electron system of double-layered perovskite Mn oxide inserting multiple layers *h*-BN spacer (1L-$MoSe_2$/*h*-BN/Mn oxide vdW heterostructure), where the Mn oxide shows the phase transition from paramagnetic insulator to ferromagnetic metal at 80 K via the double-exchange interaction. A phase transition material is introduced into a van der Waals heterostructure for the first time. I observed the drastic and discontinuous change of the temperature dependent PL spectra of excitons, caused by the dielectric screening effect and efficient charge transfer below phase transition temperature. In addition, the nonlinear and enhanced valley splitting and polarization of 1L-$MoSe_2$ on the ferromagnetic-metal with *h*-BN spacer have been revealed in comparison with those in 1L-$MoSe_2$. Experimentally, a large effective magnetic field reaching over 7 T is obtained in the vdW heterostructure with the bilayer *h*-BN. A larger effective magnetic field of over 15 T is predicted in the 1L-$MoSe_2$/*h*-BN/Mn oxide using a thinner *h*-BN monolayer. Noted that it is the first time to lift the valley

degeneracy via magnetic proximity effect by a ferromagnetic metal. With inserting thin layer spacer, other ferromagnetic metal choice like Ni and Co might be used for lifting valley degeneracy. Moreover, I revealed the characteristic length scale of a few nanometers in the magnetic proximity effect and charge transfer. This study would inspire new strategies to modulate excitonic states using dielectric screening, charge carriers, and magnetic spins of 1L-TMDs by introducing novel substrate underneath.

In **Chapter 6**, I have demonstrated a moiré excitonic system interacting with the magnetic elementary excitation of an antiferromagnetic order in a vdW heterostructure of 1L-$MoSe_2$/$MnPS_3$. I found that the fine spectral peaks in the low-temperature PL spectra on the low-energy side of the exciton and trion peaks below Néel temperature. Both experimental and theoretical results suggest that these fine spectral peaks come from intralayer trion–magnon complexes trapped in the moiré potentials (moiré trion–magn on complexes). Moreover, these moiré trion–magnon complexes well keep the C_3 symmetry with long lifetime and coherence time at cryogenic temperature. The coherence time of moiré trion–magnon complexes is much longer than that of conventional excitons and trions in 1L-TMDs. An additional prospective experiment is the investigation of the impact of charging effects on magnon coupled moiré complex because carrier number trapped in moiré potential can be modulated by electronic doping. The discovery of novel magnon coupled moiré trion complex is beneficial for the applications of quantum states and paves a new way for the exploration of novel quantum phenomena in moiré excitonic systems with magnetic functionalities.

The investigations of optical properties of semiconducting monolayer TMD and its magnetic vdW heterostructures studied here could be significant for fundamental understanding exciton and valley physics. However, it is still challenging to turn these fundamental studies into viable technologies for spin- and valley-tronics. One of challenges is to realize large valley polarization with long time keeping at room temperature. This thesis reveals one way that is using magnetic proximity effect to lift valley degeneracy even without applying any-external magnetic fields, which is very significant to reduce the energy consumption, because the additional is needed for

generation of higher magnetic field using superconducting magnet and permanent magnet. Moreover, the discovery of novel quasi-particles (magnon-coupled moiré trion) with long lifetime in heterostructures enables to use the switching and control of quantum light emission in future application. Another task is that almost systems studied here are fabricated by mechanically exfoliated and then assembled using transfer method. This also limits the actual and industrial application because of requirement of large-scale devices. The improvements of fabrication and assembly in terms of quality and large-scale are expected in the future.

Noted that the discovery of a new material, quasi-particle, and physical phenomenon will enable new products and technologies. I strongly hope that this study on novel optical physics of excitonic states in unprecedented material systems could pave the way to the potential applications for the future.

References

[1] B. Dubertret, T. Heine, M. Terrones, *Acc. Chem. Res.* **2015**, *48*, 1.

[2] J. M. Raimond, M. Brune, Q. Computation, F. De Martini, C. Monroe, **2004**, *306*, 666.

[3] S. Manzeli, D. Ovchinnikov, D. Pasquier, O. V. Yazyev, A. Kis, *Nat. Rev. Mater.* **2017**, *2*, 17033.

[4] N. Mounet, M. Gibertini, P. Schwaller, D. Campi, A. Merkys, A. Marrazzo, T. Sohier, I. E. Castelli, A. Cepellotti, G. Pizzi, N. Marzari, *Nat. Nanotechnol.* **2018**, *13*, 246.

[5] D. Geng, H. Y. Yang, *Adv. Mater.* **2018**, *30*, 1800865.

[6] G. Wang, A. Chernikov, M. M. Glazov, T. F. Heinz, X. Marie, T. Amand, B. Urbaszek, *Rev. Mod. Phys.* **2018**, *90*, 021001.

[7] M. Onga, Y. Zhang, T. Ideue, Y. Iwasa, *Nat. Mater.* **2017**, *16*, 1193.

[8] L. Yang, Q. Fu, W. Wang, J. Huang, J. Huang, J. Zhang, B. Xiang, *Nanoscale* **2015**, *7*, 10490.

[9] R. G. Dickinson, L. Pauling, *J. Am. Chem. Soc.* **1923**, *45*, 1466.

[10] J. A. Wilson, A. D. Yoffe, *Adv. Phys.* **1969**, *18*, 193.

[11] *Proc. R. Soc. London. Ser. A. Math. Phys. Sci.* **1963**, *273*, 69.

[12] M. Chhowalla, H. S. Shin, G. Eda, L. J. Li, K. P. Loh, H. Zhang, *Nat. Chem.* **2013**, *5*, 263.

[13] G. Moody, J. Schaibley, X. Xu, *J. Opt. Soc. Am. B* **2016**, *33*, C39.

[14] G. Yang, J. Li, H. Ma, Y. Yang, C. Li, X. Mao, F. Yin, *Phys. Rev. B* **2018**, *98*, 235419.

[15] Y. Lin, X. Ling, L. Yu, S. Huang, A. L. Hsu, Y.-H. Lee, J. Kong, M. S. Dresselhaus, T. Palacios, *Nano Lett.* **2014**, *14*, 5569.

[16] M. Grzeszczyk, M. R. Molas, K. Nogajewski, M. Bartoš, A. Bogucki, C. Faugeras, P. Kossacki, A. Babiński, M. Potemski, *Sci. Rep.* **2020**, *10*, 4981.

[17] Y. Li, Z. Qi, M. Liu, Y. Wang, X. Cheng, G. Zhang, L. Sheng, *Nanoscale* **2014**, *6*, 15248.

[18] T. Cao, G. Wang, W. Han, H. Ye, C. Zhu, J. Shi, Q. Niu, P. Tan, E. Wang, B. Liu, J. Feng, *Nat. Commun.* **2012**, *3*, 885.

[19] K. F. Mak, D. Xiao, J. Shan, *Nat. Photonics* **2018**, *12*, 451.

[20] J. R. Schaibley, H. Yu, G. Clark, P. Rivera, J. S. Ross, K. L. Seyler, W. Yao, X.

Xu, *Nat. Rev. Mater.* **2016**, *1*, 16055.

[21] K. S. Novoselov, A. Mishchenko, A. Carvalho, A. H. Castro Neto, *Science* **2016**, *353*, 1.

[22] X. Wang, J. Zhu, K. L. Seyler, P. Rivera, H. Zheng, Y. Wang, M. He, T. Taniguchi, K. Watanabe, J. Yan, D. G. Mandrus, D. R. Gamelin, W. Yao, X. Xu, *Nat. Nanotechnol.* **2021**, *16*, 1208.

[23] N. Zhang, A. Surrente, M. Baranowski, D. K. Maude, P. Gant, A. Castellanos-Gomez, P. Plochocka, *Nano Lett.* **2018**, *18*, 7651.

[24] F. Cadiz, E. Courtade, C. Robert, G. Wang, Y. Shen, H. Cai, T. Taniguchi, K. Watanabe, H. Carrere, D. Lagarde, M. Manca, T. Amand, P. Renucci, S. Tongay, X. Marie, B. Urbaszek, *Phys. Rev. X* **2017**, *7*, 021026.

[25] T. Norden, C. Zhao, P. Zhang, R. Sabirianov, A. Petrou, H. Zeng, *Nat. Commun.* **2019**, *10*, 4163.

[26] P. Wei, S. Lee, F. Lemaitre, L. Pinel, D. Cutaia, W. Cha, F. Katmis, Y. Zhu, D. Heiman, J. Hone, J. S. Moodera, C.-T. Chen, *Nat. Mater.* **2016**, *15*, 711.

[27] C. Zhao, T. Norden, P. Zhang, P. Zhao, Y. Cheng, F. Sun, J. P. Parry, P. Taheri, J. Wang, Y. Yang, T. Scrace, K. Kang, S. Yang, G. X. Miao, R. Sabirianov, G. Kioseoglou, W. Huang, A. Petrou, H. Zeng, *Nat. Nanotechnol.* **2017**, *12*, 757.

[28] K. L. Seyler, D. Zhong, B. Huang, X. Linpeng, N. P. Wilson, T. Taniguchi, K. Watanabe, W. Yao, D. Xiao, M. A. McGuire, K.-M. C. Fu, X. Xu, *Nano Lett.* **2018**, *18*, 3823.

[29] C. Jin, E. C. Regan, A. Yan, M. Iqbal Bakti Utama, D. Wang, S. Zhao, Y. Qin, S. Yang, Z. Zheng, S. Shi, K. Watanabe, T. Taniguchi, S. Tongay, A. Zettl, F. Wang, *Nature* **2019**, *567*, 76.

[30] K. L. Seyler, P. Rivera, H. Yu, N. P. Wilson, E. L. Ray, D. G. Mandrus, J. Yan, W. Yao, X. Xu, *Nature* **2019**, *567*, 66.

[31] S. Miao, T. Wang, X. Huang, D. Chen, Z. Lian, C. Wang, M. Blei, T. Taniguchi, K. Watanabe, S. Tongay, Z. Wang, D. Xiao, Y.-T. Cui, S.-F. Shi, *Nat. Commun.* **2021**, *12*, 8.

[32] M. S. Hybertsen, S. G. Louie, *Phys. Rev. B* **1986**, *34*, 5390.

[33] G. Onida, L. Reining, A. Rubio, *Rev. Mod. Phys.* **2002**, *74*, 601.

[34] M. Bernardi, C. Ataca, M. Palummo, J. C. Grossman, *Nanophotonics* **2017**, *6*, 214.

[35] B. Partoens, F. M. Peeters, *Phys. Rev. B* **2006**, *74*, 075404.

[36] A. H. Castro Neto, F. Guinea, N. M. R. Peres, K. S. Novoselov, A. K. Geim, *Rev. Mod. Phys.* **2009**, *81*, 109.

[37] Y. Zhang, T. T. Tang, C. Girit, Z. Hao, M. C. Martin, A. Zettl, M. F. Crommie, Y. R. Shen, F. Wang, *Nature* **2009**, *459*, 820.

[38] M. Bernardi, C. Ataca, M. Palummo, J. C. Grossman, *Nanophotonics* **2017**, *6*, 479.

[39] T. Ohta, A. Bostwick, T. Seyller, K. Horn, E. Rotenberg, *Science* **2006**, *313*, 951.

[40] O. V. Yazyev, A. Kis, *Mater. Today* **2015**, *18*, 20.

[41] A. Splendiani, L. Sun, Y. Zhang, T. Li, J. Kim, C.-Y. Chim, G. Galli, F. Wang, *Nano Lett.* **2010**, *10*, 1271.

[42] K. F. Mak, C. Lee, J. Hone, J. Shan, T. F. Heinz, *Phys. Rev. Lett.* **2010**, *105*, 136805.

[43] Y. Xu, C. Horn, J. Zhu, Y. Tang, L. Ma, L. Li, S. Liu, K. Watanabe, T. Taniguchi, J. C. Hone, J. Shan, K. F. Mak, *Nat. Mater.* **2021**, *20*, 645.

[44] F. Hüser, T. Olsen, K. Thygesen, *Phys. Rev. B* **2013**, *88*, 245309.

[45] S. Latini, T. Olsen, K. S. Thygesen, *Phys. Rev. B* **2015**, *92*, 245123.

[46] B. Baumeier, D. Andrienko, M. Rohlfing, *J. Chem. Theory Comput.* **2012**, *8*, 2790.

[47] X. F. He, *Phys. Rev. B* **1991**, *43*, 2063.

[48] A. Chernikov, T. C. Berkelbach, H. M. Hill, A. Rigosi, Y. Li, O. B. Aslan, D. R. Reichman, M. S. Hybertsen, T. F. Heinz, *Phys. Rev. Lett.* **2014**, *113*, 076802.

[49] A. Raja, A. Chaves, J. Yu, G. Arefe, H. M. Hill, A. F. Rigosi, T. C. Berkelbach, P. Nagler, C. Schüller, T. Korn, C. Nuckolls, J. Hone, L. E. Brus, T. F. Heinz, D. R. Reichman, A. Chernikov, *Nat. Commun.* **2017**, *8*, 15251.

[50] A. Chernikov, T. C. Berkelbach, H. M. Hill, A. Rigosi, Y. Li, O. B. Aslan, D. R. Reichman, M. S. Hybertsen, T. F. Heinz, *Phys. Rev. Lett.* **2014**, *113*, 076802.

[51] W. Zhao, Z. Ghorannevis, L. Chu, M. Toh, C. Kloc, P.-H. Tan, G. Eda, *ACS Nano* **2013**, *7*, 791.

[52] C. Ruppert, O. B. Aslan, T. F. Heinz, *Nano Lett.* **2014**, *14*, 6231.

[53] A. Arora, K. Nogajewski, M. Molas, M. Koperski, M. Potemski, *Nanoscale* **2015**, *7*, 20769.

[54] X.-X. Zhang, Y. You, S. Y. F. Zhao, T. F. Heinz, *Phys. Rev. Lett.* **2015**, *115*, 257403.

[55] O. Gunawan, Y. P. Shkolnikov, K. Vakili, T. Gokmen, E. P. De Poortere, M. Shayegan, *Phys. Rev. Lett.* **2006**, *97*, 186404.

[56] A. Rycerz, J. Tworzydło, C. W. J. Beenakker, *Nat. Phys.* **2007**, *3*, 172.

[57] D. Xiao, G.-B. Liu, W. Feng, X. Xu, W. Yao, *Phys. Rev. Lett.* **2012**, *108*, 196802.

[58] Z. Y. Zhu, Y. C. Cheng, U. Schwingenschlögl, *Phys. Rev. B* **2011**, *84*, 153402.

[59] G.-B. Liu, W.-Y. Shan, Y. Yao, W. Yao, D. Xiao, *Phys. Rev. B* **2013**, *88*, 085433.

[60] Y. Song, H. Dery, *Phys. Rev. Lett.* **2013**, *111*, 026601.

[61] C. J. Ciccarino, T. Christensen, R. Sundararaman, P. Narang, *Nano Lett.* **2018**, *18*, 5709.

[62] G. Aivazian, Z. Gong, A. M. Jones, R. L. Chu, J. Yan, D. G. Mandrus, C. Zhang, D. Cobden, W. Yao, X. Xu, *Nat. Phys.* **2015**, *11*, 148.

[63] X. Xu, W. Yao, D. Xiao, T. F. Heinz, *Nat. Phys.* **2014**, *10*, 343.

[64] A. Srivastava, M. Sidler, A. V. Allain, D. S. Lembke, A. Kis, A. Imamoğlu, *Nat. Phys.* **2015**, *11*, 141.

[65] W. Yao, D. Xiao, Q. Niu, *Phys. Rev. B* **2008**, *77*, 235406.

[66] S. A. Vitale, D. Nezich, J. O. Varghese, P. Kim, N. Gedik, P. Jarillo-Herrero, D. Xiao, M. Rothschild, *Small* **2018**, *14*, 1801483.

[67] K. F. Mak, K. He, J. Shan, T. F. Heinz, *Nat. Nanotechnol.* **2012**, *7*, 494.

[68] H. Zeng, J. Dai, W. Yao, D. Xiao, X. Cui, *Nat. Nanotechnol.* **2012**, *7*, 490.

[69] D. MacNeill, C. Heikes, K. F. Mak, Z. Anderson, A. Kormányos, V. Zólyomi, J. Park, D. C. Ralph, *Phys. Rev. Lett.* **2015**, *114*, 037401.

[70] H. Rostami, A. G. Moghaddam, R. Asgari, *Phys. Rev. B* **2013**, *88*, 085440.

[71] K. S. Novoselov, A. Mishchenko, A. Carvalho, A. H. Castro Neto, *Science.* **2016**, *353*, aac9439.

[72] C. Zhao, T. Norden, P. Zhang, P. Zhao, Y. Cheng, F. Sun, J. P. Parry, P. Taheri, J. Wang, Y. Yang, T. Scrace, K. Kang, S. Yang, G. Miao, R. Sabirianov, G. Kioseoglou, W. Huang, A. Petrou, H. Zeng, *Nat. Nanotechnol.* **2017**, *12*, 757.

[73] D. Zhong, K. L. Seyler, X. Linpeng, R. Cheng, N. Sivadas, B. Huang, E. Schmidgall, T. Taniguchi, K. Watanabe, M. A. McGuire, W. Yao, D. Xiao, K.-M. C. Fu, X. Xu, *Sci. Adv.* **2017**, *3*, e1603113.

[74] J. Kang, S. Tongay, J. Zhou, J. Li, J. Wu, *Appl. Phys. Lett.* **2013**, *102*, 012111.

[75] Y. Liu, C. Zeng, J. Yu, J. Zhong, B. Li, Z. Zhang, Z. Liu, Z. M. Wang, A. Pan, X. Duan, *Chem. Soc. Rev.* **2021**, *50*, 6401.

[76] C. R. Dean, A. F. Young, I. Meric, C. Lee, L. Wang, S. Sorgenfrei, K. Watanabe, T. Taniguchi, P. Kim, K. L. Shepard, J. Hone, *Nat. Nanotechnol.* **2010**, *5*, 722.

[77] M. Kubota, H. Fujioka, K. Hirota, K. Ohoyama, Y. Moritomo, H. Yoshizawa, Y. Endoh, *J. Phys. Soc. Japan* **2000**, *69*, 1606.

[78] L. Wang, I. Meric, P. Y. Huang, Q. Gao, Y. Gao, H. Tran, T. Taniguchi, K. Watanabe, L. M. Campos, D. A. Muller, J. Guo, P. Kim, J. Hone, K. L. Shepard, C. R. Dean, *Science* **2013**, *342*, 614.

[79] Nanophoton corp, "Nanophoton website," can be found under https://www.nanophoton.net/products/ramantouch, **2020**.

[80] "Homepage of NIREOS," can be found under https://www.nireos.com/gemini/#tab-id-4.

[81] K. Shinokita, X. Wang, Y. Miyauchi, K. Watanabe, T. Taniguchi, K. Matsuda, *Adv. Funct. Mater.* **2019**, *29*, 1900260.

[82] H. Yuan, X. Wang, B. Lian, H. Zhang, X. Fang, B. Shen, G. Xu, Y. Xu, S. C. Zhang, H. Y. Hwang, Y. Cui, *Nat. Nanotechnol.* **2014**, *9*, 851.

[83] Y. J. Zhang, T. Oka, R. Suzuki, J. T. Ye, Y. Iwasa, *Science* **2014**, *344*, 725.

[84] F. Liu, J. Zhou, C. Zhu, Z. Liu, *Adv. Funct. Mater.* **2017**, *27*, 1602404.

[85] G. Aivazian, Z. Gong, A. M. Jones, R. L. Chu, J. Yan, D. G. Mandrus, C. Zhang, D. Cobden, W. Yao, X. Xu, *Nat. Phys.* **2015**, *11*, 148.

[86] A. Srivastava, M. Sidler, A. V. Allain, D. S. Lembke, A. Kis, A. Imamoḃlu, *Nat. Phys.* **2015**, *11*, 141.

[87] G. Plechinger, P. Nagler, A. Arora, A. Granados del Águila, M. V. Ballottin, T. Frank, P. Steinleitner, M. Gmitra, J. Fabian, P. C. M. Christianen, R. Bratschitsch, C. Schüller, T. Korn, *Nano Lett.* **2016**, *16*, 7899.

[88] T. Smoleński, M. Goryca, M. Koperski, C. Faugeras, T. Kazimierczuk, A. Bogucki, K. Nogajewski, P. Kossacki, M. Potemski, *Phys. Rev. X* **2016**, *6*, 021024.

[89] Y. Li, J. Ludwig, T. Low, A. Chernikov, X. Cui, G. Arefe, Y. D. Kim, A. M. van der Zande, A. Rigosi, H. M. Hill, S. H. Kim, J. Hone, Z. Li, D. Smirnov, T. F. Heinz, *Phys. Rev. Lett.* **2014**, *113*, 266804.

[90] A. Arora, R. Schmidt, R. Schneider, M. R. Molas, I. Breslavetz, M. Potemski, R. Bratschitsch, *Nano Lett.* **2016**, *16*, 3624.

[91] A. A. Mitioglu, K. Galkowski, A. Surrente, L. Klopotowski, D. Dumcenco, A. Kis, D. K. Maude, P. Plochocka, *Phys. Rev. B* **2016**, *93*, 165412.

[92] S. Dal Conte, F. Bottegoni, E. A. A. Pogna, D. De Fazio, S. Ambrogio, I. Bargigia, C. D'Andrea, A. Lombardo, M. Bruna, F. Ciccacci, A. C. Ferrari, G. Cerullo, M. Finazzi, *Phys. Rev. B* **2015**, *92*, 235425.

[93] C. R. Zhu, K. Zhang, M. Glazov, B. Urbaszek, T. Amand, Z. W. Ji, B. L. Liu, X. Marie, *Phys. Rev. B* **2014**, *90*, 161302.

[94] L. Yang, N. A. Sinitsyn, W. Chen, J. Yuan, J. Zhang, J. Lou, S. A. Crooker, *Nat.*

Phys. **2015**, *11*, 830.

[95] J. Huang, T. B. Hoang, T. Ming, J. Kong, M. H. Mikkelsen, *Phys. Rev. B* **2017**, *95*, 075428.

[96] G. Plechinger, P. Nagler, A. Arora, R. Schmidt, A. Chernikov, A. G. del Águila, P. C. M. Christianen, R. Bratschitsch, C. Schüller, T. Korn, *Nat. Commun.* **2016**, *7*, 12715.

[97] T. Yan, X. Qiao, P. Tan, X. Zhang, *Sci. Rep.* **2015**, *5*, 15625.

[98] Y. Miyauchi, S. Konabe, F. Wang, W. Zhang, A. Hwang, Y. Hasegawa, L. Zhou, S. Mouri, M. Toh, G. Eda, K. Matsuda, *Nat. Commun.* **2018**, *9*, 2598.

[99] C. Mai, A. Barrette, Y. Yu, Y. G. Semenov, K. W. Kim, L. Cao, K. Gundogdu, *Nano Lett.* **2014**, *14*, 202.

[100] C. Mai, Y. G. Semenov, A. Barrette, Y. Yu, Z. Jin, L. Cao, K. W. Kim, K. Gundogdu, *Phys. Rev. B* **2014**, *90*, 041414.

[101] Q. Wang, S. Ge, X. Li, J. Qiu, Y. Ji, J. Feng, D. Sun, *ACS Nano* **2013**, *7*, 11087.

[102] Y. Zhang, K. Shinokita, K. Watanabe, T. Taniguchi, Y. Miyauchi, K. Matsuda, *Adv. Funct. Mater.* **2021**, *31*, 2006064.

[103] G. Wang, E. Palleau, T. Amand, S. Tongay, X. Marie, B. Urbaszek, *Appl. Phys. Lett.* **2015**, *106*, 112101.

[104] D. MacNeill, C. Heikes, K. F. Mak, Z. Anderson, A. Kormányos, V. Zólyomi, J. Park, D. C. Ralph, *Phys. Rev. Lett.* **2015**, *114*, 037401.

[105] J. S. Ross, S. Wu, H. Yu, N. J. Ghimire, A. M. Jones, G. Aivazian, J. Yan, D. G. Mandrus, D. Xiao, W. Yao, X. Xu, *Nat. Commun.* **2013**, *4*, 1474.

[106] D. Lagarde, L. Bouet, X. Marie, C. R. Zhu, B. L. Liu, T. Amand, P. H. Tan, B. Urbaszek, *Phys. Rev. Lett.* **2014**, *112*, 047401.

[107] D. Schmidt, T. Godde, J. Schmutzler, M. Aßmann, J. Debus, F. Withers, E. M. Alexeev, O. Del Pozo-Zamudio, O. V. Skrypka, K. S. Novoselov, M. Bayer, A. I. Tartakovskii, *Phys. Rev. B* **2016**, *94*, 165301.

[108] C. Robert, D. Lagarde, F. Cadiz, G. Wang, B. Lassagne, T. Amand, A. Balocchi, P. Renucci, S. Tongay, B. Urbaszek, X. Marie, *Phys. Rev. B* **2016**, *93*, 205423.

[109] M. Palummo, M. Bernardi, J. C. Grossman, *Nano Lett.* **2015**, *15*, 2794.

[110] G. Kioseoglou, A. T. Hanbicki, M. Currie, A. L. Friedman, D. Gunlycke, B. T. Jonker, *Appl. Phys. Lett.* **2012**, *101*, 221907.

[111] K. Shinokita, X. Wang, Y. Miyauchi, K. Watanabe, T. Taniguchi, S. Konabe, K. Matsuda, *Phys. Rev. B* **2019**, *100*, 161304.

[112] C. M. Chow, H. Yu, A. M. Jones, J. R. Schaibley, M. Koehler, D. G. Mandrus,

R. Merlin, W. Yao, X. Xu, *npj 2D Mater. Appl.* **2017**, *1*, 33.

[113] G. Kioseoglou, A. T. Hanbicki, M. Currie, A. L. Friedman, B. T. Jonker, *Sci. Rep.* **2016**, *6*, 25041.

[114] K. F. Mak, K. He, C. Lee, G. H. Lee, J. Hone, T. F. Heinz, J. Shan, *Nat. Mater.* **2013**, *12*, 207.

[115] G. Plechinger, P. Nagler, A. Arora, R. Schmidt, A. Chernikov, A. G. del Águila, P. C. M. Christianen, R. Bratschitsch, C. Schüller, T. Korn, *Nat. Commun.* **2016**, *7*, 12715.

[116] M. Selig, G. Berghäuser, A. Raja, P. Nagler, C. Schüller, T. F. Heinz, T. Korn, A. Chernikov, E. Malic, A. Knorr, *Nat. Commun.* **2016**, *7*, 13279.

[117] J. Pei, J. Yang, T. Yildirim, H. Zhang, Y. Lu, *Adv. Mater.* **2018**, *31*, 1706945.

[118] Q. Zhang, S. A. Yang, W. Mi, Y. Cheng, U. Schwingenschlögl, *Adv. Mater.* **2016**, *28*, 959.

[119] Y. Moritomo, A. Asamitsu, H. Kuwahara, Y. Tokura, *Nature* **1996**, *380*, 141.

[120] T. Ishikawa, T. Kimura, T. Katsufuji, Y. Tokura, *Phys. Rev. B* **1998**, *57*, 8079.

[121] M. Baldini, T. Muramatsu, M. Sherafati, H. K. Mao, L. Malavasi, P. Postorino, S. Satpathy, V. V. Struzhkin, *Proc. Natl. Acad. Sci. U. S. A.* **2015**, *112*, 10869.

[122] G. T. Woods, P. Poddar, H. Srikanth, Y. M. Mukovskii, *J. Appl. Phys.* **2005**, *97*, 1.

[123] Y. Moritomo, Y. Maruyama, T. Akimoto, A. Nakamura, *Phys. Rev. B* **1997**, *56*, R7057.

[124] K. Hirota, S. Ishihara, H. Fujioka, M. Kubota, H. Yoshizawa, Y. Moritomo, Y. Endoh, S. Maekawa, *Phys. Rev. B* **2002**, *65*, 064414.

[125] J. F. Mitchell, D. N. Argyriou, J. D. Jorgensen, D. G. Hinks, C. D. Potter, S. D. Bader, *Phys. Rev. B* **1997**, *55*, 63.

[126] D. S. Dessau, T. Saitoh, C. H. Park, Z. H. Shen, P. Villella, N. Hamada, Y. Moritomo, Y. Tokura, *Phys. Rev. Lett.* **1998**, *81*, 192.

[127] Stephen Blundell, *Magnetism in Condensed Matter*, **2001**.

[128] Y. Zhang, K. Shinokita, K. Watanabe, T. Taniguchi, M. Goto, D. Kan, Y. Shimakawa, Y. Moritomo, T. Nishihara, Y. Miyauchi, K. Matsuda, *Adv. Mater.* **2020**, *32*, 2003501.

[129] J. Kutrowska-Girzycka, P. Kapuściński, L. Bryja, A. Wójs, J. Jadczak, Y. S. Huang, *Nanotechnology* **2017**, *28*, 395702.

[130] J. Ye, T. Yan, B. Niu, Y. Li, X. Zhang, *Sci. Rep.* **2018**, *8*, 2389.

[131] N. Lundt, E. Cherotchenko, O. Iff, X. Fan, Y. Shen, P. Bigenwald, A. V. Kavokin,

S. Höfling, C. Schneider, *Appl. Phys. Lett.* **2018**, *112*, 031107.

[132] K. P. O'Donnell, X. Chen, *Appl. Phys. Lett.* **1991**, *58*, 2924.

[133] S. Tongay, J. Zhou, C. Ataca, K. Lo, T. S. Matthews, J. Li, J. C. Grossman, J. Wu, *Nano Lett.* **2012**, *12*, 5576.

[134] H. Wang, C. Zhang, W. Chan, C. Manolatou, S. Tiwari, F. Rana, *Phys. Rev. B* **2016**, *93*, 045407.

[135] M. Palummo, M. Bernardi, J. C. Grossman, *Nano Lett.* **2015**, *15*, 2794.

[136] M. Drüppel, T. Deilmann, P. Krüger, M. Rohlfing, *Nat. Commun.* **2017**, *8*, 2117.

[137] W. Xu, D. Kozawa, Y. Zhou, Y. Wang, Y. Sheng, T. Jiang, M. S. Strano, J. H. Warner, *Small* **2020**, *16*, 1905985.

[138] L. Zhang, H. Yan, X. Sun, M. Dong, T. Yildirim, B. Wang, B. Wen, G. P. Neupane, A. Sharma, Y. Zhu, J. Zhang, K. Liang, B. Liu, H. T. Nguyen, D. Macdonald, Y. Lu, *Nanoscale* **2019**, *11*, 418.

[139] F. Gao, Y. Gong, M. Titze, R. Almeida, P. M. Ajayan, H. Li, *Phys. Rev. B* **2016**, *94*, 245413.

[140] S. Mouri, Y. Miyauchi, K. Matsuda, *Nano Lett.* **2013**, *13*, 5944.

[141] D. Kozawa, R. Kumar, A. Carvalho, K. Kumar Amara, W. Zhao, S. Wang, M. Toh, R. M. Ribeiro, A. H. Castro Neto, K. Matsuda, G. Eda, *Nat. Commun.* **2014**, *5*, 4543.

[142] Y. P. Varshni, *Physica* **1967**, *34*, 149.

[143] G. D. Shepard, J. V. Ardelean, O. A. Ajayi, D. Rhodes, X. Zhu, J. C. Hone, S. Strauf, *ACS Nano* **2017**, *11*, 11550.

[144] H. Zhou, Y. Zhao, W. Tao, Y. Li, Q. Zhou, H. Zhu, *ACS Nano* **2020**, *14*, 4618.

[145] J. Tersoff, *Phys. Rev. Lett.* **1984**, *52*, 465.

[146] A. Kerelsky, A. Nipane, D. Edelberg, D. Wang, X. Zhou, A. Motmaendadgar, H. Gao, S. Xie, K. Kang, J. Park, J. Teherani, A. Pasupathy, *Nano Lett.* **2017**, *17*, 5962.

[147] T. Musso, P. V. Kumar, J. C. Grossman, A. S. Foster, *Adv. Electron. Mater.* **2017**, *3*, 1600318.

[148] B. Scharf, G. Xu, A. Matos-Abiague, I. Žutić, *Phys. Rev. Lett.* **2017**, *119*, 127403.

[149] A. Nagashima, N. Tejima, Y. Gamou, T. Kawai, C. Oshima, *Phys. Rev. B* **1995**, *51*, 4606.

[150] G. Wang, L. Bouet, M. M. Glazov, T. Amand, E. L. Ivchenko, E. Palleau, X. Marie, B. Urbaszek, *2D Mater.* **2015**, *2*, 034002.

[151] C. Zou, C. Cong, J. Shang, C. Zhao, M. Eginligil, L. Wu, Y. Chen, H. Zhang, S. Feng, J. Zhang, H. Zeng, W. Huang, T. Yu, *Nano Res.* **2018**, *11*, 6252.

[152] K. Zollner, M. Gmitra, T. Frank, J. Fabian, *Phys. Rev. B* **2016**, *94*, 155441.

[153] K. Zollner, P. E. Faria Junior, J. Fabian, *Phys. Rev. B* **2020**, *101*, 085112.

[154] P. Rivera, K. L. Seyler, H. Yu, J. R. Schaibley, J. Yan, D. G. Mandrus, W. Yao, X. Xu, *Science* **2016**, *351*, 688.

[155] Y. Cao, V. Fatemi, A. Demir, S. Fang, S. L. Tomarken, J. Y. Luo, J. D. Sanchez-Yamagishi, K. Watanabe, T. Taniguchi, E. Kaxiras, R. C. Ashoori, P. Jarillo-Herrero, *Nature* **2018**, *556*, 80.

[156] Y. Cao, V. Fatemi, S. Fang, K. Watanabe, T. Taniguchi, E. Kaxiras, P. Jarillo-Herrero, *Nature* **2018**, *556*, 43.

[157] K. Tran, G. Moody, F. Wu, X. Lu, J. Choi, K. Kim, A. Rai, D. A. Sanchez, J. Quan, A. Singh, J. Embley, A. Zepeda, M. Campbell, T. Autry, T. Taniguchi, K. Watanabe, N. Lu, S. K. Banerjee, K. L. Silverman, S. Kim, E. Tutuc, L. Yang, A. H. MacDonald, X. Li, *Nature* **2019**, *567*, 71.

[158] E. M. Alexeev, D. A. Ruiz-Tijerina, M. Danovich, M. J. Hamer, D. J. Terry, P. K. Nayak, S. Ahn, S. Pak, J. Lee, J. I. Sohn, M. R. Molas, M. Koperski, K. Watanabe, T. Taniguchi, K. S. Novoselov, R. V. Gorbachev, H. S. Shin, V. I. Fal'ko, A. I. Tartakovskii, *Nature* **2019**, *567*, 81.

[159] M. Förg, A. S. Baimuratov, S. Y. Kruchinin, I. A. Vovk, J. Scherzer, J. Förste, V. Funk, K. Watanabe, T. Taniguchi, A. Högele, *Nat. Commun.* **2021**, *12*, 1656.

[160] A. R. Wildes, V. Simonet, E. Ressouche, G. J. McIntyre, M. Avdeev, E. Suard, S. A. J. Kimber, D. Lançon, G. Pepe, B. Moubaraki, T. J. Hicks, *Phys. Rev. B* **2015**, *92*, 224408.

[161] Z. Ni, A. V. Haglund, H. Wang, B. Xu, C. Bernhard, D. G. Mandrus, X. Qian, E. J. Mele, C. L. Kane, L. Wu, *Nat. Nanotechnol.* **2021**, *16*, 782.

[162] S. L. Gnatchenko, I. S. Kachur, V. G. Piryatinskaya, Y. M. Vysochanskii, M. I. Gurzan, *Low Temp. Phys.* **2011**, *37*, 144.

[163] M. Onga, M. Onga, Y. Sugita, T. Ideue, T. Ideue, Y. Nakagawa, Y. Nakagawa, R. Suzuki, R. Suzuki, Y. Motome, Y. Iwasa, *Nano Lett.* **2020**, *20*, 4625.

[164] X. Wang, J. Cao, Z. Lu, A. Cohen, H. Kitadai, T. Li, Q. Tan, M. Wilson, C. H. Lui, D. Smirnov, S. Sharifzadeh, X. Ling, *Nat. Mater.* **2021**, *20*, 964.

[165]K. Hwangbo, Q. Zhang, Q. Jiang, Y. Wang, J. Fonseca, C. Wang, G. M. Diederich, D. R. Gamelin, D. Xiao, J.-H. Chu, W. Yao, X. Xu, *Nat. Nanotechnol.* **2021**, *16*, 655.

[166] S. Kang, K. Kim, B. H. Kim, J. Kim, K. I. Sim, J. U. Lee, S. Lee, K. Park, S. Yun, T. Kim, A. Nag, A. Walters, M. Garcia-Fernandez, J. Li, L. Chapon, K. J. Zhou,

Y. W. Son, J. H. Kim, H. Cheong, J. G. Park, *Nature* **2020**, *583*, 785.

[167] Y. J. Sun, Q. H. Tan, X. L. Liu, Y. F. Gao, J. Zhang, *J. Phys. Chem. Lett.* **2019**, *10*, 3087.

[168] Y. Guo, C. Liu, Q. Yin, C. Wei, S. Lin, T. B. Hoffman, Y. Zhao, J. H. Edgar, Q. Chen, S. P. Lau, J. Dai, H. Yao, H.-S. P. Wong, Y. Chai, *ACS Nano* **2016**, *10*, 8980.

[169] Y. Zhang, K. Shinokita, K. Watanabe, T. Taniguchi, Y. Miyauchi, K. Matsuda, *Adv. Funct. Mater.* **2020**, 2006064.

[170] J. S. Ross, S. Wu, H. Yu, N. J. Ghimire, A. M. Jones, G. Aivazian, J. Yan, D. G. Mandrus, D. Xiao, W. Yao, X. Xu, *Nat. Commun.* **2013**, *4*, 1474.

[171] A. R. Wildes, B. Roessli, B. Lebech, K. W. Godfrey, *J. Phys. Condens. Matter* **1998**, *10*, 6417.

[172] S. Mouri, W. Zhang, D. Kozawa, Y. Miyauchi, G. Eda, K. Matsuda, *Nanoscale* **2017**, *9*, 6674.

[173] J. Joshi, T. Zhou, S. Krylyuk, A. V. Davydov, I. Žutić, P. M. Vora, *ACS Nano* **2020**, *14*, 8528.

[174] H. Yu, G.-B. Liu, J. Tang, X. Xu, W. Yao, *Sci. Adv.* **2017**, *3*, e1701696.

[175] E. Marcellina, X. Liu, Z. Hu, A. Fieramosca, Y. Huang, W. Du, S. Liu, J. Zhao, K. Watanabe, T. Taniguchi, Q. Xiong, *Nano Lett.* **2021**, *21*, 4461.

[176] Z. Li, X. Lu, D. F. Cordovilla Leon, Z. Lyu, H. Xie, J. Hou, Y. Lu, X. Guo, A. Kaczmarek, T. Taniguchi, K. Watanabe, L. Zhao, L. Yang, P. B. Deotare, *ACS Nano* **2021**, *15*, 1539.

[177] K. Shinokita, Y. Miyauchi, K. Watanabe, T. Taniguchi, K. Matsuda, *Nano Lett.* **2021**, *21*, 5938.

[178] Y. Li, A. Chernikov, X. Zhang, A. Rigosi, H. M. Hill, A. M. van der Zande, D. A. Chenet, E.-M. Shih, J. Hone, T. F. Heinz, *Phys. Rev. B* **2014**, *90*, 205422.

[179] Y. Bai, L. Zhou, J. Wang, W. Wu, L. J. McGilly, D. Halbertal, C. F. B. Lo, F. Liu, J. Ardelean, P. Rivera, N. R. Finney, X. C. Yang, D. N. Basov, W. Yao, X. Xu, J. Hone, A. N. Pasupathy, X. Y. Zhu, *Nat. Mater.* **2020**, *19*, 1068.

[180] P. Hohenberg, W. Kohn, *Phys. Rev.* **1964**, *136*, B864.

[181] W. Kohn, L. J. Sham, *Phys. Rev.* **1965**, *140*, A1133.

[182] Y. Morikawa, K. Iwata, K. Terakura, *Appl. Surf. Sci.* **2001**, *169–170*, 11.

[183] https://state-doc.readthedocs.io/en/latest/index.html**.**

[184] J. P. Perdew, K. Burke, M. Ernzerhof, *Phys. Rev. Lett.* **1996**, *77*, 3865.

[185] K. Lee, É. D. Murray, L. Kong, B. I. Lundqvist, D. C. Langreth, *Phys. Rev. B*

2010, *82*, 081101.

[186] V. R. Cooper, *Phys. Rev. B* **2010**, *81*, 161104.

[187] W. Kohn, L. J. Sham, *Phys. Rev.* **1965**, *140*, A1133.

[188] G. Moody, K. Tran, X. Lu, T. Autry, J. M. Fraser, R. P. Mirin, L. Yang, X. Li, K. L. Silverman, *Phys. Rev. Lett.* **2018**, *121*, 57403.

[189] M. Brotons-Gisbert, H. Baek, A. Molina-Sánchez, A. Campbell, E. Scerri, D. White, K. Watanabe, T. Taniguchi, C. Bonato, B. D. Gerardot, *Nat. Mater.* **2020**, *19*, 630.

[190] W. Li, X. Lu, S. Dubey, L. Devenica, A. Srivastava, *Nat. Mater.* **2020**, *19*, 624.

[191] C. Kammerer, G. Cassabois, C. Voisin, M. Perrin, C. Delalande, P. Roussignol, J. M. Gérard, *Appl. Phys. Lett.* **2002**, *81*, 2737.

[192] I. Sarpkaya, Z. Zhang, W. Walden-Newman, X. Wang, J. Hone, C. W. Wong, S. Strauf, *Nat. Commun.* **2013**, *4*, 2152.

[193]T. Kuroda, Y. Sakuma, K. Sakoda, K. Takemoto, T. Usuki, *Appl. Phys. Lett.* **2007**, *91*, 223113.

Scientific contributions

List of publications

1. **Controllable Magnetic Proximity Effect and Charge Transfer in 2D Semiconductor and Double-Layered Perovskite Manganese Oxide van der Waals Heterostructure**
   Y. Zhang, K. Shinokita, K. Watanabe, T. Taniguchi, M. Goto, D. Kan, Y. Shimakawa, Y. Moritomo, T. Nishihara, Y. Miyauchi, K. Matsuda.
   Adv. Mater. 2020, *32*, 2003501. **Back inside cover**.

2. **Magnetic Field Induced Inter-Valley Trion Dynamics in Monolayer 2D Semiconductor**
   Y. Zhang, K. Shinokita, K. Watanabe, T. Taniguchi, Y. Miyauchi, K. Matsuda.
   Adv. Funct. Mater. 2021, *31*, 2006064.

3. **Magnon Coupled Intralayer Moiré Trion in Monolayer Semiconductor and Antiferromagnet Heterostructure**
   Y. Zhang, L. Kim, K. W. Zhang, K. Watanabe, T. Taniguchi, Y. Gao, M. Maruyama, S. Okada, K, Shinokita, and K. Matsuda.
   Adv. Mater. 2022, 2200301.

4. **Ultralarge Photoluminescence Enhancement of Monolayer Molybdenum Disulfide by Spontaneous Superacid Nanolayer Formation**
   Y. Yamada, **Y. Zhang**, H. Ikeno, K. Shinokita, T. Yoshimura, A. Ashida, N. Fujimura, K. Matsuda, and D. Kiriya.
   ACS Appl. Mater. Interfaces 2021,13, 25280.

Conference presentations

International conferences

1. **Optical Spectroscopy of Artificial Hetero-structure of Monolayer $MoSe_2$ and Manganese Oxide**
   Y. Zhang.
   3rd Seminar of A3 Japan-China-Korea Foresight Program on June 30-July 2, 2019, in Korea, Poster.
2. **Spectroscopic Studies of Monolayer $MoSe_2$ on Strongly Correlated Manganese Oxide**
   Y. Zhang, K. Shinokita, Y. Miyauchi, Y. Moritomo, and K. Matsuda.
   Recent Progress in Graphene and 2D Material Research on October 6-10, 2019, Oral presentation.

Domestic conferences

1. **Optical Spectroscopy of Artificial Heterostructure of Monolayer $MoSe_2$ and Manganese Oxide**
   Y. Zhang, K. Shinokita, Y. Miyauchi, Y. Moritomo, and K. Matsuda.
   The Japan Society of Applied Physics on March 9-12, 2019, Poster.
2. **Optical Studies of Monolayer $MoSe_2$ on Strongly Correlated Manganese Oxide**
   Y. Zhang, Y. Moritomo, K. Shinokita, Y. Miyauchi, and K. Matsuda.
   Fullerenes, Nanotube and Graphene Research Society Symposium on September 3-6, 2019, Poster.
3. **Optical Properties in Van der Waals Heterostructure of Monolayer $MoSe_2$ and Perovskite Manganese Oxide**
   Y. Zhang, K. Shinokita, K. Watanabe, T. Taniguchi, Y. Moritomo, Y. Miyauchi, and K. Matsuda.
   JSAP-OSA Joint Symposia on September 8-11, 2020, Oral presentation.
4. **Intra-layer Excitons Trapped in Moiré Potential on Monolayer-$MoSe_2$/$NiPS_3$ Heterostructure**
   Y. Zhang, K. Shinokita, Y. Miyauchi, Y. Moritomo, and K. Matsuda.
   Fullerenes, Nanotube and Graphene Research Society Symposium on March 8-9, 2021, Poster.